A Scalable DC Microgrid Architecture for Rural Electrification in Emerging Regions

Achintya Madduri

Electrical Engineering and Computer Sciences
University of California at Berkeley

Technical Report No. UCB/EECS-2015-240
http://www.eecs.berkeley.edu/Pubs/TechRpts/2015/EECS-2015-240.html

December 16, 2015

A Scalable DC Microgrid Architecture for Rural Electrification in Emerging Regions

by

Parimalram Achintya Madduri

A dissertation submitted in partial satisfaction of the
requirements for the degree of
Doctor of Philosophy

in

Engineering–Electrical Engineering and Computer Science

in the

Graduate Division
of the
University of California, Berkeley

Committee in charge:
Professor Seth R. Sanders, Chair
Professor Eric Brewer, Co-Chair
Professor Duncan Callaway

Fall 2015

A Scalable DC Microgrid Architecture for Rural Electrification in Emerging Regions

Abstract

A Scalable DC Microgrid Architecture for Rural Electrification in Emerging Regions

by

Parimalram Achintya Madduri
Doctor of Philosophy in Engineering–Electrical Engineering and Computer Science

University of California, Berkeley

Professor Seth R. Sanders, Chair
Professor Eric Brewer, Co-Chair

This dissertation discusses the design and validation of a community-scale DC microgrid architecture that can integrate renewable generation sources by using a distributed control scheme implemented on the microgrid-connected households to mitigate resource variability. The presented system is designed to address the technical and economic challenges of electrifying emerging regions. The levelized cost of electricity (LCOE) is expected to be less than $0.40 per kW-hr over a 15 year horizon.

Solar panel costs have steadily declined to make them a very affordable option for distributed generation. However, battery costs have not declined at the same rate. The important figure of merit for microgrids is the efficiency of stored electricity. The architecture presented in this work is shown to minimize losses in stored electricity. Another key feature of the system is the ability to prioritize loads by controlling the power flow of the system.

There are three key components of the presented DC microgrid architecture: source converters, fanout nodes, and household power management units (PMUs). The functionality of each of these components and the rationale for their design choices is presented in detail. The PMUs implement a distributed loadline control scheme to mitigate variability in available grid power. The design of the distributed control scheme of the DC microgrid is discussed in detail. The relevance of Lyapunov based analysis towards the large signal stability of grid voltage is also discussed.

The first-generation system uses a phase shifted full-bridge converter topology in the PMUs to convert from 380-to-12V in a single stage. Analytical analysis of this topology shows large signal and small signal stability. Transient response of the grid voltages and currents is shown through simulations. Experimental results are presented that showcase the operation and efficiency of system hardware.

The second-generation system incorporates a two-stage conversion architecture. The first stage is a 380-to-48V fixed ratio bus converter, which is used to generate a 48V bus for a local cluster of connected households. In the second stage, PMUs utilize a buck converter topology to step down from 48V-to-12V in each household. In addition to

simulation and experimental validation of the hardware, a cost analysis is also presented to determine LCOE of system. The second-generation architecture achieves higher efficiency and reduced cost in comparison to the first-generation.

Lastly, grounding and protection of the microgrid is discussed in detail. Relevant examples from existing distribution schemes are presented and the rationale behind existing schemes are explored. A grounding and protection scheme that is suited to this dissertation's DC microgrid is presented. The protection scheme is validated throgh relevant simulations and experiments.

This work presents a grid topology that is designed to adapt to a changing landscape of solar PV prices and meets the challenge of providing a scalable and low-cost electrification solution. Future efforts in addressing the energy needs of unelectrified regions can build on the work presented in this dissertation.

Dedicated to my family, whose love and support has been ever constant.

Contents

List of Figures

List of Tables

Acknowledgments

I want to first acknowledge my advisors Professors Seth Sanders and Eric Brewer. Their continued support and guidance was instrumental in the process of completing this dissertation. I also want to thank my fellow group members in both the Power Electronics and TIER Research Groups. My colleagues provided invaluable knowledge and support through our numerous conversations.

Finally, I want to thank my family for their encouragement and support. I would never have reached this point if it were not for them.

Chapter 1

Background and Motivation

1.1 Introduction

There are over 1.3 billion people worldwide lacking access to electricity. This energy poverty has a large adverse effect on economic development and education outcomes. In addition, many of these populations rely on fossil fuels (kerosene and wood) for their primary lighting needs; fossil fuels are an inefficient source of lighting and their use has significant detrimental impacts on the environment and on public health. Unelectrified populations are located predominantly in rural emerging regions that are unconnected to the central electricity grid (Table 1.1). These presently unelectrified households are expected to drive most of the medium-term (next 20-30 years) growth in energy consumption[13]. Grid extension to meet their energy needs is not viable because of high connection costs. In addition, grid operators face structural disincentives to providing grid-connectivity—such as high transmission losses, and electricity theft [14]. Furthermore, studies show that grid extension does not guarantee access to reliable electricity; there is a high degree of load-shedding and service-unreliability for rural customers [15]. However, the steep decline in cost of solar photovoltaic panels provides a viable renewable, distributed alternative to grid-generated electricity. Based on the usage data from recent field studies to establish solar PV-powered microgrids [16], there is a strong body of evidence to suggest that a fully DC solar-PV-powered system with distributed storage at every household will increase the efficiency, and reduce the costs of providing sustainable, and reliable electricity to rural emerging regions.

A scalable DC microgrid with distributed storage is designed and tested in this dissertation (Fig. 1.1); The DC microgrid has been designed to meet the electricity needs of households within a 1 km radius, and has the following features:

1. **DC power generation and distribution:** Line distribution losses will be minimized by using 380V for distribution. Electricity will be converted to safer 12V at the households.

2. **Household Power Management Units (PMUs):** The DC distribution lines

Table 1.1: Overview of population lacking electricity-access

Target Characteristics	
No. of people lacking electricity-access	1.3 billion[13]
Distance from transformer substation	5-50km
Microgrid size	50-100 households
Target levelized cost	less than $0.40 per kW-hr
Initial electricity usage per household	100-500 W-hrs/day[17]

will be connected to each household via a DC-DC converter integrated into the PMU that provides the power for all household appliances. PMUs also integrate scalable distributed storage that is owned by the individual households. In addition, the PMUs can digitally communicate information such as price, charge-state of households, credits, and usage.

3. **Distributed control scheme to mitigate variability in grid power:** A droop-voltage power-sharing scheme is implemented, wherein the microgrid distribution-bus voltage droops in response to low-supply/high-demand. The PMUs in turn respond by reducing the power that they are drawing from the grid by reducing their battery charging load. The control of grid voltage is thereby distributed to the PMUs connected to the grid. This feature is enabled by the combination of DC voltage distribution, and distributed storage. Since the PMUs are able to communicate digitally to the power station, we are also able to do more advanced scheduling and load-management.

4. **High-efficiency DC Appliances:** PMUs have DC-DC converters that provide power to efficient DC appliances (such as LED lighting). Small-scale, point-of-load inverters are used for AC appliances.

5. **Scalable Distributed Storage:** Battery-storage integrated into individual PMUs reduces losses of stored energy by minimizing conversion steps, and line-losses. Distributed storage also allows for household loads to be decoupled from the grid-supply as required. Furthermore, household ownership of batteries allows for flexible, demand-driven growth of storage in the grid; each household makes decisions about the size of their storage-capacity based on desired night-time usage.

1.2 Background

Despite significant growth in global electrification-rates over the past few decades, lack of electricity-access remains significant in many parts of the world. The number of

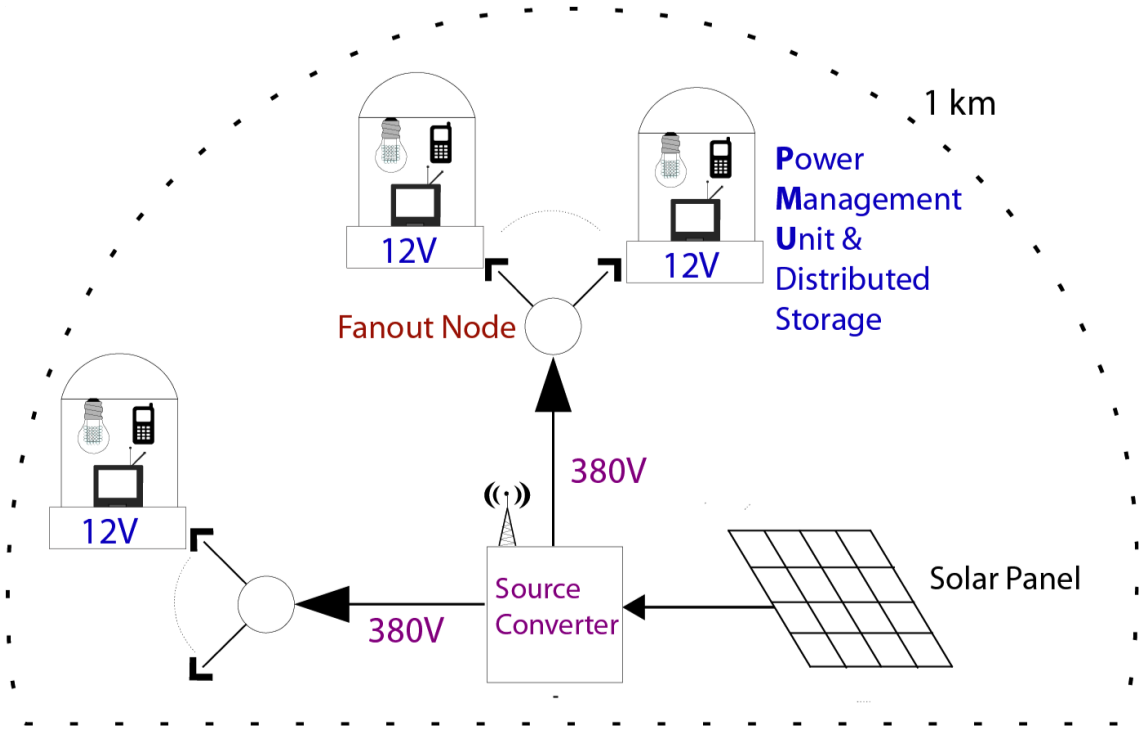

Figure 1.1: Overview of DC microgrid architecture with 380V distribution that is converted to 12V for household usage.

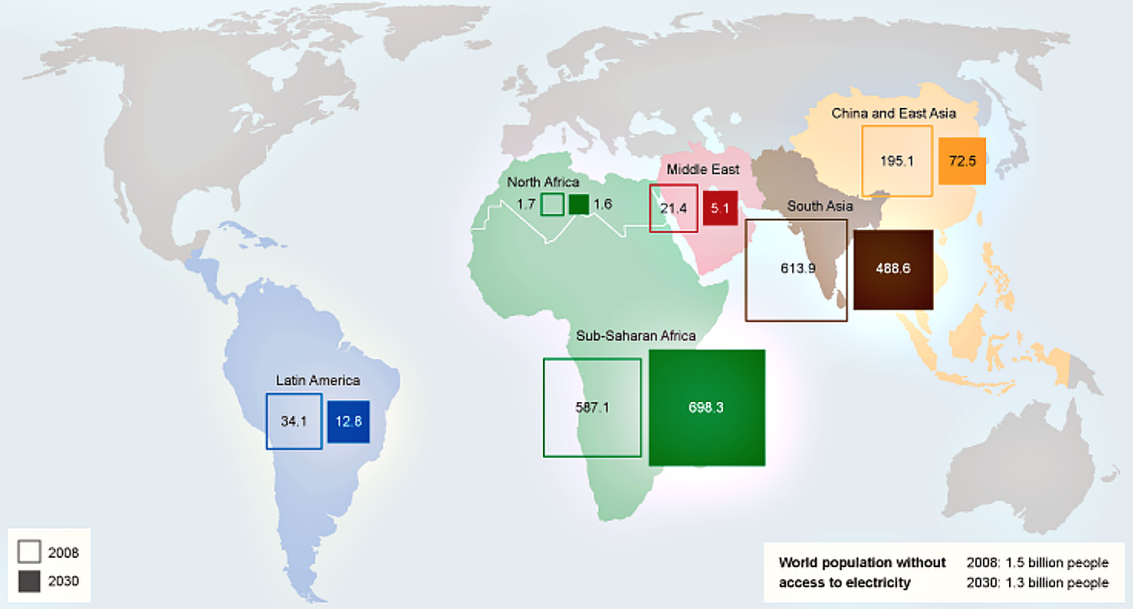

Figure 1.2: International Energy Agency projection of world populations without energy-access in 2030. Populations (in millions) without electricity-access are shown for 2008 and projected for 2030 based on the IEA reference scenario[1].

people lacking electricity-access, as projected by the International Energy Agency (IEA), is expected to be unchanged through 2030 (shown in Figure 1.2). There are regions, such as Sub-Saharan Africa, where the rate of increase in grid-electricity-access will not be able to keep pace with population growth. However, as shown in Figure 1.3, regions with largest unelectrified populations correlate with the highest solar energy potentials. The cost of PV ($/W) has fallen substantially in the last 5 years (shown in Figure 1.4). In addition, the compact and modular nature of solar-panels makes them ideal candidates for electricity-generation in remote, rural regions with limited transportation infrastructure. Based on the above factors, there is a basis for hypothesizing that solar PV can prove to be a cheap and sustainable source of generating electricity in areas with low rates of electricity-access.

1.3 Economic Motivations for Rural Electrification

Energy poverty is predominantly a rural issue. Significant monies from rural poor are used towards inefficient lighting, and mobile-device charging. Figure 1.5 shows that a clear positive relationship between economic development, and electricity-access has been established through numerous studies worldwide. An implication of this relationship is that not only will reliable electricity-access be a net economic benefit, electricity-demand of newly electrified populations will also grow over time. The positive relationship between

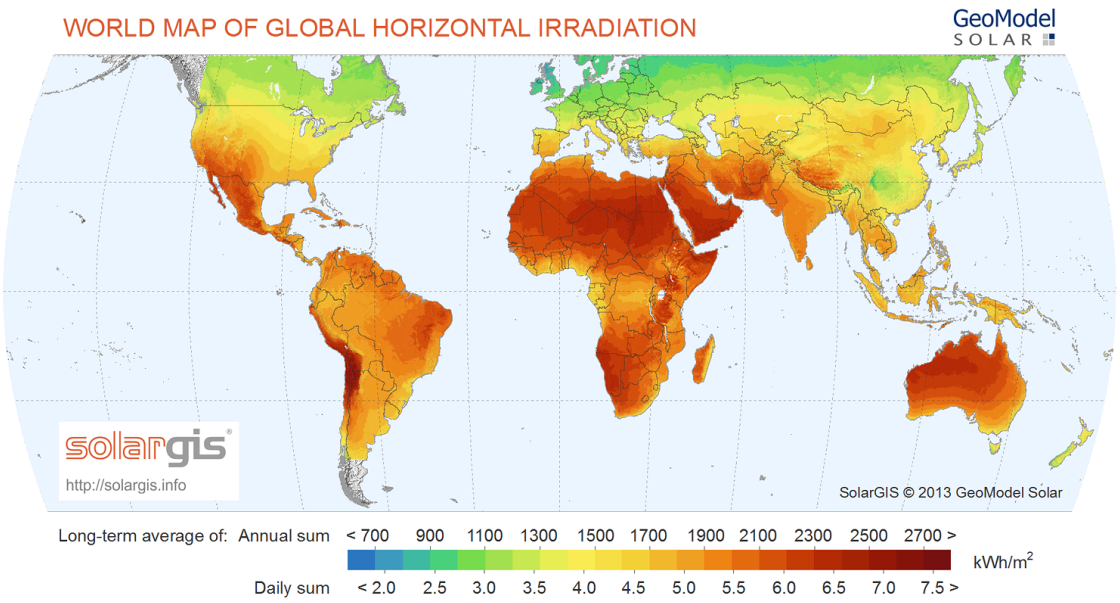

Figure 1.3: Map of global annual solar irradiance. Sub-saharan Africa and the Indian sub-continent, areas with lowest global electrification-rates, have the highest annual solar irradiance.

economic growth and energy demand has been measured for first 5.5-11kWh per-capita per-day.

The IEA predicts that in order to achieve universal energy access, a majority of the unelectrified rural people will have to rely on decentralized sources for electricity. This is because grid extension is restricted due to the significant connection costs compared to expected usage [2]. Beyond serving basic lighting needs, high value end-uses for electricity for rural populations in emerging regions include: computing, mobile device charging, television, refrigeration, fans/HVAC, and motor applications. There is a significant potential for growth in the electricity-demand as off-grid populations are electrified. A decentralized electrification solution that is easily scalable is necessary to bridge the energy access gap that exists between the electrified and un-electrified populations of emerging regions.

1.4 Existing Energy Access Options for Rural Off-grid Regions

Presently deployed distributed-solutions for electricity-access in rural off-grid regions include solar lanterns, and solar home systems (Fig. 1.6). While they both can provide essential services to off-grid populations, they are limited in their inability to: (a) scale to support higher load levels, and (b) integrate multiple generation sources[18].

Solar lanterns are stand-alone devices that are suitable for providing night-time light-

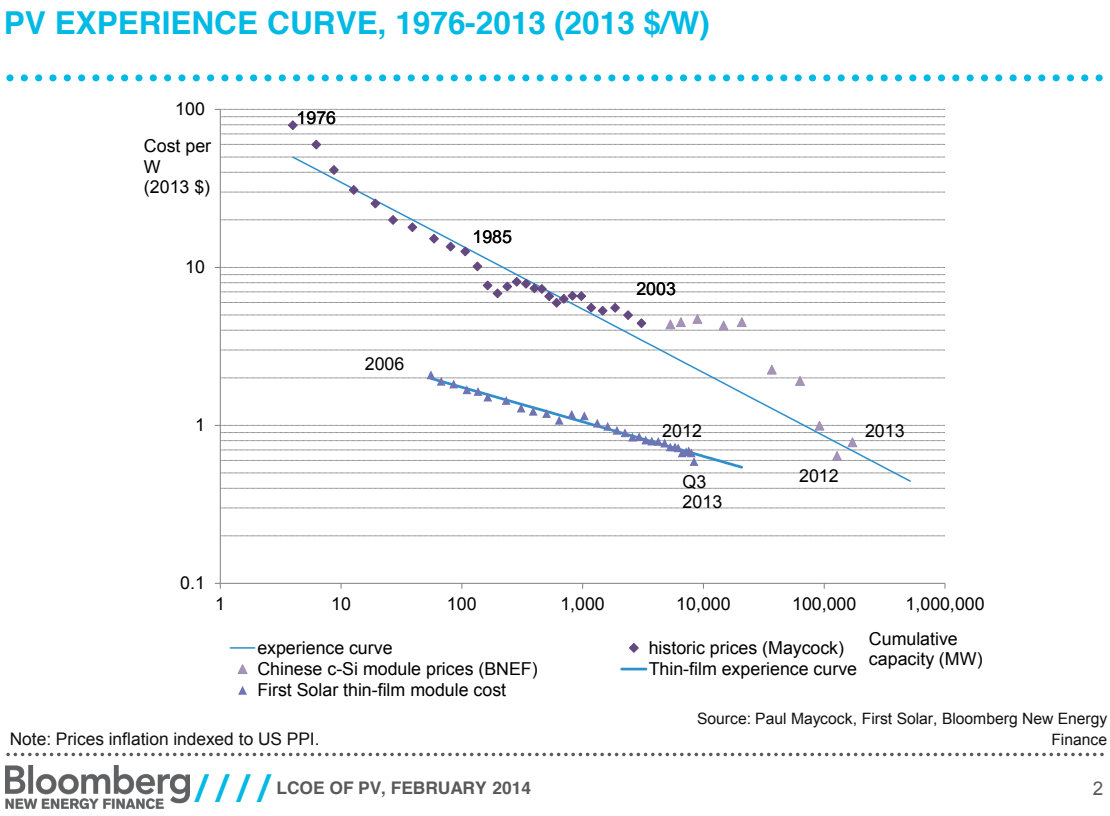

Figure 1.4: Experience curve of solar PV modules. As the amount of total installed solar PV has grown, the prices of PV modules ($/W) has fallen substantially.

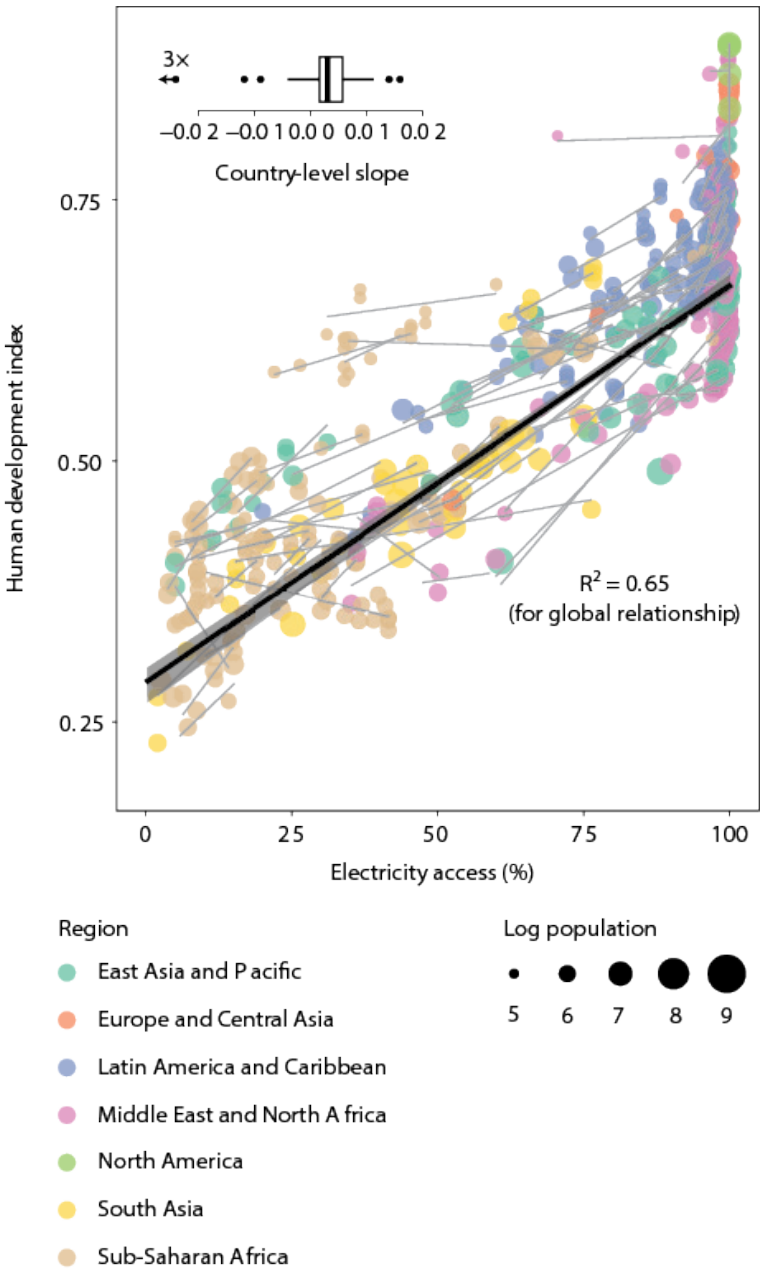

Figure 1.5: Relationship between electricity-access rate (%) and human development index (HDI). The changes in electricity-access rate and HDI are parametrically plotted for individual countries for data collected from 2000-2010. Trend-lines are shown for individual countries (grey) and across all countries (bold black)[2].

ing, and cell-phone charging. However, solar lanterns are very limited in the amount of electricity that they can provide for more energy-intensive end uses.

Solar home systems have been successful in some countries (ex: Bangladesh) in addressing the electricity needs of off-grid households[19]. However, they do not have the ability to multiplex either generation, or electricity-storage over multiple households.

Both solar lanterns, and solar home systems do not present an easy pathway towards integrating other sources of generation. It would not be possible to easily integrate a grid-connection with both these types of systems in the future—if the central grid is able to expand and provide electricity-service to currently off-grid customers. Solar lanterns, and solar home systems also cannot be easily interconnected; the possibility of aggregating multiple customers to achieve a higher bargaining power with utilities is very limited.

Grid-connectivity to the central electric grid exists on the other end of the energy services spectrum. However, there are many barriers towards extension of central-grid-connectivity to presently off-grid regions. A large percentage of unelectrified communities are in areas where the cost of connectivity is very high. Figure 1.7 shows the cost of grid-connectivity is significant in many country with low national rates of electrification-coverage. In addition, studies have shown that grid-connectivity does not guarantee electricity-service for rural customers. Service reliability for grid-connections in rural emerging regions is very poor. Rural customers are often the primary targets when grid operators engage in load-shedding [20]. This is because utilities face higher transmission-losses for providing rural customers electricity-service. Furthermore, the rate of payment for electricity is lower for rural customers in comparison to urban customers, even in the same country. Free and subsidized rural-electricity-schemes are often provided by politicians as incentives to rural voters[21]. Many of the countries with low electrification rates also face significant shortfalls in grid generation capacity. Demand for electricity far outstrips the available utility supply. Regulation barriers often prevent utilities from raising electricity rates to generate the required capital to add more generation to their portfolio. These barriers are also another factor dis-incentivizing utility operators from connecting off-grid rural customers to the central electricity grid.

1.5 Advantages of DC Microgrids with Distributed Storage for Rural Electrification

1.5.1 Microgrids vs other distributed electricity-access solutions

Microgrids are interconnected systems that integrate multiple loads with at least one generation source and hence are able to use the benefit of multiplexing to achieve higher net-utilization of resources. In general microgrids have the following properties:

1. Microgrids are stand-alone, small-scale electricity grids that interconnect multiple households.

Figure 1.6: Solar lanterns (left) and solar home systems (right) are both existing options for distributed energy access in rural emerging regions.

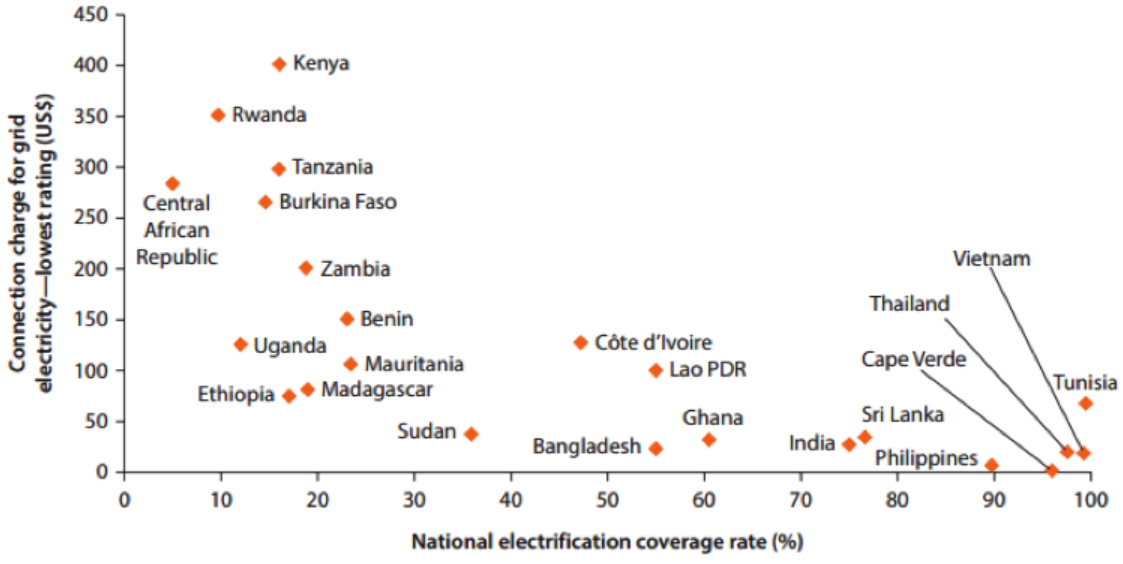

Figure 1.7: Connection cost for grid connectivity and rural electrification rate for a number of African and Asian countries[3].

2. Microgrids can have a single, or multiple sources of generation.

3. Microgrids are not necessarily independent of a larger microgrid; but they have the ability to run independently—in an islanded-operation mode.

4. Most importantly, microgrid installers, and operators have a larger degree of control over grid equipment functionality, and operation. This enables the ability to make design tradeoffs, and to tailor microgrids to serve specific community needs.

One of the challenges in sizing solar home systems is that the system components have to be rated for peak load; therefore, the utilization-ratio—the ratio of average utilization of a system hardware to peak utilization—is often low. In comparison, microgrids are able to multiplex usage over the multiple connected households, and increase the net utilization-ratio of system components. As shown in Figure 1.8, microgrids can support a higher level of service than other distributed electricity-access solutions—i.e. solar lanterns and solar home systems. The system costs per-unit-of-installed-capacity are also lower for microgrids in comparison to other distributed options (Fig. 1.9). Therefore, microgrids have many benefits as a bridge solution to provide electricity-access to off-grid communities. They can provide electricity at low cost over a relatively wide range of per-capita-electricity-usage.

Microgrids also have the ability to integrate multiple generation sources. This diversity of generation is a way to enhance reliability of electricity-service. For example, in the case of individual home systems, it is cost-prohibitive to include a diesel backup generator for situations when the solar resource is limited over an extended period of time. The capital costs can be multiplexed in microgrids. Furthermore, a microgrid can function as an aggregated entity to a utility provider. A rural microgrid as a single customer can be more lucrative to a utility than multiple, individual rural households. The load-aggregation, and other ancillary services provided by microgrids can be motivating factors in convincing utilities to provide a grid-connection to presently off-grid communities. Microgrids easily integrate with the central grid if it is extended to the community in the future. Grid connectivity can be treated as another generation source to a microgrid[22].

1.5.2 AC vs DC microgrids

The efficiency gains associated with using a DC architecture for household settings has been explored in the context of integrating renewable resources and electric vehicles in countries with a strong central grid architecture [22, 23]. However the case for deploying DC microgrids in rural emerging regions is even stronger due to the combination of the following factors:

1. There are many advantages of using solar PV for distributed generation in rural emerging regions such as:

   (a) Availability of solar resource in regions with low electricity-access.

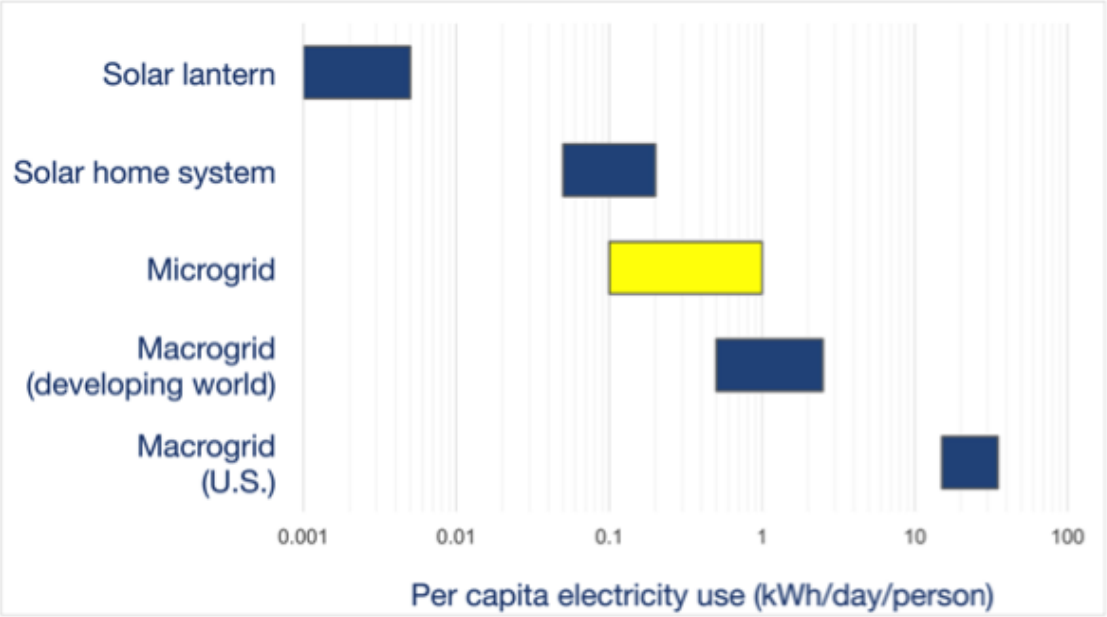

Figure 1.8: Per capita electricity use (kWh/day/person) that can be supported by different energy technologies[4]. Microgrids have a potential to be a bridge solution for energy access as they can support greater per capita electricity use than other distributed options.

(b) The low cost of PV as a generation source.

(c) The modularity and ease of transport of PV panels.

2. The predominant usages of rural off-grid customers—lighting, cell phone charging, fans—come from DC appliances.

Studies suggest that a 20% cost-reduction is possible through gains associated with improved power-conversion efficiencies that can be realized with a fully DC microgrid [24]. Distributed point-of-load (POL) converters can achieve higher efficiencies than always-on central inverters; POL converters can be selectively turned off, and thereby reduce standby electricity-losses in the grid. The potential efficiency improvements of a solar-powered DC microgrid compared to an equivalent AC microgrid are shown in Figure 1.10. Some of the main factors that influence the efficiency calculations shown in Figure 1.10 are:

1. In an AC microgrid with a centralized battery bank, there is a constant source of loss due to the always-on inverter. In a DC microgrid with distributed storage, this loss is mitigated during nighttime as the DC distribution is off at night.

2. A majority of end-use appliances are inherently DC devices. The losses from POL AC-DC adapters have been estimated to be around 15%[8]. This is energy that is lost without any end-use benefit.

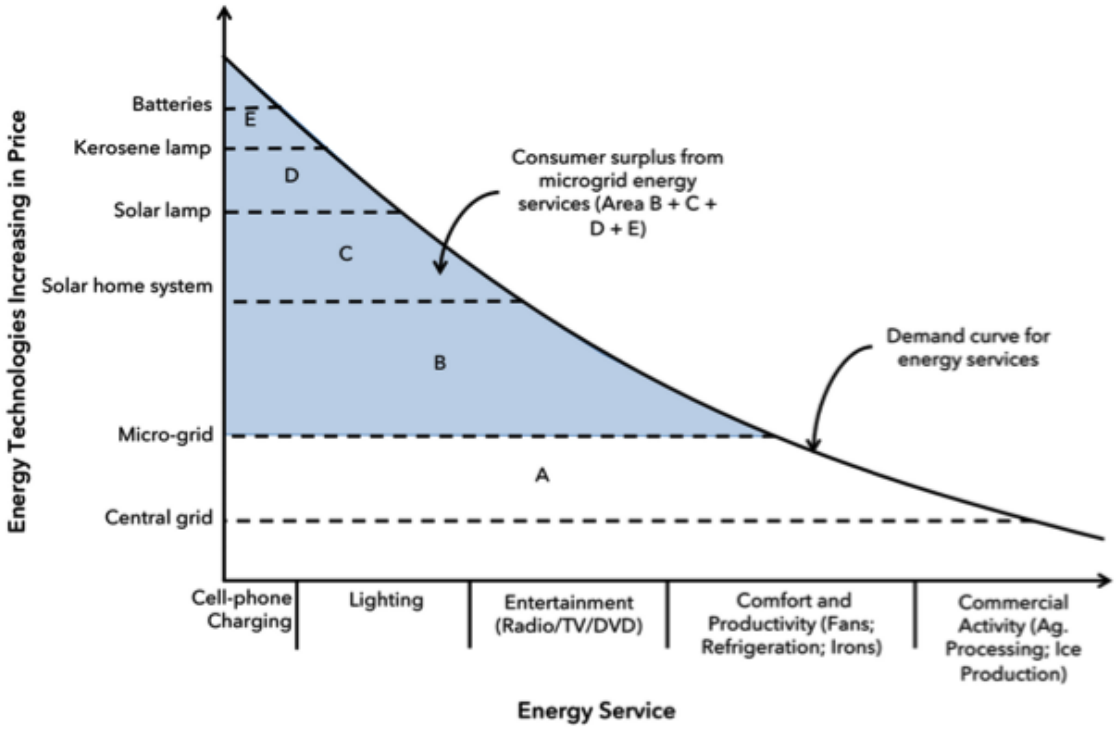

Figure 1.9: Relative cost of energy technologies (cost per unit energy) and the types of energy services that they can provide[5]. Microgrids can provide more energy services than other distributed energy technologies at a lower price per unit energy.

3. In an AC microgrid, inverter losses can dominate with mismatch in rated-power to actual load. The size of the inverter (kVA-rating) is determined by the peak power-load expected. There have been numerous microgrid studies that show that peak loads are correlated in time across many households. Examples of such loads are electric rice cookers and electric kettles running at the same time of the day[25]. Inverters that are sized to match the average power demand are unable to mitigate these correlated peaks in demand and this mismatch leads to grid-wide brownouts. In a DC microgrid with distributed storage, the batteries function as local energy buffers that filter variability in power-demand on upstream power converters.

4. On the other end of the spectrum, when the average power demand is substantially below peak in an AC microgrid, inverter efficiencies suffer. This is due to the fact that inverter efficiencies are highest when operating between 80-90% of rated output capacity. When inverters are operated at low utilization-rates (average-load/rated-capacity), the overall efficiencies of AC microgrids suffer. When storage is distributed, the upstream power converters can be sized to better match average demand and hence operate at higher efficiencies. It is possible to easily distribute storage in DC microgrids.

5. In addition, it is generally hard to resize AC microgrids incrementally. The lack of an inverter and centralized-storage makes it easy to incrementally add more generation in a DC microgrid with distributed storage.

Solar PV prices have fallen significantly over the last 5 years. Prices of solar panels are currently below $1.00 per W as shown in Figure 1.4. But a large part of lifetime costs for off-grid systems is the cost of storage. Most solar panels are rated to have a 20 year operational lifetime. However, most batteries have to be replaced approximately every 2000 cycles or every 5 years. Table 1.2 shows that the cost of storage over a microgrid system life can be 8 times the cost of generation per unit (W) of solar PV installed. This calculation is based on replacing batteries every 5 years. The assumption that 100% of the generated energy needs to be stored for nighttime usage is conservative, but accurate for rural microgrids—where electricity use is predominantly for nighttime lighting, cell-phone charging, and television. It is therefore important to note that a key figure-of-merit (FOM) for off-grid systems is the efficiency of stored power η_{stored}. It is by this FOM that a DC system with distributed storage can far outperform an equivalent AC system. Distributed storage is easily enabled in DC systems but impossible in AC systems without many extraneous conversion steps.

Furthermore, a distributed system allows for greater control over the size of storage at an individual household level. By enabling direct end-user control of both size and usage of stored energy (rather than using a proxy mechanism such as day-night pricing), a DC microgrid can enhance resource management of stored energy. Most customers are well accustomed to tailoring usage when the charge state of their individual batteries is low; widespread cell phone penetration has familiarized most people with the need to

conserve on usage when device batteries are low on charge. Also, matching customer needs with storage-size effectively, and allowing for easy growth-of-storage-capacity are very important value propositions in microgrids.

The remainder of this dissertation discusses in detail the architecture and components of a DC microgrid system that has been designed to electrify rural emerging regions in a scalable, and cost-effective manner.

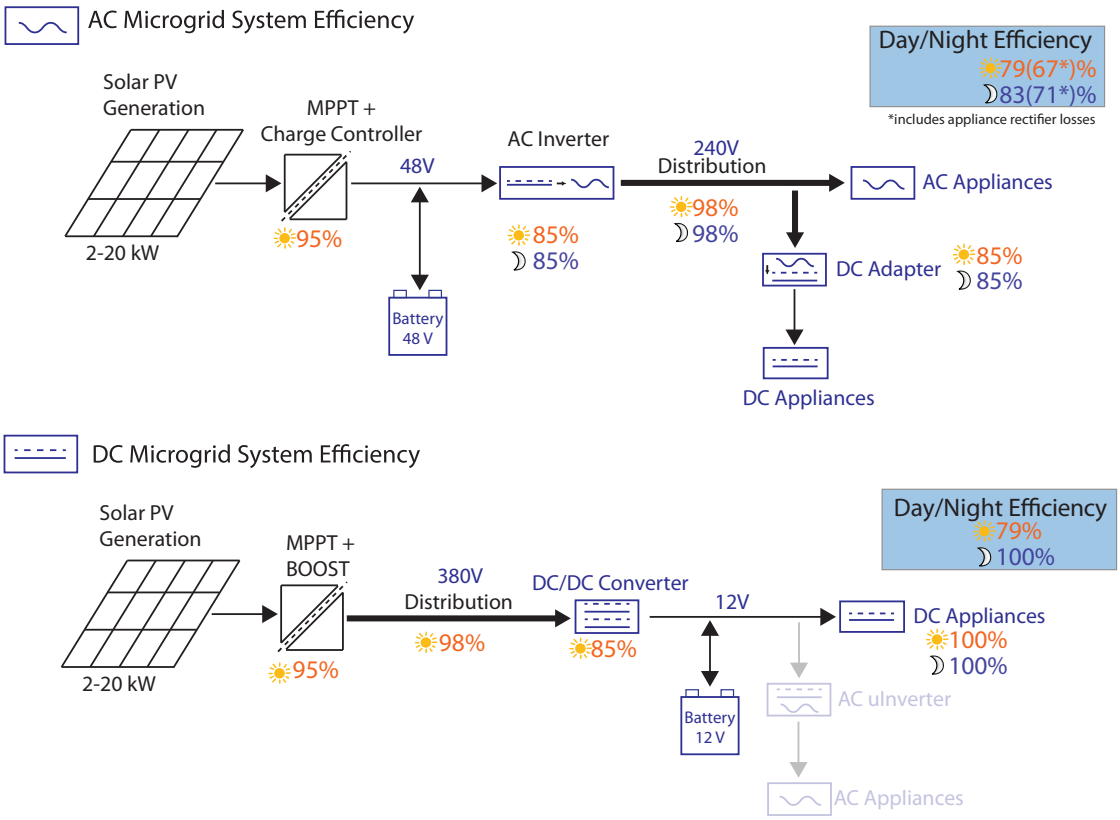

Figure 1.10: AC vs DC microgrids day/night efficiency. Since the efficiency of stored power (η_{stored}) is an important figure of merit, the ability to distribute storage in a DC system allows for minimizing conversion steps on stored electricity[6, 7, 8].

Table 1.2: Comparison of PV costs to battery costs over a 20 year time period—assuming that 100% generated energy is stored.

COST OF SOLAR PANELS	\$1.00 per W
Daily capacity factor (Whrs per W-PV-installed)	5 Whrs
Energy storage requirement at 50% DOD	10Whrs
Cost per Whr of lead-acid batteries	\$0.20 per Whr
No. of replacements over a 20 year time period	4 replacements
TOTAL COST OF BATTERIES	\$8.00 per $W_{PV-Installed}$

Chapter 2

DC Microgrid Architecture Overview

This chapter presents an overview of the architecture of a scalable DC microgrid with distributed storage that was designed for rural electrification in emerging regions. The key system components of the microgrid are described in detail. The distributed voltage-regulation, and power-sharing scheme of the microgrid is also introduced.

2.1 System Description and Overview

An overview of our DC microgrid system is shown in Figure 2.1. There are three key hardware components to the DC microgrid:

1. **Source converters:** The source converter is responsible for operating the grid-connected solar panels at their peak-power point. It is also responsible for detecting and mitigating faults on the grid. The grid voltage is allowed to operate between 360-400 VDC. Fault mitigation, and over-voltage protection are integrated into the functionality of the source converter. A distribution voltage with a range between 360 and 400V is used to keep line losses modest while complying with the emerging standards for high voltage DC power in data centers [26]. The choice also enables use of readily available 600V power semiconductor devices.

2. **Fanout nodes:** The fanout nodes are branch points for power-flow in the microgrid to a local cluster of households. They are also the earthing points of for the grid.

3. **Home Power Management Units (PMUs):** The PMUs are responsible for distributed control of grid voltage and for providing power for 12V DC household batteries and appliances.

A salient property of the DC microgrid architecture is the distributed control of the grid voltage, which enables both instantaneous power sharing and a metric for determining the

available grid power. A droop-voltage power-sharing scheme is implemented, as shown in Figure 2.2, wherein the bus-voltage droops in response to low-supply/high-demand. This droop profile is due to the constant power characteristic of the source converter: a MPPT converter connected to a solar PV installation. The PMUs have a controllable usage profile (load-line), and they can reduce power drawn from the grid by reducing their battery charging load. Switching converters regulated to implement a load-line profile have been shown to have the properties of both large-scale and incremental passivity [27]. Interconnected networks of passive converters have been shown to be stable using Lyapunov techniques [28, 29].

Additionally, the architecture of the DC microgrid aims to minimize the losses associated with stored energy. Since storage is distributed to the individual household PMUs, the number of conversion steps and line losses are reduced. Distributed storage provides reliable provision of electricity 24/7 and also allows for household loads to be decoupled from the grid supply when required. Furthermore, household ownership of batteries enables flexible, demand-driven growth of storage in the grid; each household makes decisions about the size of their storage-capacity based on desired night-time usage.

2.1.1 Distributed Voltage Control

One of the key features to be incorporated in the DC microgrid is the distributed control of the grid-voltage. This allows for instantaneous signaling of power available in the installed generation and enables on-the-fly power-sharing between the connected PMUs. Similar techniques have been explored to enable fast signaling of power-sharing information in DC microgrids [30, 31]. The grid voltage is allowed to operate in a range between 360-400 VDC; Higher voltage indicates more available generation supply. The PMUs have a controllable impedance characteristic, also called load-line (Figure 2.2); A steeper load-line slope indicates a higher demand from the PMU. The load-line slope parameter can be based on information provided through digital communications such as price, as well as internal PMU parameters such as battery charge state.

The superposition of the individual load-lines of the connected PMUs sets the total microgrid demand curve. The intersection of the aggregate demand (aggregate load-line) and the supply (source converter output impedance) provides a unique solution for grid voltage (Figure 2.3). The current drawn by each load PMU is determined by the instantaneous grid voltage operating-point; therefore, power-sharing between PMUs is determined by their relative load-line slopes.

The distributed voltage control scheme allows for load prioritization. Using a digital communication scheme, the relative load-line slopes can be controlled to ensure that sensitive loads (ex. hospitals, water purification facilities) are given a higher priority—i.e. a higher share of the available microgrid-power. The ability to change the demand curve of connected loads also allows for the ability to implement grid-wide demand response schemes.

Implementing a distributed voltage control with the functionality described above is

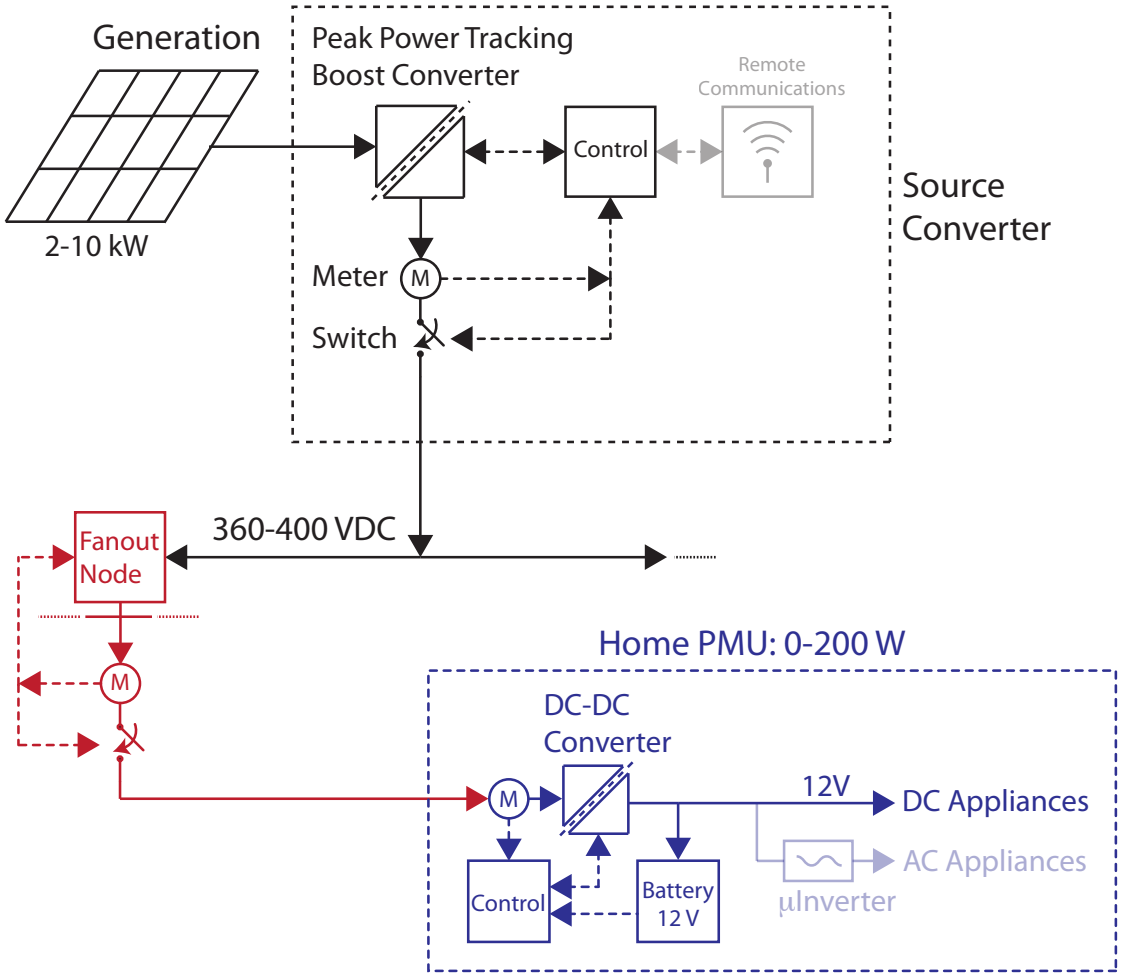

Figure 2.1: DC microgrid system overview. There are 3 main functional component to the microgrid: Source converter, fanout nodes, and home power management units (PMUs).

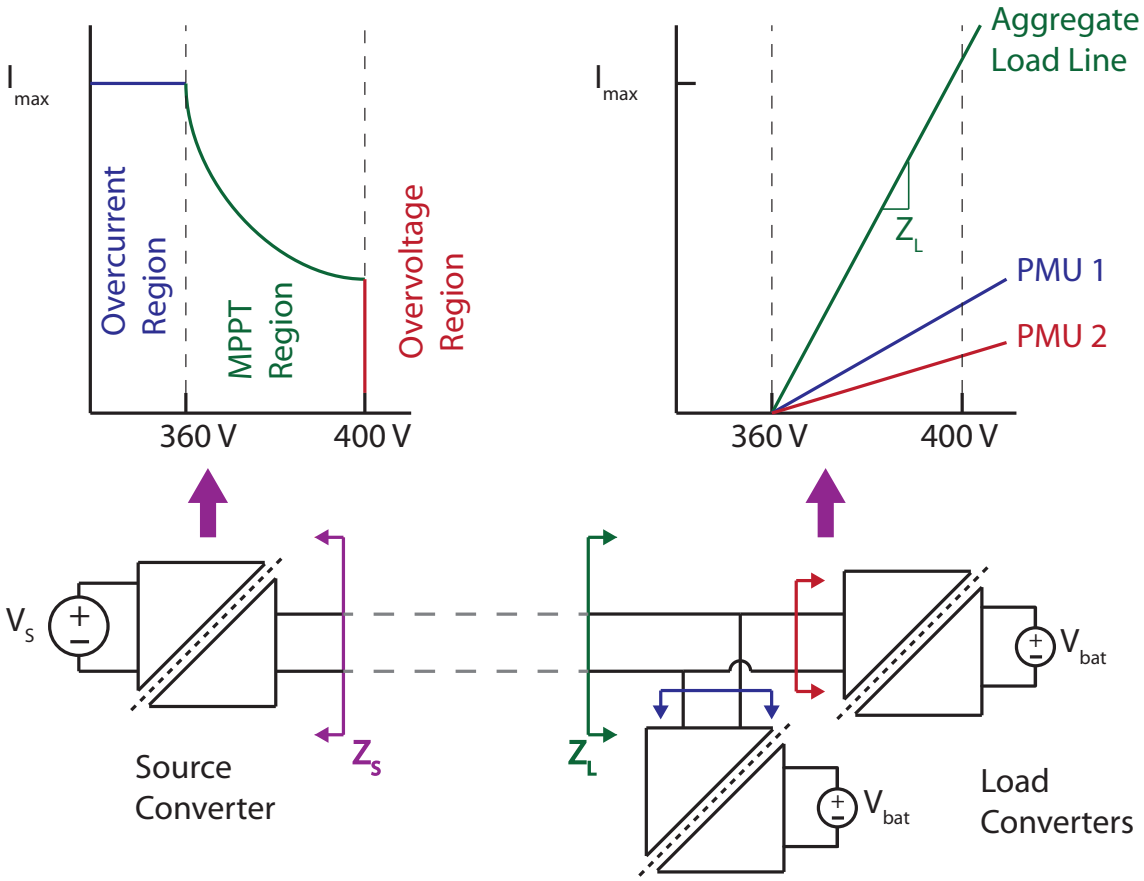

Figure 2.2: Distributed control scheme overview. The output impedance of the source converter has 3 distinct regions. The source converter nominally operates in the MPPT region, where it has the output impedance profile of a constant power source. The available power is dependent on the solar insolation. The load converters (PMUs) present a positive impedance profile to the grid.

dependent on the PMU DC-DC converters having the capacity to control their instantaneous power draw. Typically, in POL power-converters the power drawn is dependent on the connected appliance load. Controlling the instantaneous power draw of a power converter requires the ability to buffer the power drawn by the connected appliances. This is enabled since batteries are integrated with the load converters.

2.1.2 Source Converter

The source converter (Figure 2.4) manages the generation attached to the microgrid; It is responsible for implementing a maximum peak-power tracking (MPPT) algorithm on the grid-connected solar panels. Implementing an MPPT algorithm ensures that the solar panels are operating at their highest efficiency regardless of the incident solar radiation

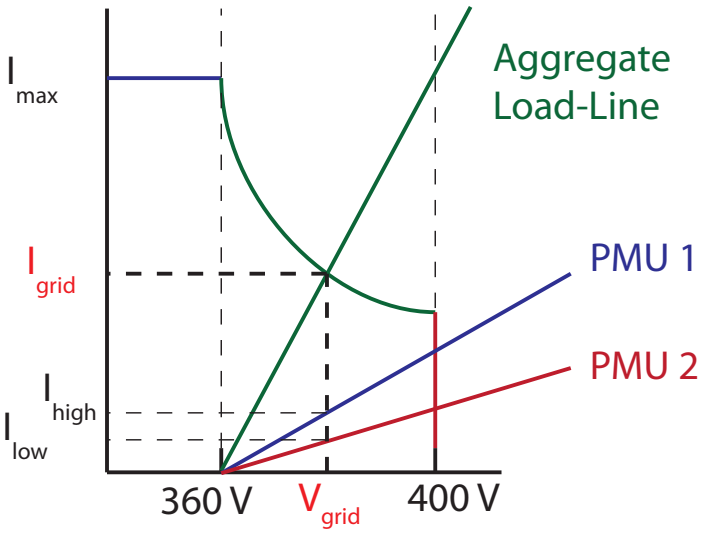

Figure 2.3: An instantaneous operating point of the microgrid is determined by the intersection of load-line and available source-power. The power sharing balance between connected microgrid PMUs is determined by the relative load-line slopes.

(insolation). Since the source converters are implementing an MPPT algorithm on their input terminals, the output characteristic (V-I curve) of source converter is that of a power constrained (constant-power) source. The available power is determined by the insolation on the solar panels.

The source converter is also responsible for fault protection. There are two modes of protection—over-voltage (open-circuit) protection and over-current (short-circuit) protection. The protection modes are shown in the output V-I profile of the source converter in Figure 2.2. In cases of open-circuit faults or light-load conditions—i.e. when microgrid loads are not drawing sufficient power from the grid—the over-voltage protection ensures that the voltage of the distribution (380V) bus is prevented from rising above 400V. Effectively the MPPT functionality of the source converter is detuned and less power is extracted from the connected solar panels.

Over-current (fault) protection for the 380V bus is also implemented at the source converter. Fault-protection is needed to ensure that both line-to-line and line-to-ground faults are detected and mitigated. Fault-protection minimizes safety risks to humans and electronic equipment. The protection scheme implemented on the 380V bus is described in detail in Chapter 5.

2.1.3 Fanout Node

The fanout nodes are the branch points for the microgrid system. They are primarily responsible for the metering and grounding for a local cluster of households. The microgrid uses a multiple-point grounding system and the fanout nodes are the grounding points

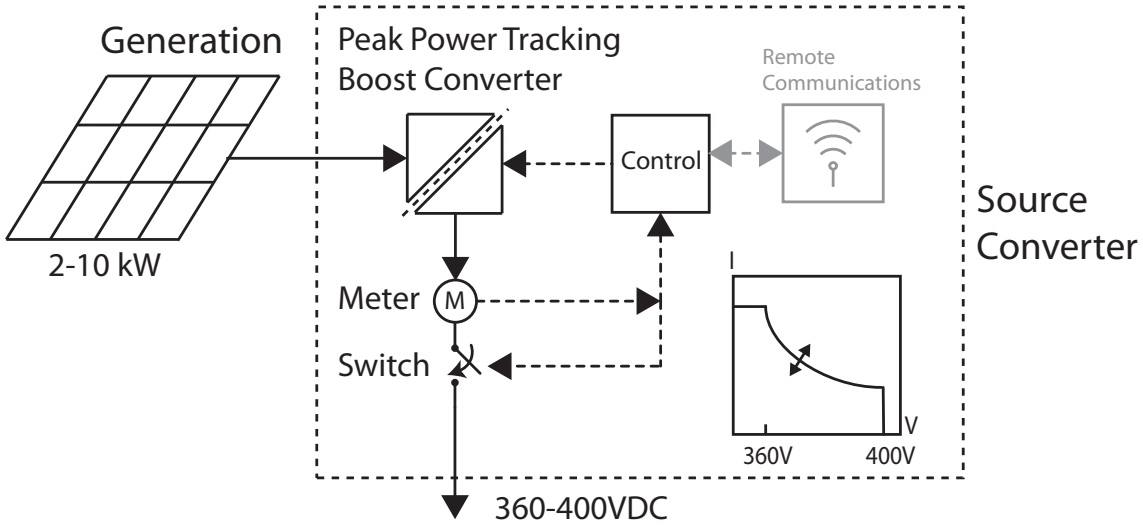

Figure 2.4: Block diagram of the source converter and all the functionality entailed. Show MPPT block, over-voltage block, fault-protection and grounding block, and digital communications block. in each block highlight the features of the block. Perhaps relative importance of the blocks.

for the local cluster. This is further described in Chapter 5.

In the case of a 2-stage conversion architecture as described in Chapter 4, the fanout nodes integrate a bus converter to further step down from the high distribution bus voltage (380V) to a lower intermediate voltage (48V).

In addition, the fanout nodes are intended to be metering and aggregation points for the microgrid. Metering is needed in order to ensure that losses of of power are accounted for. Power losses can include losses from theft and faulty equipment.

2.1.4 Power Management Units

The power management units are responsible for converting the grid voltage to 12 V for battery charging and home appliance use. The batteries are integrated at the output of the DC-DC converter of the power management unit. As described in Section 2.1.1, the PMUs implement a load-line control scheme to stabilize grid voltage and enable control of power flow in the grid. The load-line regulation scheme is enforced by controlling the impedance at the input terminals of the PMU, i.e. the current drawn by a PMU is a function of the grid voltage and is set by a controllable load-line slope and set-point parameters. The slope of the load-line determines the effective "demand" of a given PMU. The set-point of the load-line determines the lowest voltage at which a PMU draws power from the grid. A block diagram of the PMU is shown in Figure 2.6. The slope and the set-point of the PMU load-line can be changed based on factors such as the price of grid power and the charge state of the PMU battery. The interplay between relative PMU load-

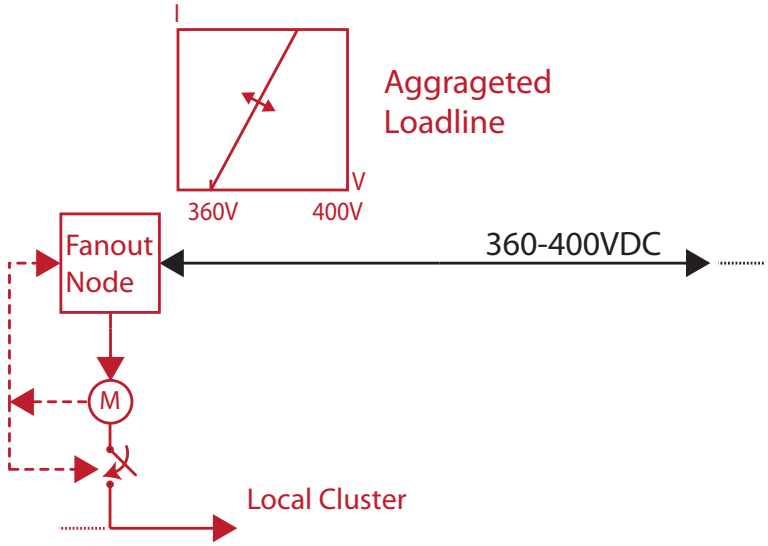

Figure 2.5: Block diagram of a fanout node. Fanout nodes are branch points for local clusters of houses. They are also grounding points for the microgrid.

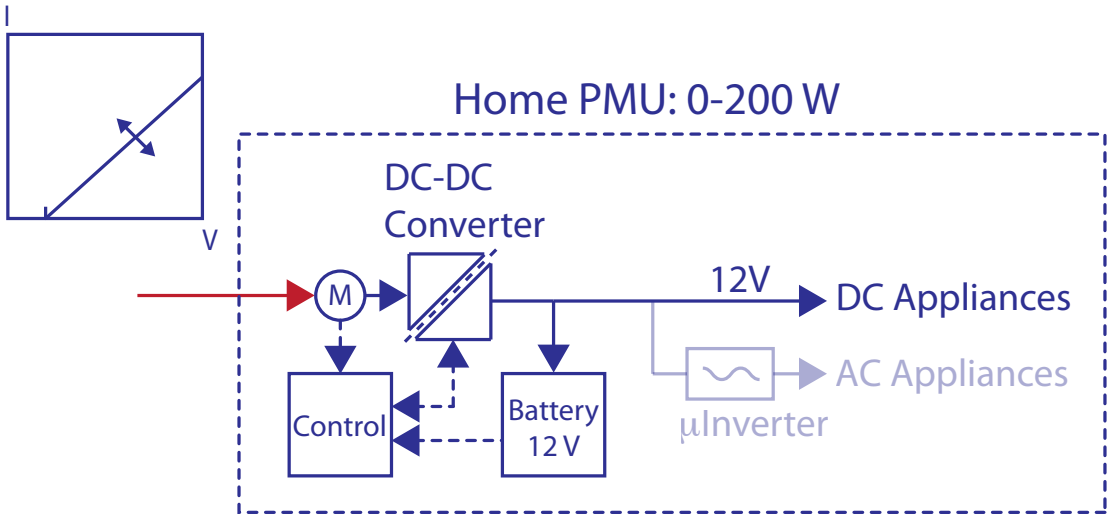

Figure 2.6: Block diagram of PMU functionality. The main functional blocks are the load-line control block that controls the power conversion block

line slopes and set-points can be used to reach a wide range of microgrid power-sharing operating points.

There are two different hardware versions of the PMU presented in the following chapters. In Chapter 3, a phase-shifted full-bridge topology is utilized to convert from the 380V bus to 12V for household use in a single-conversion-step. In Chapter 4 a buck topology is utilized to convert from an intermediate 48V bus (generated by bus converters integrated into the fanout nodes) to 12V for household usage.

Chapter 3

Phase Shifted Full Bridge Topology

The first generation prototype of the scalable DC microgrid for rural electrification in emerging regions is presented in this chapter. The microgrid architecture was designed around a single-stage, isolated, step-down conversion from 380V to 12V at each home power management unit (PMU). This specification was met with a transformer isolated PSFB topology which was rated for 400 W. This chapter presents an analytical analysis of the PSFB topology. Simulation results for PSFB converters implementing a distributed (load-line) microgrid voltage regulation scheme are also presented. In addition, experimental results from a microgrid testbed are shown. The work presented in this chapter was published in [27].

3.1 Overview of Architecture

An overview of the first generation of DC microgrid architecture is shown in Figure 3.1. The key components of the system are the source converter, fanout nodes, and the home PMUs. The source converter is responsible for operating the solar panels at their peak-power point as well as detecting and mitigating faults on the grid. The grid distribution voltage is allowed to operate between 360-400V and over-current and over-voltage protection is integrated into the functionality of the source converter. The grid voltage is a signaling mechanism to the PMUs connected to the grid for available power at the source converter. The fanout nodes are grid branch points that are responsible for switching and metering usage from a local cluster of houses; this functionality helps in deterring theft of power as well as isolating faults on the grid. Fanout nodes are also the grounding points for the microgrid. Finally, the PMUs are responsible for distributed control of grid voltage and for powering for the household appliances and battery charging.

3.1.1 Distributed Voltage Control

As described in Chapter 2, one of the key features of the DC microgrid is the distributed control of the grid-voltage. This allows for instantaneous signaling of power

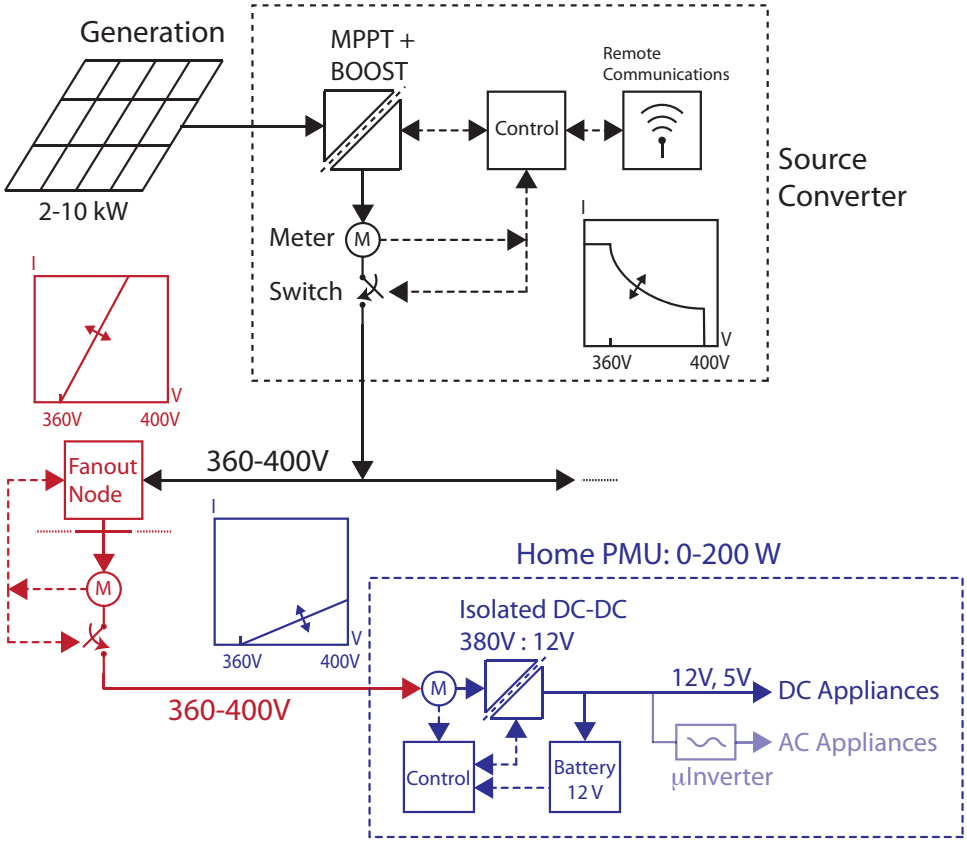

Figure 3.1: Overview of the key components of the DC microgrid system with distributed storage and their functional blocks.

available in the source converter and enables control of power-sharing between the connected PMUs. The source-converter allows the voltage to operate in a range between 360-400V. A higher voltage indicates more available generation supply on the grid relative to the current load power demand. The PMU power converters have a controllable current-vs-voltage profile, called the load-line (Figure 3.2). The slope of the load-line parameter indicates the instantaneous demand of a PMU. Power sharing between the connected PMUs is determined by the relative slopes and set-points of the individual PMU load-lines.

3.1.2 Source Converter Architecture

The source converter operates its connected solar-panels at their peak power point and has the following characteristics:

1. The source converter uses a 400W 2-phase boost topology with a digital control scheme.

2. The source converter implements an MPPT algorithm on the solar panels connected to the input terminals.

3. The converter incorporates over-current and over-voltage protection on its output terminals, but does not directly regulate the voltage on the 380V bus. Instead while the connected solar panels are operating at peak power, the output characteristic of a source converter is that of a constant power source. As the available insolation to the solar panels changes, the grid voltage also changes accordingly reflecting available grid power. The variability in grid voltage is a signal to the connected loads (PMUs) and is stabilized by response of the PMUs as described in the Section 3.2.

4. In a field implementation, the source converter also incorporates a digital communications block to aggregate usage from the grid-connected PMUs. It also transmits pricing information so that the PMUs can tailor their demand in response.

3.1.3 Power Management Unit Architecture

The PMUs are responsible for converting the grid voltage down to 12V for household usage and battery charging. The PMU power converters are designed such that their input impedance (load-line) is regulated in order to stabilize grid voltage and enable power-sharing between multiple units. The PMUs consist of the following functional blocks:

1. A phase shifted full bridge (PSFB) converter that converts the grid distribution voltage from 360-400V to the 12V household level.

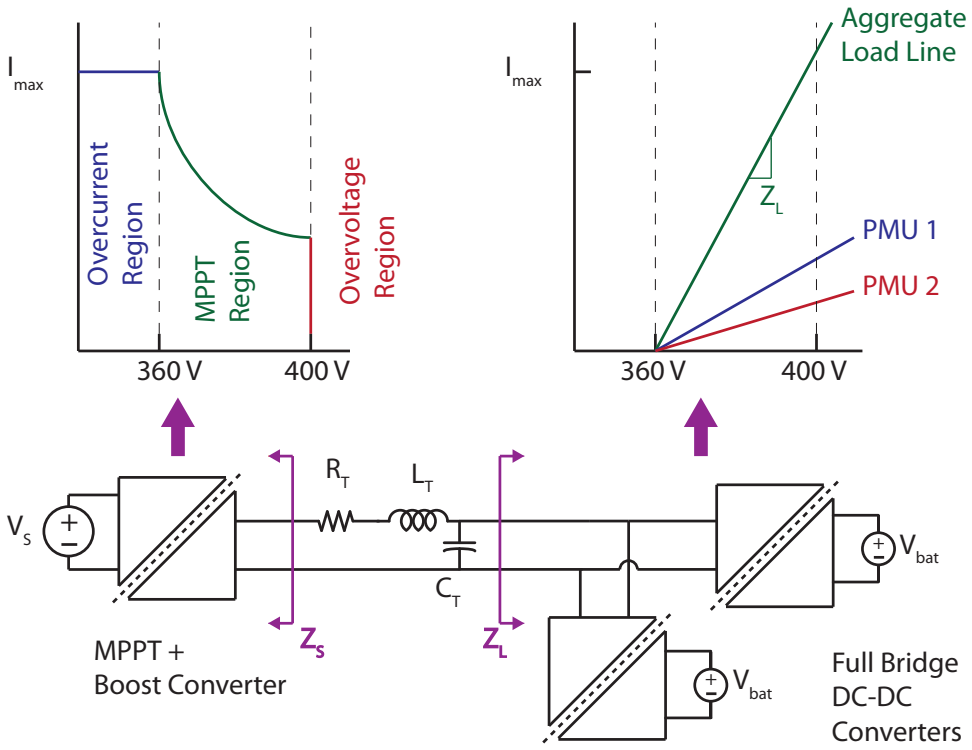

Figure 3.2: Overview of a microgrid with two PMUs connected to a single source-converter. The source impedance reflects maximum power available from the solar panels. When in the MPPT region, the source impedance curve is that of a constant power source. The power in this region varies as a function of solar panel insolation. The aggregate load-lines reflects the aggregate input-impedance of the PMUs as a function of grid-voltage. A unique grid-voltage operating point is formed at the intersection of the source output-impedance and the aggregate load-line. The grid-voltage operating point changes dynamically with insolation and changes in aggregate power demand from the microgrid loads.

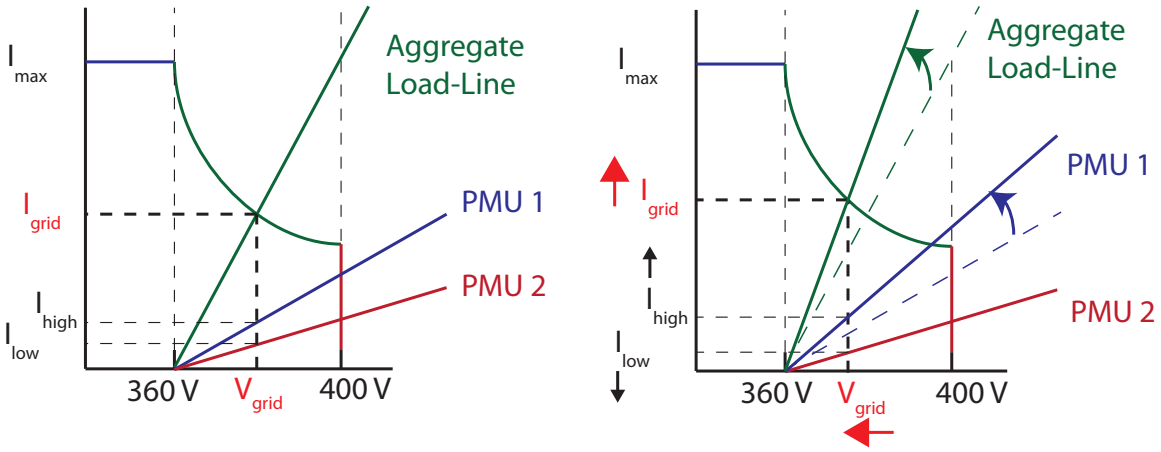

Figure 3.3: Overview of the response of grid voltage to a change in load conditions. PMU 1 increases the slope of its load-line and changes the set-point of the grid voltage. The change in set-point results in greater power going to PMU 1 and less power going to PMU 2.

2. Integrated, scalable battery storage that enables the PMUs to store energy at the households and decouple PMU power-draw from house appliance usage; this allows for distributed stabilization of grid-voltage.

3. A communications block that enables sharing of usage information and remote management.

3.2 Theory of Operation and Analysis

The design of PMUs and the load-line control scheme ensure stability of the grid voltage in response to a wide range of disturbances. The steady-state grid-voltage is determined by the intersection of the aggregate load-line and the power available from the source converter. A change in load-conditions results in a new grid-voltage operating point as shown in Figure 3.3. The power drawn by each PMU is dependent on the grid-voltage operating point. The power-sharing ratio between individual PMUs is determined by the relative slopes of their load-lines.

The circuit topology used for power-conversion in the PMUs is a PSFB converter (Figure 3.4). In addition to having the favorable property of magnetic isolation, the transformer-isolated PSFB converter also easily enables zero-voltage switching by utilizing the leakage inductance of the transformer [32].

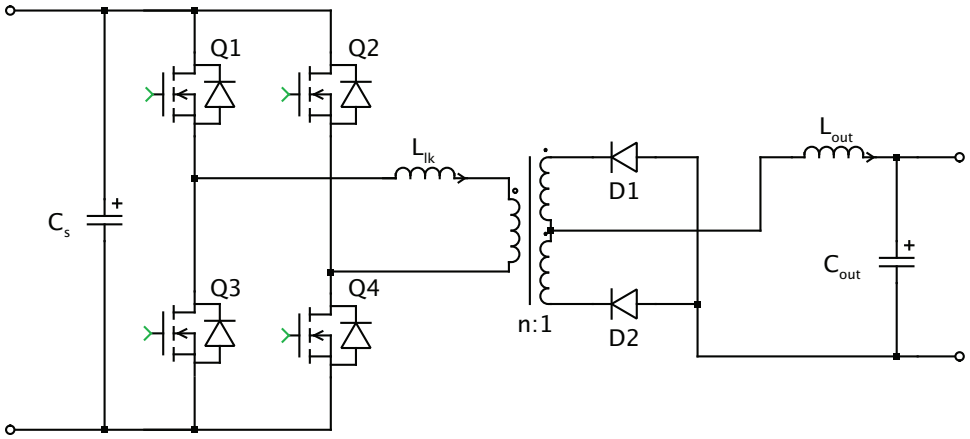

Figure 3.4: Basic Phase-Shifted Full-Bridge DC-DC converter schematic. For the experimental converter presented in this chapter: $L_{lk} = 26\mu H$, $n = 2$, $C_s = 330\mu F$, $L_{out} = 10\mu H$, and $C_{out} = 7500\mu F$.

3.2.1 Open-loop Characteristics of PSFB Converter

The PSFB topology is a buck-derived topology and lends itself to analysis by using a PWM buck converter as an analogous circuit. However, the leakage inductance causes the small-signal behavior to diverge from that of a buck converter. The small signal behavior of the PSFB topology has been analyzed in depth by numerous past papers [33, 34]. The impact of the leakage inductance is analogous to current feedback and has a damping effect on the circuit. For the purpose of analysis in this dissertation we make the simplifying assumption that the variation in current through the output inductor L_{out}, and the variation in voltage across the capacitors C_s and C_{out} are small compared to the nominal values of those quantities over a switching period. This assumption simplifies the analysis of the small-signal model but still accounts for the first-order effects of the leakage inductance. Choosing the current through L_{out} and the voltage across C_s as the state variables the system of equations that determine the the operation of the converter are shown to be:

$$L\frac{\mathrm{d}I_l}{\mathrm{dt}} = D_{eff} \cdot \frac{1}{n} \cdot V_c - V_{out} \tag{3.1}$$

$$C\frac{\mathrm{d}V_c}{\mathrm{dt}} = I_s - D_{eff} \cdot \frac{1}{n} \cdot I_l \tag{3.2}$$

where I_s is the input current from the grid, n is the turns ratio of the primary windings to the secondary windings of the transformer (n_p/n_s), V_{out} is the battery voltage and hence assumed to be constant, $L = L_{out}$, $C = C_s$, and D_{eff} is the effective duty ratio defined as:

$$D_{eff} = D_{nom} - \Delta D \tag{3.3}$$

where ΔD is the deviation from the nominal duty cycle caused by leakage inductance commutation, which can be approximated as:

$$\Delta D = \frac{1}{\frac{V_s}{L_{lk}} \cdot \frac{T_s}{2}} \cdot 2 \cdot \frac{I_l}{n} = \frac{R_l}{V_s} \cdot \frac{I_l}{n} \tag{3.4}$$

where $R_l = 4 \cdot L_{lk}/T_s$.

Solving for the steady-state operating point of the converter we get that:

$$I_l = \frac{I_s \cdot V_{out} \cdot n}{D_{nom} \cdot V_{out} - I_s \cdot R_l/n} \tag{3.5}$$

$$V_c = \frac{V_{out}^2 \cdot n}{D_{nom} \cdot V_{out} - I_s \cdot R_l/n} \tag{3.6}$$

Figure 3.5 shows the open-loop characteristic under constant duty cycle of the steady-state input current as a function of input voltage. The curves show that at a constant duty cycle, the input current is directly proportional to input voltage. This effect is due to the relationship between I_s and V_c as shown in (3.6). The current-feedback effect caused by the leakage inductance makes the effective impedance of the PMU on the grid always positive. Additional feedback can enhance (or modify) this characteristic as will be shown below.

The small-signal perturbation state-space model can be derived from the large-signal equations (3.1-3.4) above and it takes the form:

$$\dot{x} = A \cdot x + b_1 \cdot \hat{d} + b_2 \cdot \hat{i_s} + b_3 \cdot \hat{v_{out}} \tag{3.7}$$

where $x = [\ \hat{i_l} \quad \hat{v_c}\ ]^t$ and all system variables: $[\ \hat{i_l} \quad \hat{v_c} \quad \hat{d} \quad \hat{i_s} \quad \hat{v_{out}}\ ]$, are perturbations from nominal operating points. The relevant matrices of the system are:

$$A = \begin{bmatrix} -R_l/L \cdot n^2 & D_{nom}/L \cdot n \\ 1/C \cdot (2 \cdot R_l \cdot I_l/V_c \cdot n^2 - D_{nom}/n) & -R_l \cdot I_l^2/C \cdot V_c^2 \cdot n^2 \end{bmatrix}$$

$$b_1 = \begin{bmatrix} V_c/(n \cdot L) \\ -I_l/(n \cdot C) \end{bmatrix}$$

$$b_2 = \begin{bmatrix} 0 \\ 1/C \end{bmatrix}$$

$$b_3 = \begin{bmatrix} -1/L \\ 0 \end{bmatrix}$$

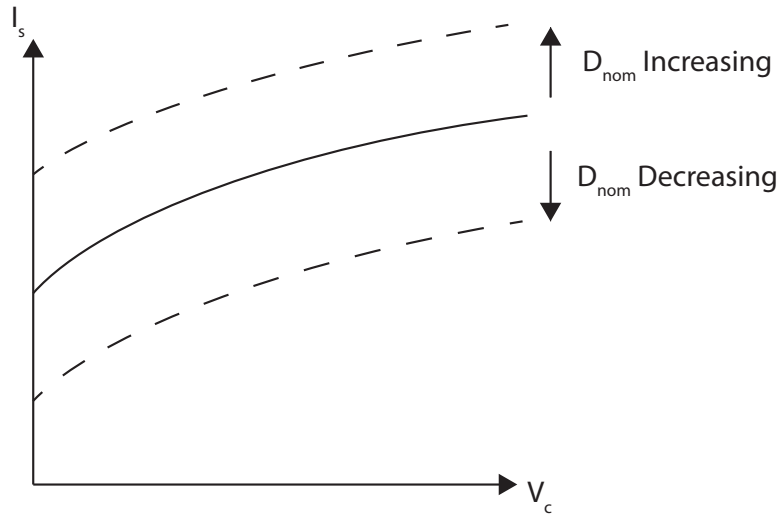

Figure 3.5: Open-loop steady-state response of input current (I_s) to input capacitor voltage (V_c) of a phase-shifted full bridge converter .

We can derive transfer functions and impedance functions for the converter from (3.7). An example of the small-signal response of the input-capacitor voltage ($\hat{v_c}$) to a change in the duty cycle is shown in Figure 3.6. The leakage inductance has a damping effect on the response of $\hat{v_c}$. The open-loop input impedance (i.e. response of $\hat{v_c}$ to $\hat{i_s}$) shown in Figure 3.7 also highlights the damping effect due to L_{lk} in the PSFB converter. As mentioned in Chapter 2, this characteristic opens up the possibility of utilizing network passivity concepts to make an argument for large-scale grid stability of multiple-interconnected PMUs even in the case of open-loop operation [28, 29].

3.2.2 Closed-Loop Response of Phase-Shifted Full-Bridge Converter

As explained in Section 3.2, the desired control objective of the PMUs is to present a load-line profile to the grid, i.e. the PMUs should behave as controllable positive impedances to stabilize the grid voltage to a unique operating point under each set of source and load conditions. The choice of PSFB topology has the favorable properties of both large-signal and incremental passivity under open-loop operation; Such converters have been shown to be stable using Lyapunov based arguments [29]. The desired load-line controller would enforce the following relationship between the input current (I_s) and the input-capacitor voltage (V_c):

$$I_s = G_{desired}(V_c - V_{ref}) \tag{3.8}$$

where $G_{desired}$ is the desired slope of the load-line and V_{ref} is the cut-off grid-voltage as shown in Figures 3.2 & 3.3.

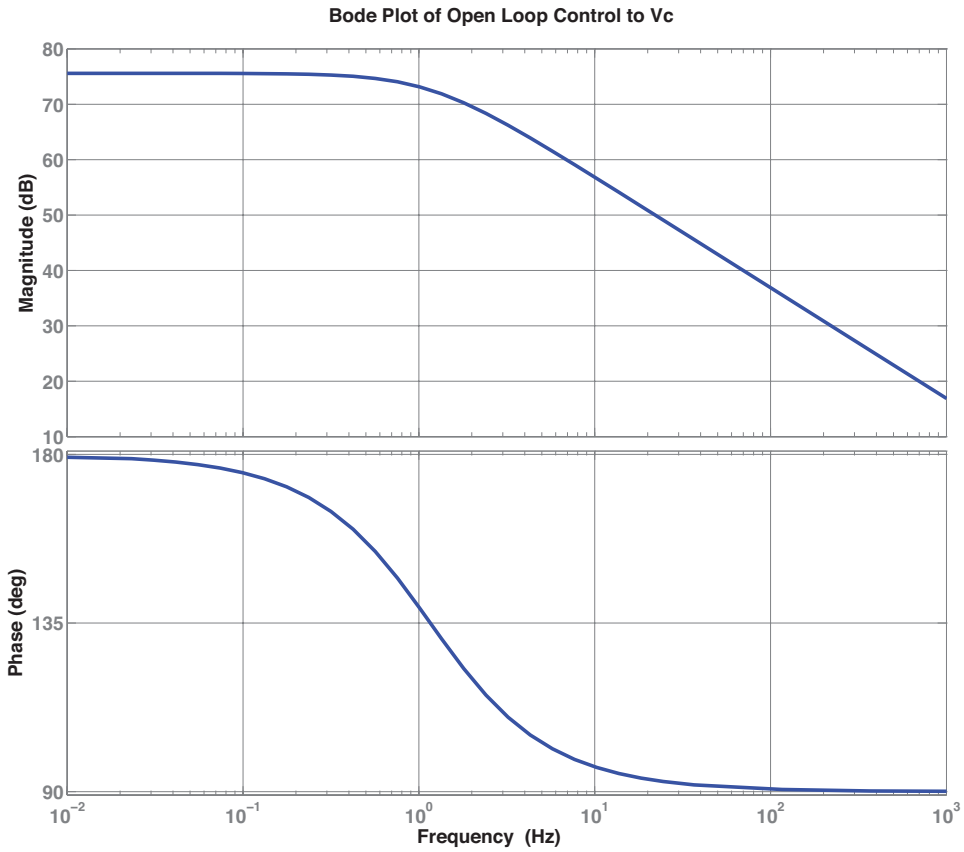

Figure 3.6: Control to input-capacitor-voltage transfer function ($\hat{v_c}(s)/\hat{d}(s)$) of the PS-full bridge converter. The phase characteristic indicates an inverse relationship between $\hat{d}(s)$ and $\hat{v_c}(s)$.

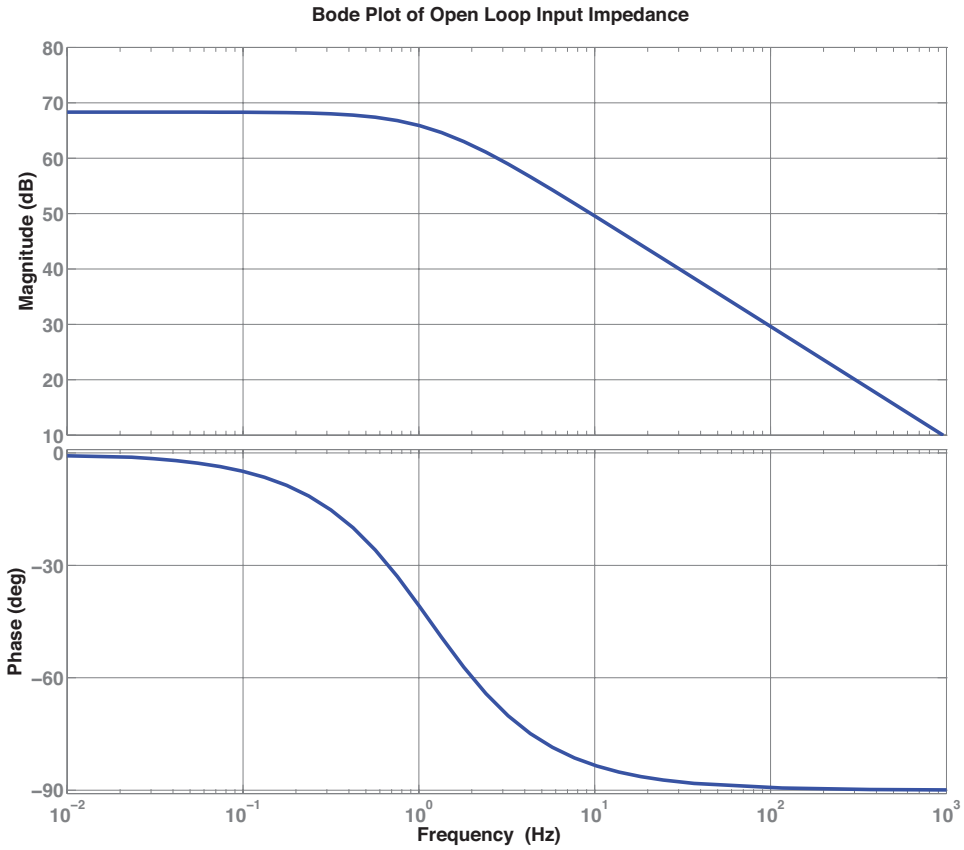

Figure 3.7: Open-loop input-impedance ($\hat{v_c}(s)/\hat{i_s}(s)$) of the PS-full bridge converter.

It is possible to regulate the slope of the load-line of an individual PMU through proportional feedback of $V_c - V_{ref}$ to the reference of a current controller, I_{ref}. A schematic of the feedback scheme is shown in Figure 3.8. The current through the primary winding, I_{pri}, is the sensed circuit variable, I_{sense}, for the current control minor loop. Using the assumption that the current control loop removes the dynamics of the L_{lk} and L_{out} inductors in the converter, i.e. $I_{pri} = I_{ref}$, there is a direct relationship between I_{ref} and the current through the output inductor, I_{out},

$$n \cdot I_{ref} = I_{out} \tag{3.9}$$

Using the conservation of power relationship between the input and the output terminals of the converter,

$$V_c \cdot I_s = V_{out} \cdot I_{out} \tag{3.10}$$

the relationship between I_{ref} and I_s is derived to be:

$$I_{ref} = \frac{I_s}{n} \cdot \frac{V_c}{V_{out}} \tag{3.11}$$

To enforce the load-line relationship 3.8, the equation for I_{ref} is derived as:

$$I_{ref} = K_p \cdot G_{desired} \cdot (V_c - V_{ref}) \tag{3.12}$$

where $K_p = V_c/n \cdot V_{out}$. V_c is the sensed circuit variable used to generate I_{ref}. I_{ref} is the reference command to the current control minor loop. In practice a nominal value for K_p, is used to generate I_{ref} as shown in Figure 3.8. This simplification is used since there is less than 5% deviation of K_p from its nominal value over the entire operating range of V_c. The large-signal load-line behavior does not deviate significantly from 3.8 with this simplification as is shown from the PLECS simulation results in Figure 3.9.

Using the control scheme described above, the small-signal closed-loop input impedance of the PSFB converter has a single-pole response:

$$\frac{\hat{v_c}(s)}{\hat{i_s}(s)} = \frac{1}{G_{desired} + C_s \cdot s} \tag{3.13}$$

A bode plot of the input impedance generated from a simulation of the converter is shown in Figure 3.10. The favorable large and small-signal characteristics of the load-line feedback control scheme allow for utilizing network passivity concepts to justify global stability of a networked system with multiple independently operating PMUs regulating the grid-voltage over the full range of operating conditions [29].

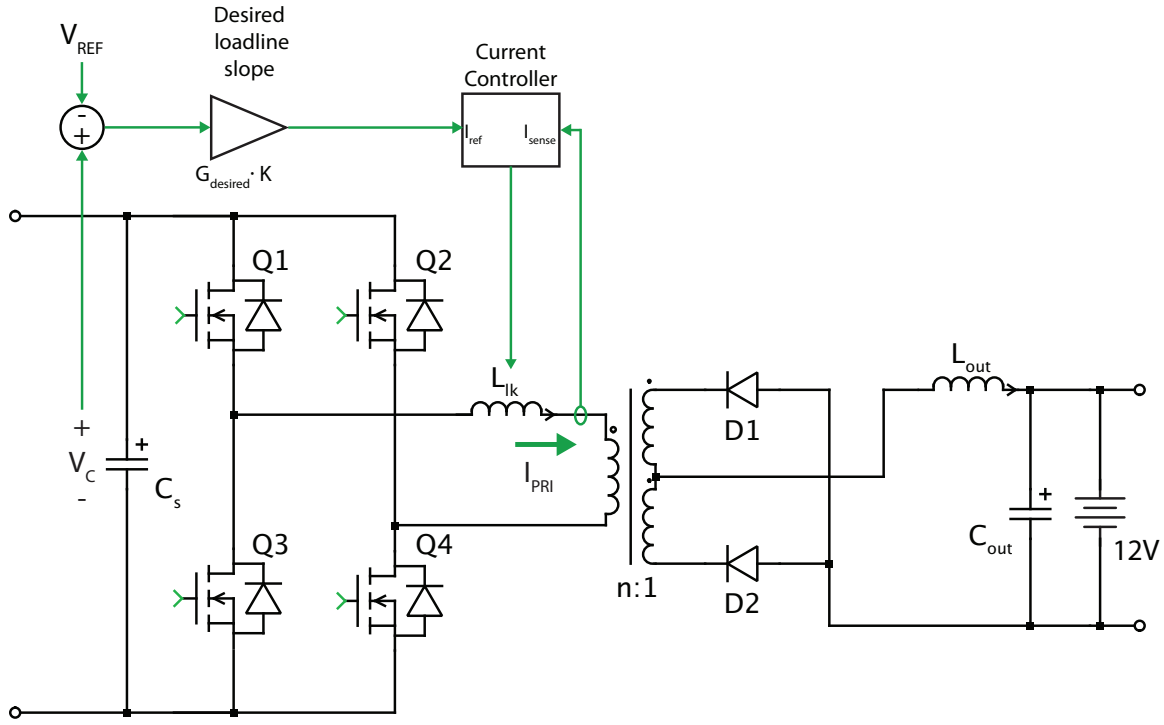

Figure 3.8: Schematic of PSFB converter with a current controller and proportional feedback of V_c.

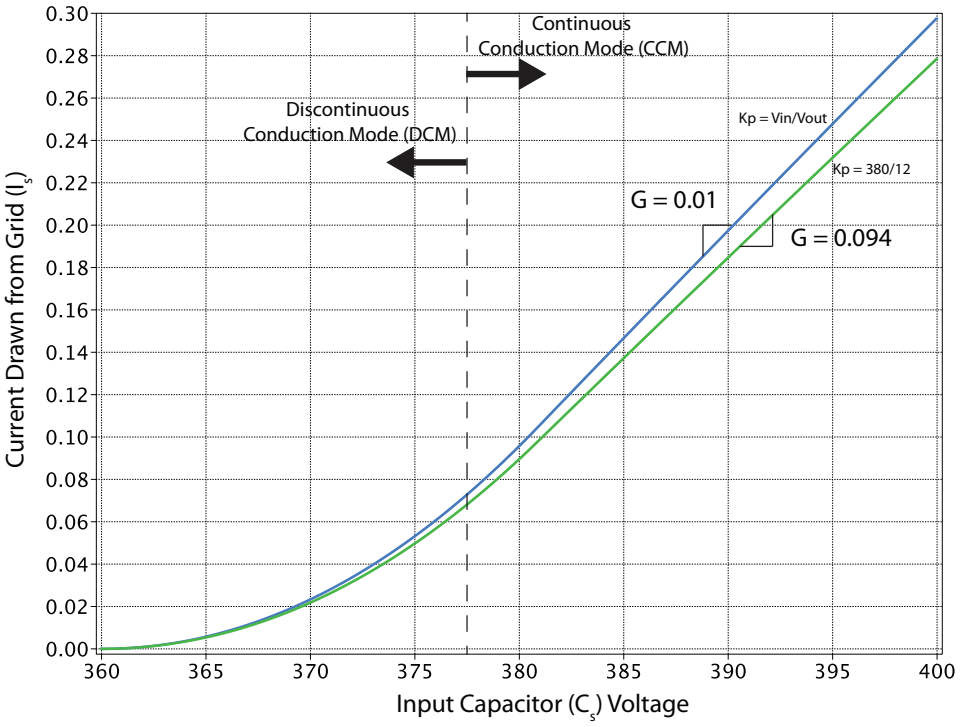

Figure 3.9: Simulation of the large signal relationship between V_c and I_{in} with closed-loop load-line control scheme. The initial deviation of the slope is caused by the converter operating in discontinuous conduction mode. Once the converter is operating in continuous conduction mode, the slope of the load-line is constant. A nominal value of K_p is used, but does not cause a significant deviation in the large-signal behavior from the desired response.

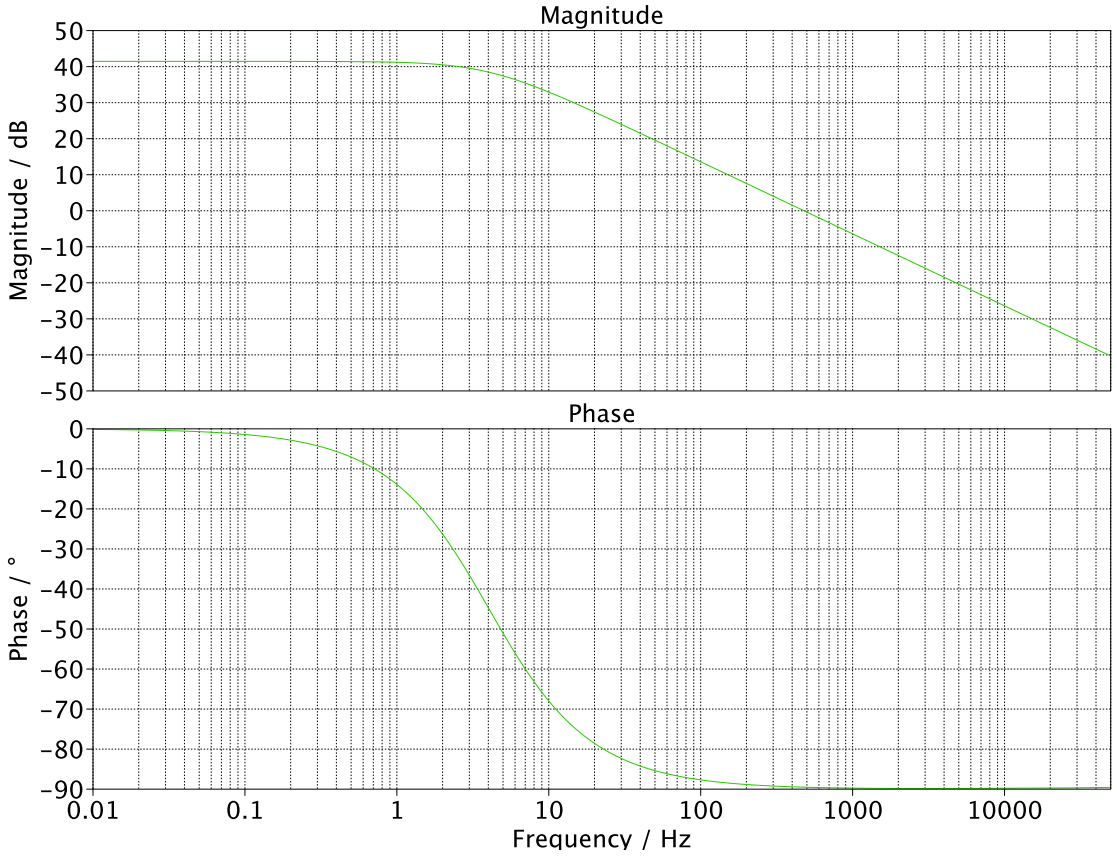

Figure 3.10: Closed-loop, small-signal input-impedance ($\hat{v_c}(s)/\hat{i_s}(s)$) of the PSFB converter. $G_{desired}$ was set as 0.01 and the low frequency response of the input-impedance reflects this value: $20 \cdot log(1/.01) = 40dB$. The corner frequency is given by C_s and $G_{desired}$, $f_p = G_{desired}/C_s \cdot 2 \cdot \pi = 4.8Hz$.

3.3 Grid Dynamics Simulation Results

In this section, results obtained using the PLECS simulation toolset are used to verify grid-voltage stability. The simulation setup is shown in Figure 3.11a. The values of resistance and inductance are worst-case parameter estimates based on using a 14 AWG transmission line over a distance of 0.5 km. A simple topology of 2 PMUs connected to a constant power source is used for the simulations presented in this section. The constant power source is modeled with the source boost converter operating in constant source current mode with a voltage input that is provided by a standard dc bench supply. Since both the input power and the input current are regulated, i.e. $P_{in-source} = V_{in-source} \cdot I_{cmd-in-source}$, the output of the boost converter models a constant power source, where $I_{source} = P_{in}/V_{grid}$.

Figure 3.11b shows the response of grid voltages and PMU currents to step changes in input power. The PMUs draw power proportional to their load-line slopes. In the case of Figure 3.11b. The grid-voltage stabilizes to a new steady-state solution after a transient period and the response of grid voltage exhibits a damped behavior that is in agreement with the analysis carried out in the previous section. The PMUs both increase their power draw in response to rising grid-voltage. This behavior ensures stability of the grid-voltage under changing power-conditions.

3.4 Experimental Results

Experimental validation of simulation and analysis results were performed by modifying commercially available converter evaluation kits[35, 36]. Figure 3.12 shows photos of the source converter and PMU, and Table 3.1 has the specifications and ratings. Both converters are digitally controlled; the firmware on the embedded controllers for both topologies was modified to achieve the desired functionality. Figure 3.12c shows the experimental hardware connected to a $400W$ PV installation. The rooftop installation was run over the course of the day and the PMUs charged their attached batteries and regulated the distribution voltage.

The response of the PSFB PMU over the full range of grid voltage is shown in Figure 3.13. The load-line parameters are set such that $G = .01$ and $V_{ref} = 350V$. The discrepancy from the simulation results is due to the loss mechanics of the power electronics components as well as parameters such as: i) slope compensation of the current loop; and ii) the deadtime compensation, which are not included in the simulation model.

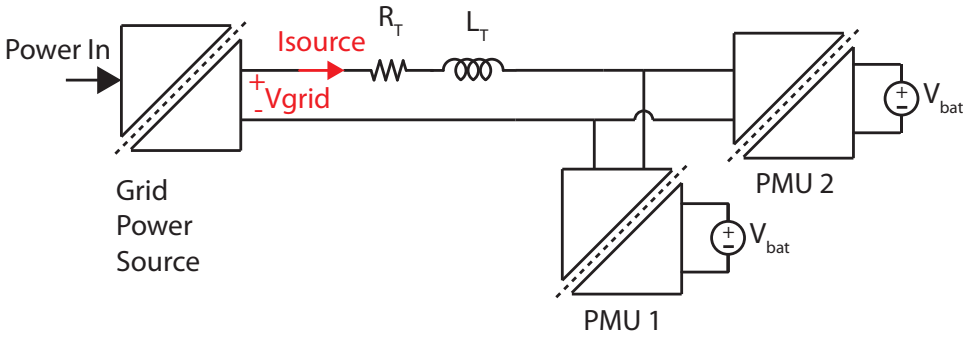

(a) Simulation setup used in PLECS with a single constant-power source connected to two closely located PMUs. $R_T = 10\Omega$, and $L_T = 10\mu H$ are the transmission-line parameters.

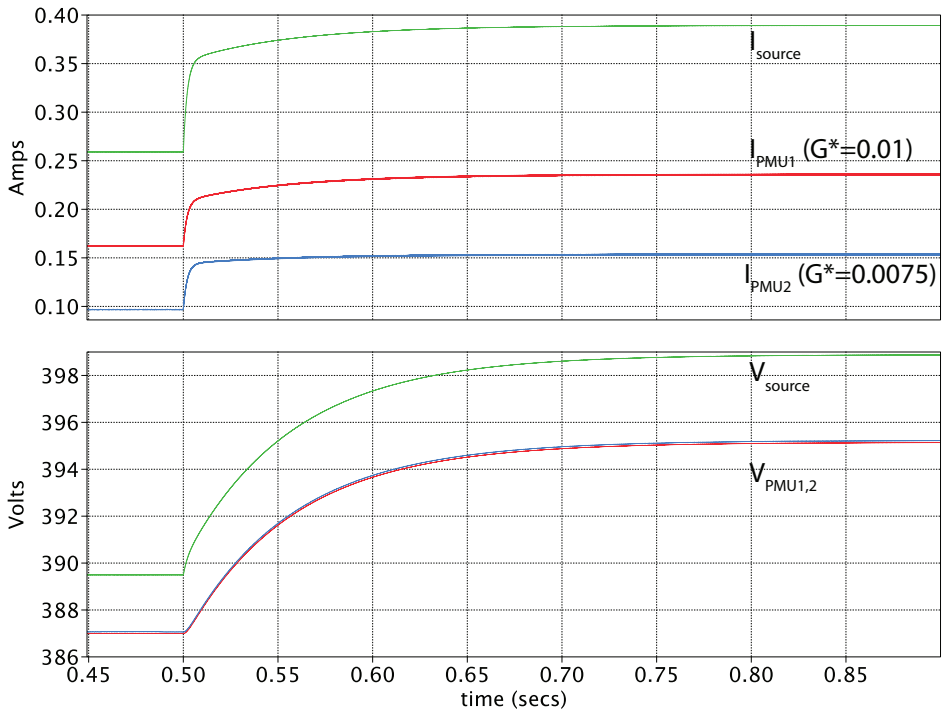

(b) Simulated response of grid-voltage to a step change in input power.At time $t = 0.5s$, the input power is increased from $100W \rightarrow 150W$. The grid voltage rises in response to the increase in input power. This rise in grid voltage is in turn stabilized by the PMUs drawing more current as the voltage increases.

Figure 3.11: Simulation of step change in microgrid power to a system of two PMUs

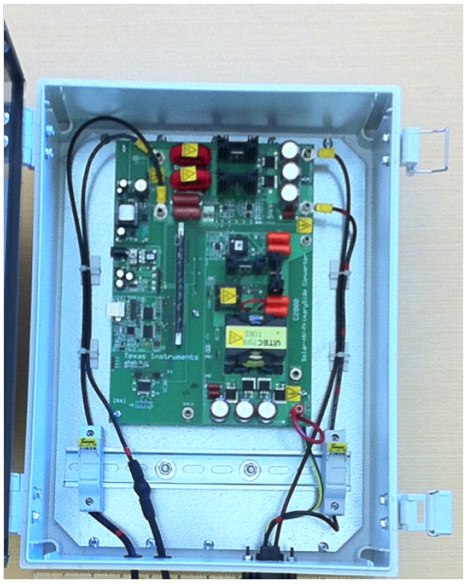

(a) 400W 2-phase boost source converter.

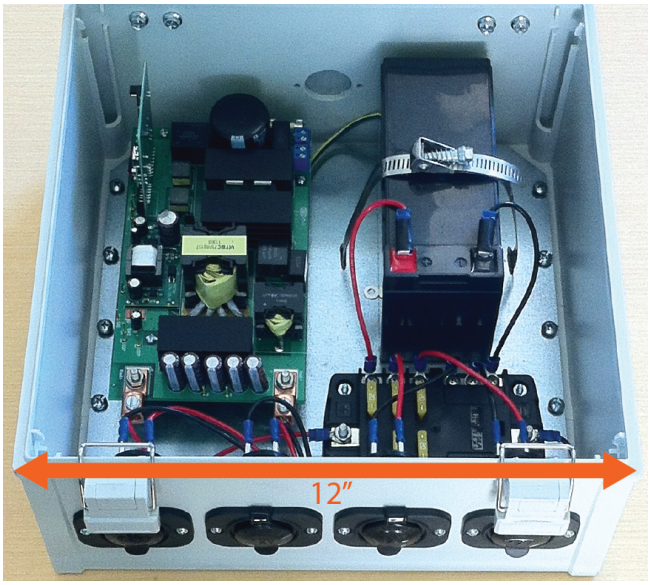

(b) 600W PSFB converter with a 12V 8A-hr lead acid battery for storage.

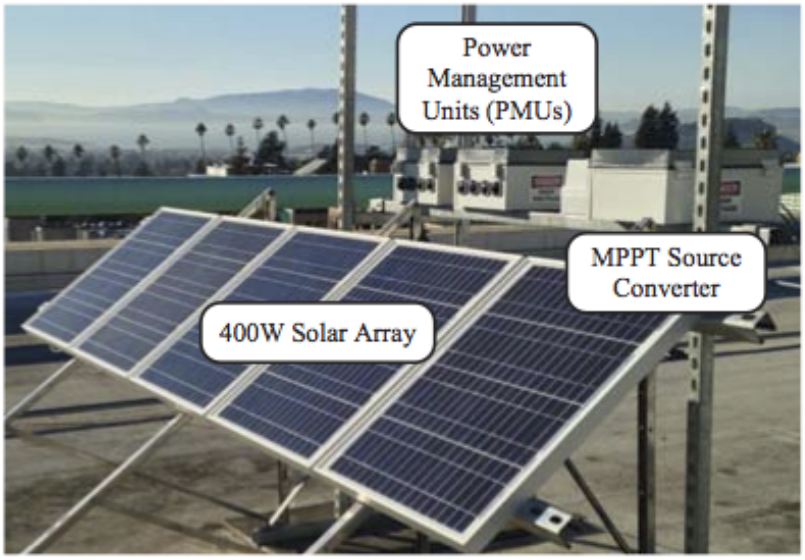

(c) Rooftop setup with 400W solar PV installation. The source converter regulates the solar panels to operate at their peak power point. 2 PMUs are connected to the output of the source converter and regulate the distribution bus voltage.

Figure 3.12: Pictures of prototype hardware in microgrid testbed.

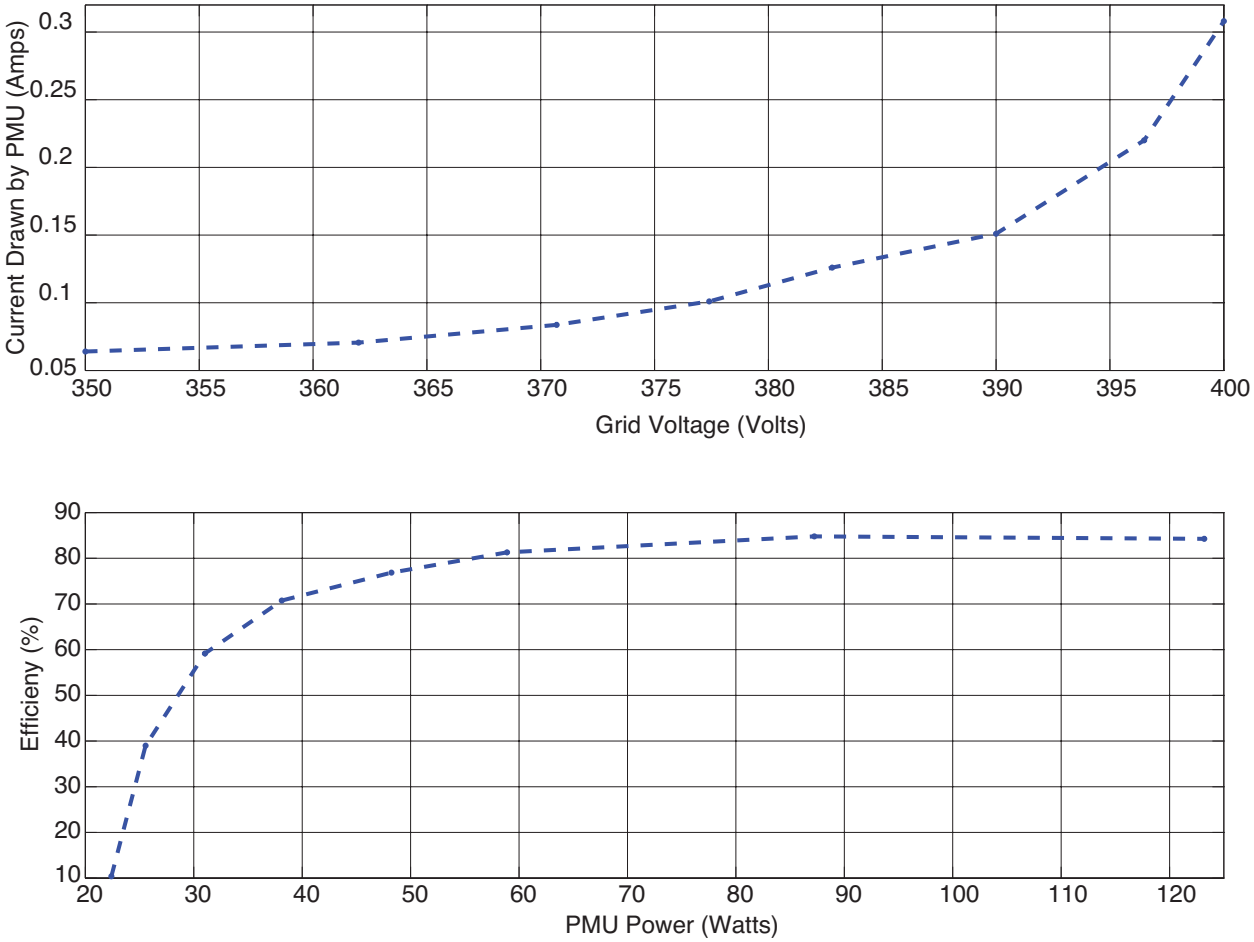

Figure 3.13: Experimental results of large-signal load-line characteristic, and efficiency of PSFB-based PMU.

Table 3.1: Specifications and ratings for prototype microgrid.

Solar PV Array	
Rated Power	$400W$
Rated open circuit voltage	$200V$
Source Converter	
Rated power	$400W$
Rated output voltage	$400V$
Switching frequency	$100kHz$
PMU Converter	
Topology	Phase Shifted Full Bridge
Rated Power	$600W$
Rated output voltage	$12V$
Switching frequency	$100kHz$

3.5 Conclusions

This chapter presented the derivation and performance-evaluation of the first generation hardware for the scalable DC microgrid designed for rural electrification of emerging regions. The general architecture of the DC microgrid was described in detail. This architecture allows for stabilizing grid voltage even in the case where the grid power source is a PV installation without any integrated storage to mitigate source variability. This stabilization is due to the distributed load-line control scheme that is implemented on the DC-DC converters in household PMUs. A phase shifted full bridge (PSFB) converter was selected for the first generation PMUs. The PSFB topology was analytically analyzed to highlight the favorable open-loop properties of the converter. The leakage inductance of the PSFB transformer has a current feedback effect, which provides incremental passivity to the converter's input impedance even under open-loop operation. The load-line control scheme enforces passivity under closed loop operation and allows for direct control of the input impedance of the PMUs. Simulation results were used to highlight: i) the large-signal behavior of the PMUs; and ii) the stable response of microgrid voltages to step changes in input power. Finally, experimental prototypes were used to: i) verify the load-line control scheme under nominal operating conditions; and ii) measure the large-signal response, and efficiency of a PSFB-based PMU.

Chapter 4

Buck Based 2-Stage Topology

This chapter describes the second iteration of the DC microgrid. Modifications were made to both the overall system architecture and the component hardware. The focus of the second-generation prototype system is to reduce the cost and complexity of the microgrid hardware. The second-generation architecture uses commercially available fixed-ratio step down converters to enable a 2-stage conversion process from the 380V distribution bus to 12V at the homes. DC transformers with a 8:1 ratio are integrated into the fanout nodes to generate a 48V bus at a local cluster of households. The household PMUs use a synchronous buck topology to convert from 48V to 12V for household usage and battery charging. Simulation and experimental results are presented that showcase the steady-state behavior, perturbation response, and efficiency of the microgrid. The work presented in this chapter was published in [37].

4.1 Overview of Architecture

An overview of the second generation of DC microgrid architecture is shown in Figure 4.1. The key components of the system are 1) the maximum power point tracking (MPPT) source converter, 2) the fanout nodes, and 3) the household power management units (PMUs).

The DC microgrid distribution voltage is kept in a range between 360 and 400V as in the first-generation of hardware. The grid voltage is converted to 12V at the households for battery-charging and appliance use. The source converter is responsible for: (i) operating the microgrid solar panels at their peak-power point; and (ii) for detecting and isolating faults on the grid. The fanout nodes: (i) aggregate usage from a local cluster of houses (3-5 households within a 15m radius); and (ii) switch and meter the usage of individual households connected to the line. This functionality helps deter theft of power and isolates faults on the grid. Also, each fanout node incorporates a fixed ratio 8:1 DC bus converter. The bus converters, which have a rated efficiency of 95%, are commercially manufactured devices typically used in data center applications [12]. They also provide galvanic isolation

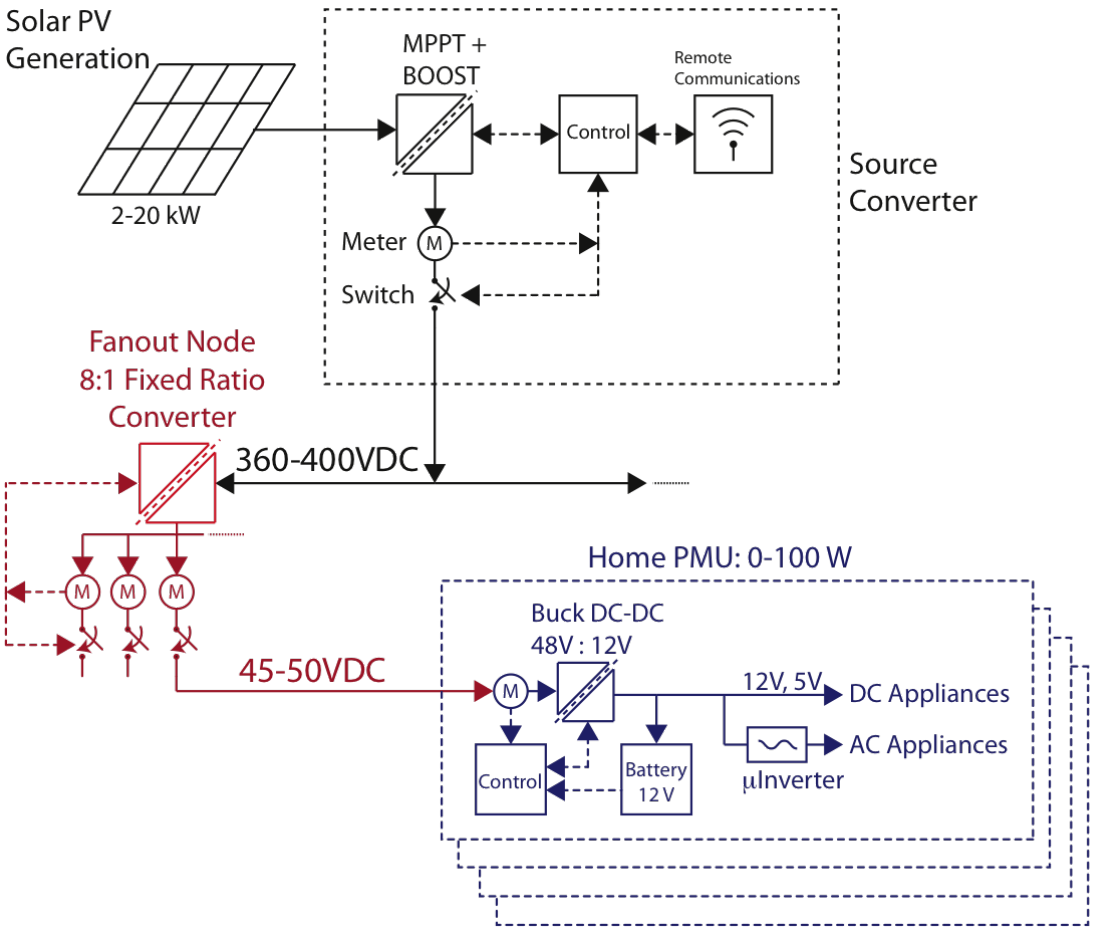

Figure 4.1: An architectural overview of the 3 stage DC microgrid system.

to the connected households which is an important safety consideration. The fanout node provides an intermediate (45-50V) bus to a local cluster of houses. Since the fanout nodes use a fixed-ratio converter, the information implicit in the grid voltage level is preserved and passed on to the households downstream. Finally, each household interfaces to the microgrid through a household power management unit (PMU), which converts the 45-50V fanout bus voltage to 12V through a buck converter for all household appliances, and also integrates battery storage. In addition, the PMUs can digitally communicate information. such as price, charge-state of households, credits, and usage both locally to the end-user and remotely to the system operator.

The droop-voltage power sharing scheme described in Chapter 2 is implemented as shown in Figure 4.2. The core functionality of the second generation of DC microgrid hardware is the same as the first generation hardware described in Chapter 3. The PMU load-line control scheme is now implemented on the 45-50V fanout bus.

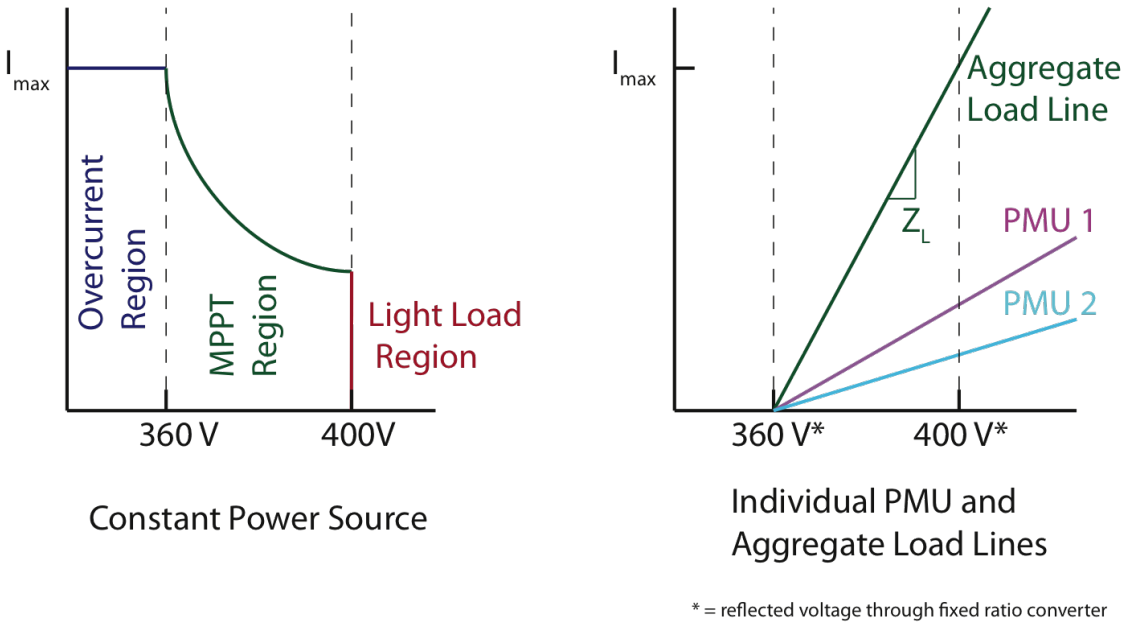

Figure 4.2: Source and load impedances of second generation DC microgrid architecture. The PMU load-lines (right) are reflected through the 8:1 fixed ratio fanout converters. As in the first generation, the PMU load-line slope and offset are controllable variables.

4.2 Motivation for Change in Architecture

The motivation for a change in architecture from a 1-stage to a 2-stage conversion process is primarily driven by the cost of the microgrid components, and a desire to quickly and easily manufacture the various components of the system for testing and deployment. The wide availability of commercial bus converter fixed-ratio modules (BCMs) that convert from 380V to 48V for datacenter applications is a strong factor informing this design change. The price for the 8:1 fixed-ratio BCMs is ~$0.15 per W [12]. Since the secondary side of these BCMs are isolated from the high voltage side, it is also possible to shift to a lower cost non-isolated topologies for the home PMUs. The conversion from the 48V fanout node bus to 12V for household battery-charging, and usage is done using a buck converter topology. The BOM price for a ~200 W buck converters is ~$.07 per W [38]. Although having a limited 48V distribution network incurs additional resistive line losses, these losses can be limited by keeping the distances from the fanout nodes to the connected houses under ~15 meters. The low-load efficiency of the new architecture is also higher as the buck topology does not suffer from the circulating energy losses of a phase shifted full bridge (PSFB) topology; these losses are a large part of the PSFB energy loss budget at low loads. Furthermore, bringing a 48V distribution into the microgrid households is safer than directly bringing the mains 380V bus. Table 4.1 shows the

Table 4.1: LCOE parameters and calculation over a 15 year horizon

System Parameters	
Number of Households	100
Daily Usage	100 W-hrs/day
Radius of Microgrid	1 km
Generation Costs	
Rated Size of Solar Panels	2 kW
Cost of Solar Panels	\$0.70 per W
Cost of Source Converter	\$0.25 per W
Total Cost of Generation	\$1,900
Fanout Node Costs	
No. of Fanout nodes in system	30
Cost of Fanout nodes	\$0.20 per W
Total cost of Fanout nodes	\$2,000
PMU Costs	
Power rating of individual PMU	100 W
Cost of PMUs	\$0.15 per W
Total Cost of PMUs	\$1,500
Battery Costs	
Storage per household	100 W-hrs
LFP Battery Cost	\$0.50 per W-hr
Total Battery Costs over 15 years	\$10,000
Wiring Costs	
Total T&D wiring costs	\$4,000
Total System Cost	\$19,400
LCOE of elec. delivered over 15 years	\$0.35 per kW-hr

levelized cost of electricity (LCOE) calculation for the second-generation microgrid with the 2-stage topology.

4.3 Prototype Implementation

In order to experimentally validate the proposed DC microgrid architecture, a scaled-down 400W hardware prototype setup, shown in Figure 4.3c, was constructed and installed at the University of California, Berkeley. The full specifications and ratings for the prototype setup are presented in Table 4.2. The converter designs and enclosures are shown in Figure 4.3. The source converter (Figure 4.3a) consists of a 2-phase interleaved boost converter, fuse protection, and connectors for PV input and bus output. The fanout node is implemented using a commercially available 8:1 fixed-ratio 300W BCM which converts from 360-400V to 45-50V. The household PMU (Figure 4.3b) consists of a 100W syn-

chronous buck converter, fuse protection, 100 W-hrs of battery storage, and connectors for 45-50V bus input and 12V DC output. The load-line control is implemented using proportional feedback of voltage at the input terminal of the converter as shown in Figure 4.4. The output from the outer voltage loop forms the peak current reference to the inner current loop. The gain of the outer loop determines slope of the load-line (input impedance) of the converter. Achieving load-line regulation through such a proportional feedback scheme has been used for output regulation of dc-dc converters [39, 40]. We use the same techniques to achieve load-line regulation on the input of the PMU buck converters. The derivation of the relationship between the proportional feedback gain and load-line slope is presented in the subsection below.

Table 4.2: Specifications and ratings for prototype microgrid

Solar PV array	
Rated power	400 W
Rated open circuit voltage	200 V
Source Converter	
Topology	2-phase boost converter
Rated power	400 W
Rated output voltage	400 V
Switching frequency	100 kHz
Household PMU	
Topology	Synchronous Buck
Rated power	100 W
Rated output voltage	12 V
Switching frequency	250 kHz

4.3.1 Derivation of Relationship Between Load-line Control Scheme and Feedback Gain

The dynamics of the buck converter with an inner peak current control loop can be extracted from the inductor waveforms (Figure 4.5). For the following set of equations we assume that the converter is operating in continuous conduction mode and the voltage ripple on the capacitors is small over a switching period.

Over a switching period the relationship between the current reference command, I_{cmd}, and the average inductor current, I_L is given by:

$$I_{cmd} - I_{ramp} \cdot D \cdot T = I_L + \frac{\Delta I_L}{2} \tag{4.1}$$

where I_{cmd} is the peak current reference value, I_{ramp} is the slope compensation magnitude, D is the nominal duty cycle of S_1 as shown in Figure 4.4, T is the switching cycle period,

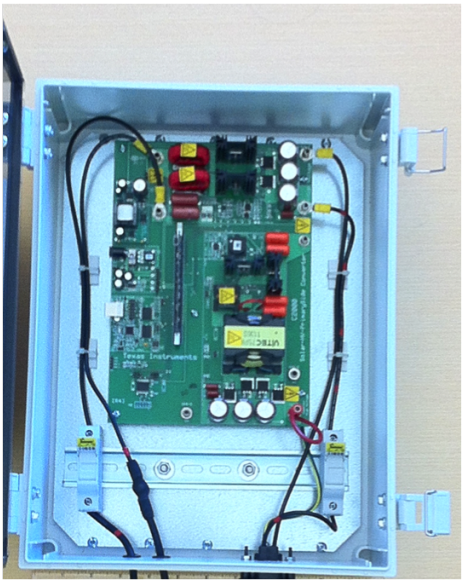

(a) 400 W 2-phase boost source converter.

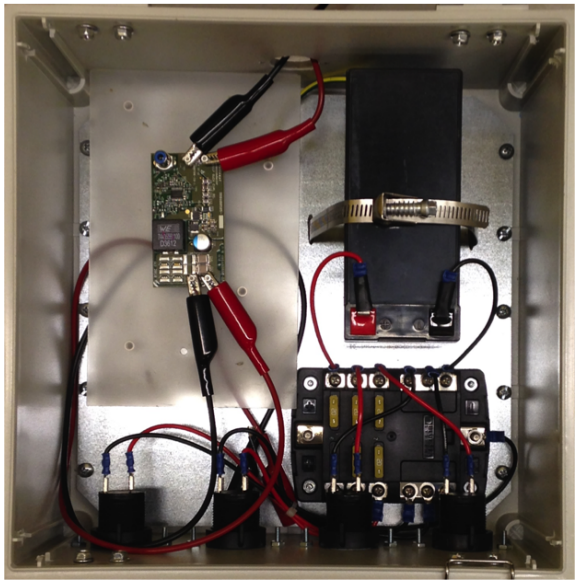

(b) 100W buck converter with a 12V 8A-hr lead acid battery for storage.

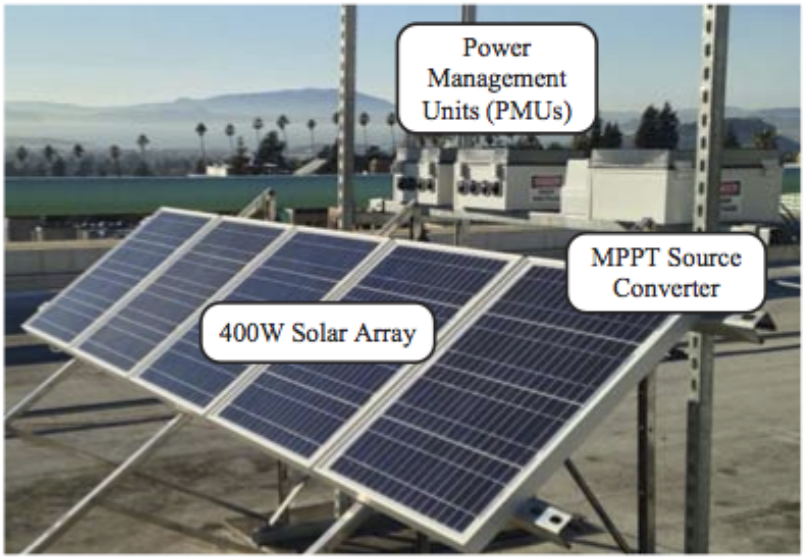

(c) Rooftop setup with 400W solar PV installation. The source converter regulates the solar panels to operate at their peak power point. 2 PMUs are connected to the output of the source converter and regulate the distribution bus voltage.

Figure 4.3: Pictures of 2nd generation prototype hardware.

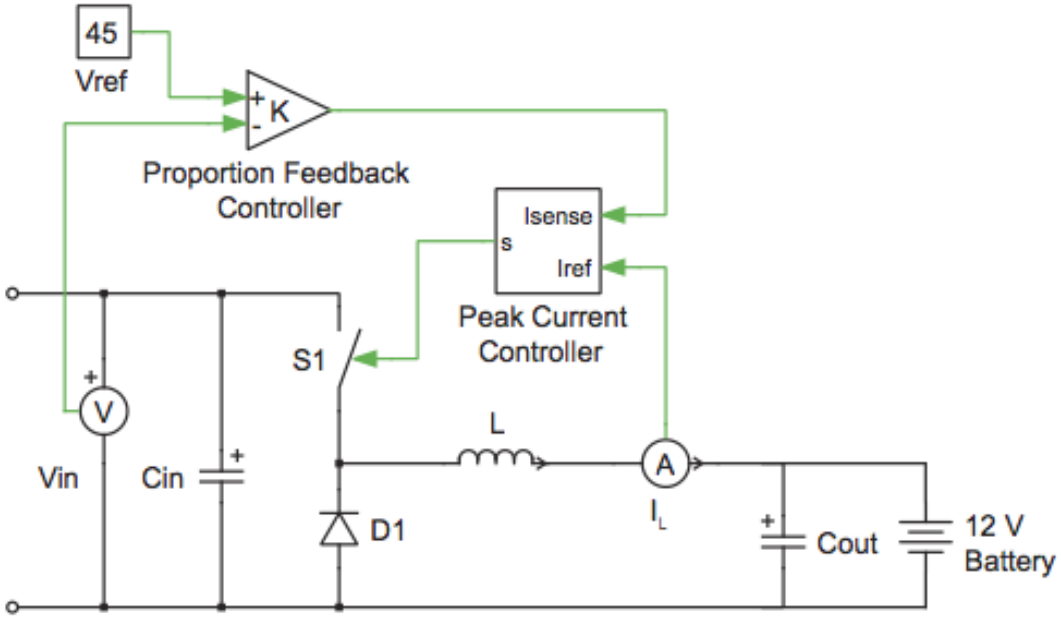

Figure 4.4: PMU load-line implementation. The gain of the outer voltage loop sets the load-line slope.

I_L is the average current through the output filter inductor, and ΔI_L is the magnitude of the current ripple in the output inductor. The current ripple on the inductor, ΔI_L is:

$$\Delta I_L = \frac{V_{in} - V_{out}}{L} \cdot D \cdot T \tag{4.2}$$

Therefore, we have a direct relationship between I_{cmd} and I_L:

$$I_{cmd} = I_L - \frac{\Delta I_L}{2} - I_{ramp} \tag{4.3}$$

The relationship between the average input current, I_{in}, and I_L in CCM is: $I_{in} = D \cdot I_L$; where the duty cycle: $D = V_{out}/V_{in}$. The desired relationship between I_{in} and V_{in} for a load-line profile is given by:

$$I_{in} = g_{des} \cdot (V_{in} - V_{ref}) \tag{4.4}$$

Therefore I_{cmd} has to be scaled by V_{in}/V_{out} to have the desired load-line slope, g_{des}:

$$I_{cmd} = g_{des} \cdot (V_{in} - V_{ref}) \cdot \frac{V_{in}}{V_{out}} \tag{4.5}$$

Using a nominal value of $V_{in}/V_{out} = 48/12$ in Eq. 4.5 is a simplification that allows for a single op-amp circuit to generate I_{cmd}. As shown in Chapter 3.2.2, , the simplification

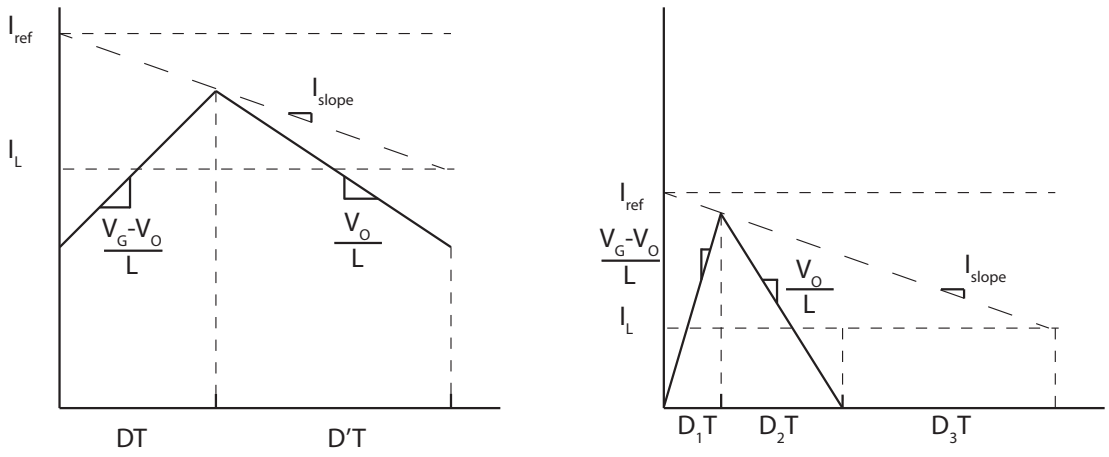

Figure 4.5: Buck Converter Inductor Waveforms for CCM and DCM

is used since the nominal value of V_{in}/V_{out} deviates from the actual value by less than 5% over the entire operating range of V_{in}. As shown in Eq. 4.3, ΔI_L and I_{ramp} introduce an offset between I_{cmd} and I_L. This offset is addressed by adjusting V_{ref} in Eq. 4.5 appropriately.

In discontinuous conduction mode, there is a deviation from the ideal load-line behavior shown in Eq. 4.4 when I_{cmd} is generated with a single op-amp circuit as described in the prior paragraph. This is due to the effect that discontinuous conduction mode has on the relationship between I_{in} and I_l. Using a similar analysis as above,

$$I_{cmd} - I_{ramp} \cdot D_1 \cdot T = \frac{V_{in} - V_{out}}{L} \cdot D_1 \cdot T \tag{4.6}$$

$$\frac{V_{in} - V_{out}}{L} \cdot D_1 \cdot T = \frac{V_{out}}{L} \cdot D_2 \cdot T \tag{4.7}$$

$$I_L = \frac{(V_{in} - V_{out})\,(D_1 + D_2) \cdot D_1 \cdot T}{2 \cdot L} \tag{4.8}$$

where D_1 is the nominal duty cycle and $D_2 \cdot T$ is the time that it takes for the inductor current to drop to 0.

When I_{cmd} is defined by Eq. 4.5, the relationship between I_{in} and V_{in} is given by:

$$I_{in} = \left(\frac{V_{in}}{V_{out}} \cdot g_{des} \cdot (V_{in} - V_{ref})\right)^2 \cdot \frac{(V_{in} - V_{out})}{(L \cdot I_{ramp} + (V_{in} - V_{out}))^2} \tag{4.9}$$

The behavior of a buck converter including both DCM and CCM is shown in Figure 4.6. The dashed line indicates a desired load-line behavior. By appropriately choosing the gain and offset parameters, it is possible to achieve a close approximation of the desired behavior across the entire operating range of V_{in}.

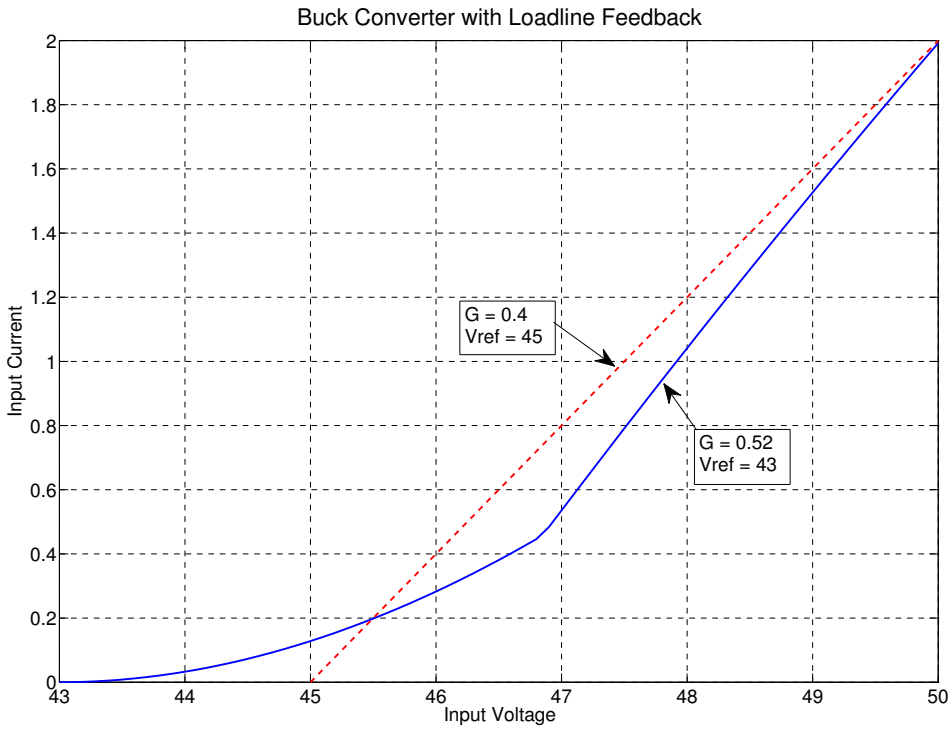

Figure 4.6: Behavior of Buck Converter with CCM and DCM considered. The dashed line shows the desired load-line behavior and the solid line shows the necessary gain and offset to achieve an approximation of the ideal behavior.

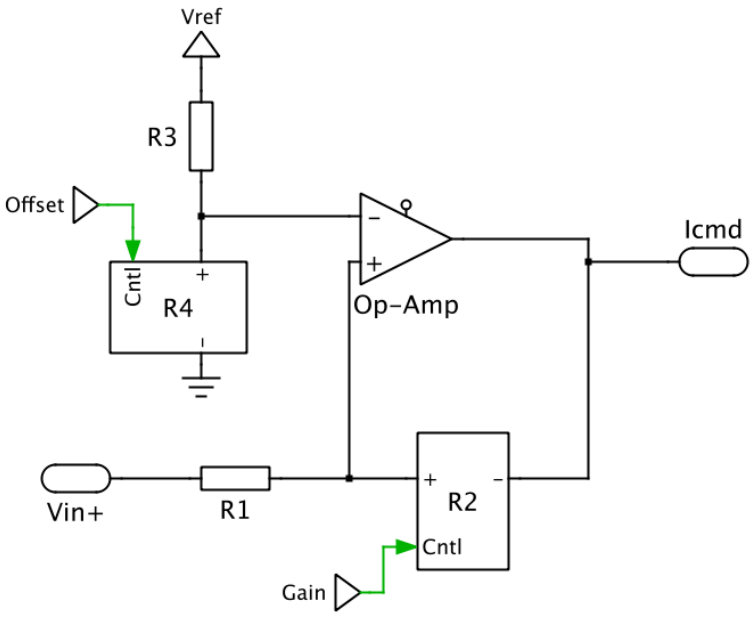

Figure 4.7: PMU Feedback implementation with op-amp and controllable resistors.

4.3.2 Buck Converter Load-line Feedback Loop Implementation

The Buck converters used to generate the results presented in this chapter utilize a reference design for the Texas Instruments LM5117 current-mode buck-controller IC. The peak current reference command, I_{ref}, is generated using an op-amp circuit with two independent controllable resistors shown in Figure 4.7. R_2 is responsible for control of the gain parameter g_{des} and R_4 controls the offset of the load-line, V_{ref}. Figure 4.8 shows the closed-loop small signal input impedance of a buck converter with load-line feedback scheme. The input impedance exhibits a single pole response, which is favorable for grid voltage stabilization.

4.4 Experimental Results

In this section, experimental results that demonstrate the operation of the second-generation DC microgrid prototype setup under various operating conditions are presented. The steady state behavior of the PMU converters, and the perturbation response of microgrid voltages are shown as the power from the source is varied. The startup and shutdown behaviors of the various components of the microgrid are also shown.

4.4.1 Experimental Test Setup

A solar panel connected to a MPPT converter behaves as a constant-power-source. In order to create a controllable constant-power-source for the experiments in this section, a

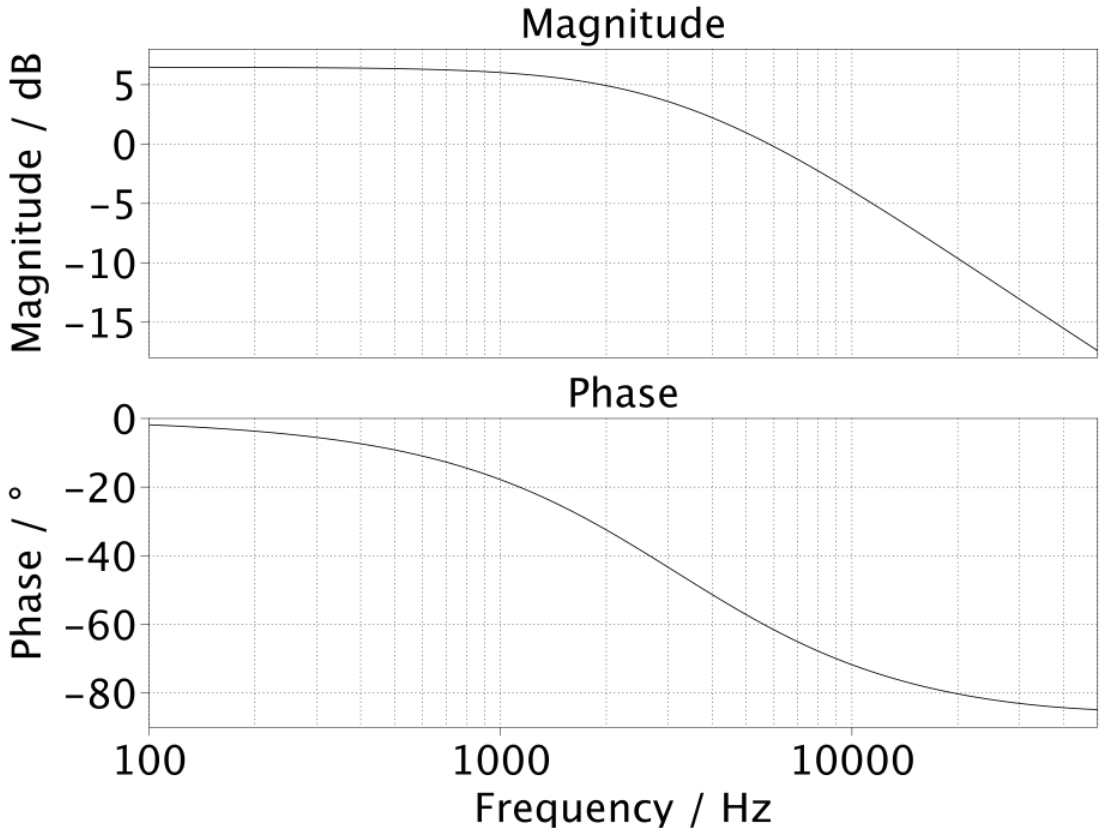

Figure 4.8: Small signal closed-loop input impedance of boost converter with load-line feedback. This plot is generated from a PLECS simulation of the converter and exhibits a single pole response with a corner frequency $f_c = G/C_{in} \cdot 2 \cdot \pi$ where $G = 0.5$ is the input gain corresponding to the commanded load-line slope and $C_{in} = 30\mu F$ is the input capacitance.

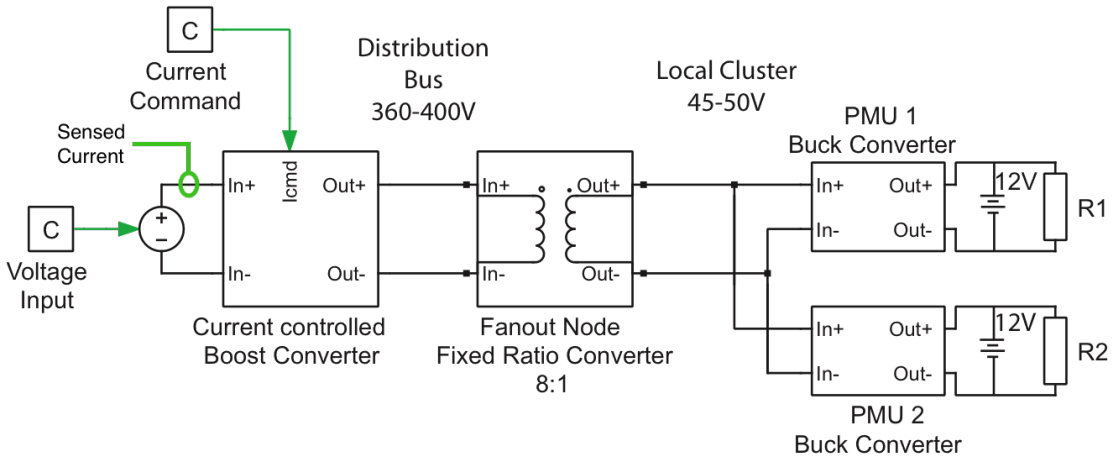

Figure 4.9: Schematic of experimental setup. The input current to the boost converter is sensed and regulated to the current command.

boost converter operating in input-current-control mode was used, i.e., where the input current from the voltage source is regulated. A schematic of the setup is shown in Figure 4.9. The input power to the 380V bus can be varied by either by changing the input voltage to the current-controlled boost or by changing the current command. The current command was used to cause step changes in grid power.

4.4.2 Steady State Behavior

Figure 4.10 shows the steady-state response of the PMU input current as a function of the grid voltage. The efficiencies of the Fanout and PMU converters used in the experiment setup are shown in Figure 4.11. Both simulation and experimental results show the same relationship between current drawn by the PMU and input voltage. As shown, the current drawn by each PMU increases as the grid voltage increases, thus exhibiting a positive impedance characteristic. The slope of this load-line is fully programmable and set by the feedback gain of input voltage. The gain on the controller is set to achieve an input impedance of Z = 2Ω. Once the PMU converter is operating in continuous conduction mode, both the simulation and experiment show that the steady state input impedance is 2Ω. When the converter is in discontinuous conduction mode , the input-impedance is higher than in continuous conduction mode. However, this deviation does not have any significant impact on system behavior as will be shown by the perturbation response.

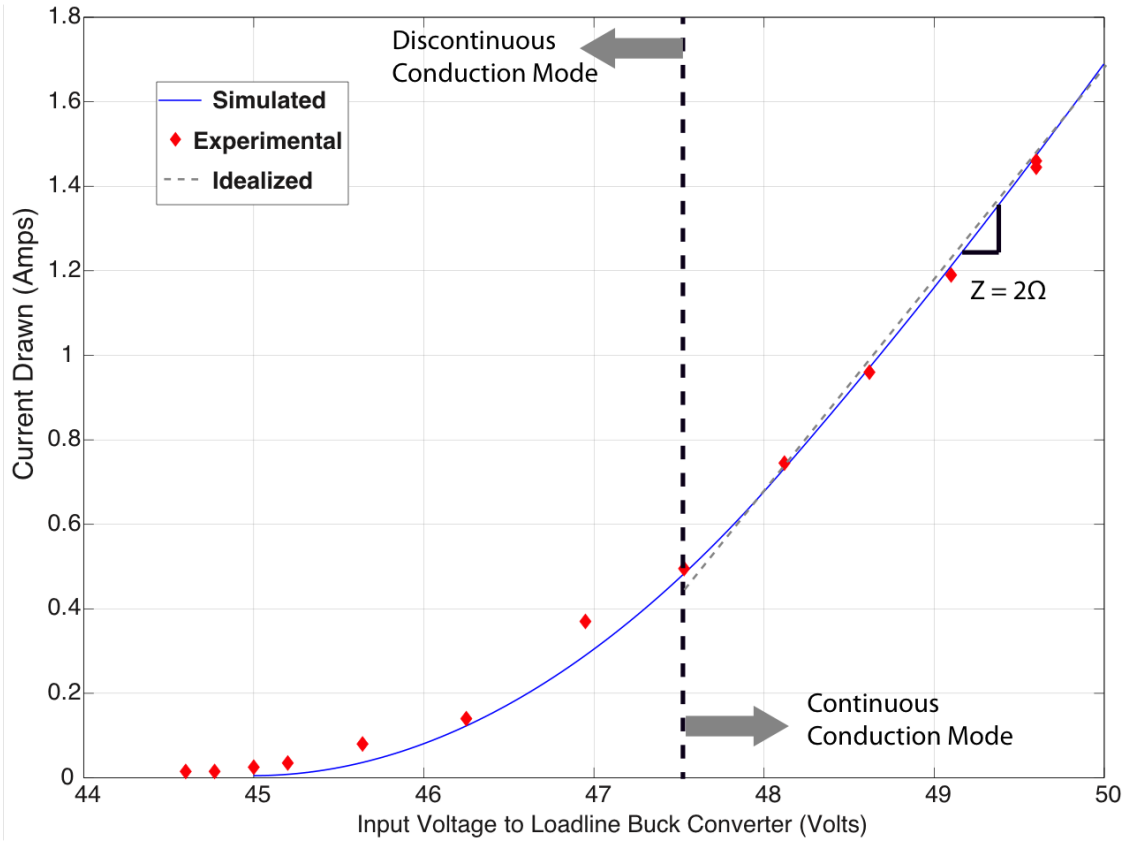

Figure 4.10: Simulation and experimental results showing the change in input current of a PMU buck converter implementing a load-line profile in response to grid voltage on the fanout node bus.

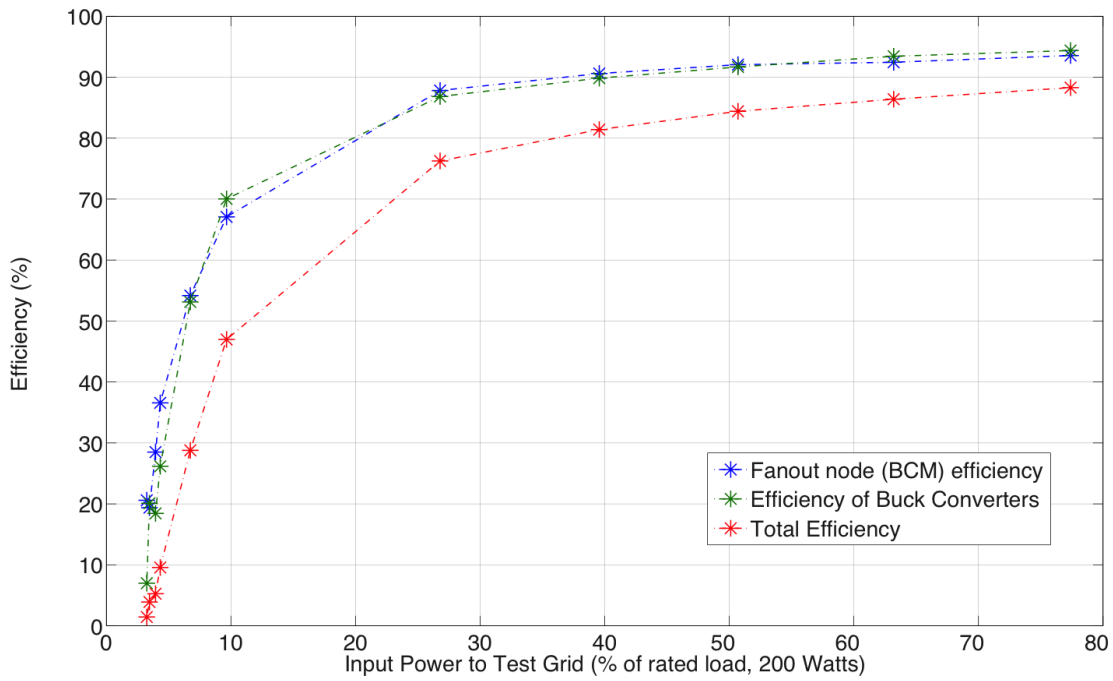

Figure 4.11: Efficiency of the fanout bus converter and the PMU buck converters as a function of input power for the configuration shown in Figure 4.9.

4.4.3 Perturbation Response

Figure 4.12 shows the perturbation response of the grid voltage, fanout node voltage, and the input current to the 2 PMUs (setup shown in Figure 4.9) in response to a step change in the microgrid power. Initially, the input power to the grid is 5W. At this level, the fanout node is powered on, but the fanout bus voltage is below 45V so the PMUs are not drawing any current from the grid; the power is dissipated in the fanout node bus converter. At t = 0.19 secs, the available grid power is instantaneously increased from 5W to 70W by commanding a step change in input current drawn by the boost converter in the experimental setup. Immediately, the grid voltage starts to rise, but remains within the 360 to 400V range. This stabilization is due to the response of the PMUs, which increase their current draw in response to the increase in grid voltage.

4.4.4 Startup and Shutdown Behavior

Figure 4.13a shows the startup behavior of the microgrid. After the power source is turned on, the voltage on the high voltage bus of the grid starts to rise. The high voltage bus rises to 400V before the fanout node starts to operate. Upon turn on of the fanout node bus converter, t = 1 sec, the voltage on the fanout node bus immediately rises to 50V. The initial spike in PMU current is due to the input capacitors charging from 0

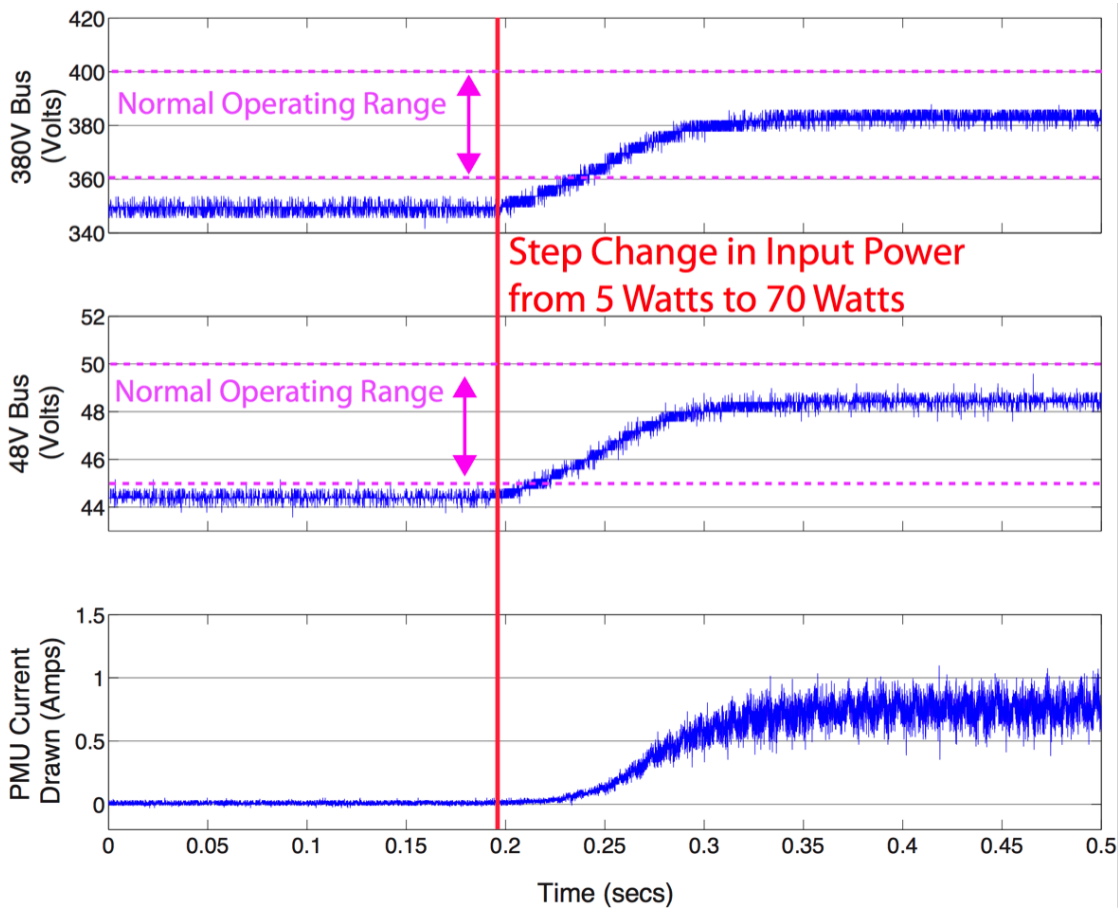

Figure 4.12: Transient behavior of bus voltages and PMU current draw in response to a step increase in grid power (5W to 70W) at $t = .19$ secs.

to 50V. The PMUs connected to the fanout node start to draw current from the fanout bus according to their load-line. This subsequently causes the voltage on both busses to droop and settle at an operating-point determined by the intersection of available power and the aggregate PMU load-line.

Figure 4.13b shows the shutdown behavior of the microgrid. As the bus voltages start to drop, the PMUs respond by drawing less current from the grid. Once the fanout bus voltage drops below 45V, the PMUs do not draw any more current. As the grid voltage drops below 300V the bus converter in the fanout nodes also shuts down and the grid voltage continues to fall. In both startup and shutdown scenarios, the household load on the low-voltage side of the PMU is decoupled due to the battery.

4.5 Conclusions

This chapter presented the design and implementation of the second-generation of scalable DC microgrid architecture for rural electrification. A 2-stage architecture that used commercially available 8:1 BCMs in addition to a 48-12V boost converters for the PMUs was fully examined. The cost analysis of the system showed that over a 15 year time span, the LCOE can be below $0.40 per kWh. This provides a compelling case for the economic viability of the architecture. The second-generation DC microgrid hardware also allowed for increased efficiency at low loads in comparison to the phase-shifted full bridge (PSFB) based architecture described in Chapter 3. Finally, the operation and stability of the DC microgrid distributed voltage control scheme were experimentally demonstrated over a wide range of operating conditions.

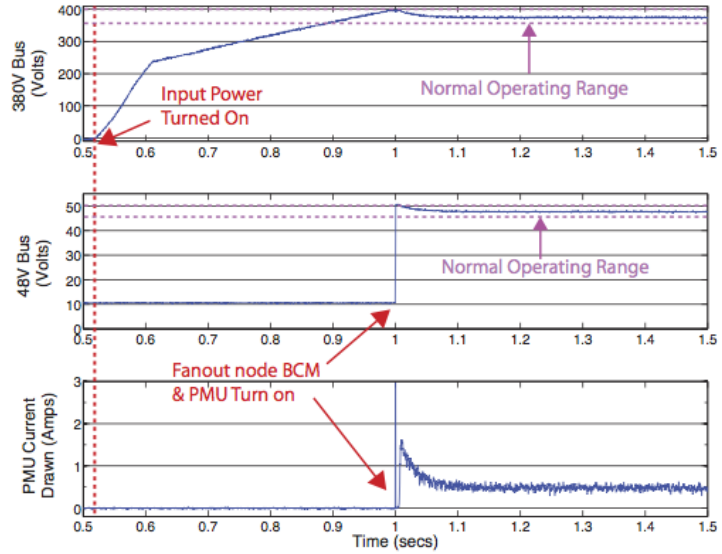

(a) Startup behavior of experimental microgrid setup after input voltage source is turned on at time $t = .52$ secs. The available power from the source upon startup is 55 W

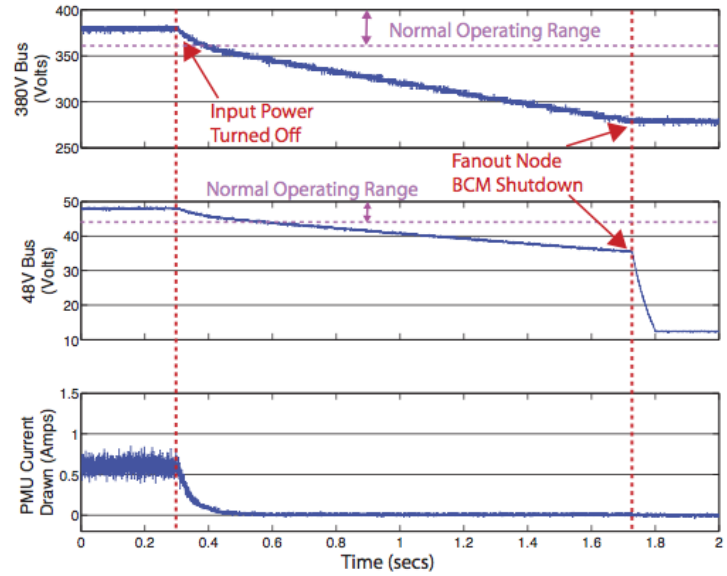

(b) Shutdown behavior of experimental microgrid setup after input voltage source is turned off at time $t = .3$ secs.

Figure 4.13: Startup and shutdown behavior of prototype DC microgrid system with input power set 55W.

Chapter 5

Protection and Fault Mitigation for the DC Microgrid

One of the major concerns with electrical transmission and distributed systems is the mitigation and diagnosis of faults. This section covers the classification of various faults that can be expected to occur in a microgrid distribution system. Mitigation strategies for the faults are also discussed.

Existing grounding schemes in AC distribution systems and in DC data centers are discussed. Present best practices are discussed and recommendations for this dissertation's DC microgrid are given based on safety, and economic motivations.

Lastly, a set of simulations and experiments that showcase the response to various fault conditions are presented to verify the faulted behavior of the DC microgrid.

5.1 Grounding Scheme

5.1.1 AC Distribution Grounding Schemes

For a distribution system, one of the most important considerations in fault mitigation is having an effective grounding scheme. AC distribution schemes have relied on 3-wire transmission for single-phase power and 4-wire transmission for 3-phase power for maximum safety. Typically the neutral in a singe-phase distribution is connected to earth-ground through a low-impedance connection at the low-voltage (120V) distribution transformer. Figure 5.1 shows the most common type of grounding scheme in the AC distribution systems. This type of scheme is called a TN scheme; where T stands for "Terra" and and N indicates a direct connection from earth to neutral at the origin of installation. In a TN grounding scheme, the neutral (N) line is connected directly to earth at the distribution transformer. The protective earth (PE) line is distributed along with the "hot" and N lines to the consumer; The PE line is not meant to be a current-carrying line during normal operation. The function of PE is to provide a fixed ground reference at every plug point. Load currents can cause the N point of an outlet to raise above the

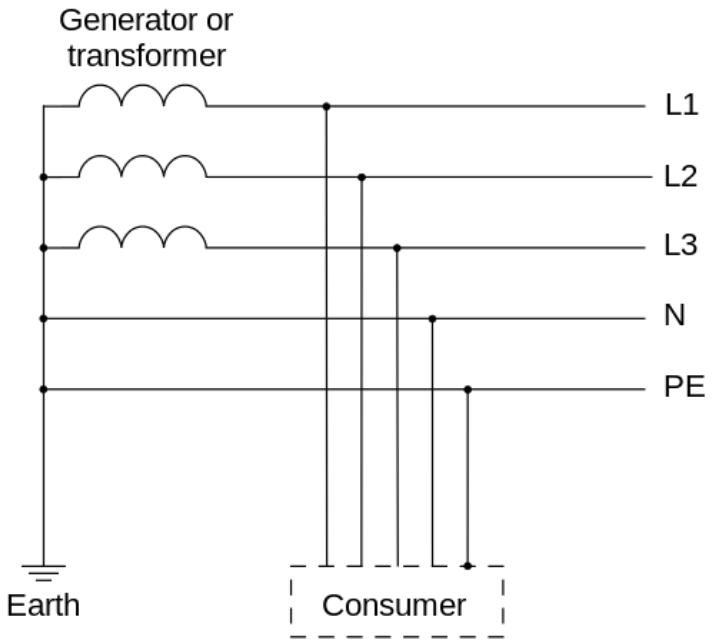

Figure 5.1: TN-S grounding scheme for AC distribution systems [9].

earth potential due to the resistive drop across the N conductor. PE also provides a low impedance path for dissipating surge currents that might occur in the case of events such as lightning strikes. In the US, a hybrid scheme where the connection between PE and N is done both at the transformer and outside the service entrance to the household is typically implemented. This hybrid ground scheme can be described as a multiple earthed neutral (MEN) scheme since there can be multiple points of connection to PE, i.e. outside each household on the same distribution network.

Another earthing scheme that is widely used is the TT (Terra-Terra) grounding scheme. This is shown in Figure 5.2. In the TT earthing scheme, the N line is grounded at the transformer, but the PE line is not distributed to the consumer. Instead a separate ground connection is made near the consumer for a local PE line. If it is practically possible to make a low-impedance grounding connection at the service entrance, then TT schemes are more economical since they require one less conductor in the distribution network. The fault impedance of a TT scheme in the case of line-to-ground faults is higher due to the lack of a dedicated PE line from the source generator/transformer. With a ground-fault detector (GFCI) or a residual current detector device (RCD) [41], it is possible to detect ground faults as effectively as the case where there is dedicated PE conductor. The TT scheme is used often in data centers and telecommunications applications since there is significantly less coupling of high-frequency noise into the N and PE lines.

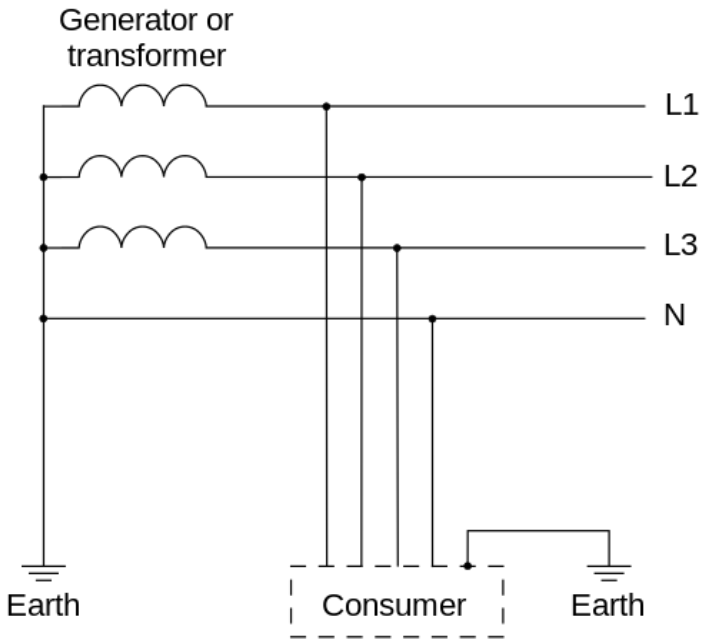

Figure 5.2: TT grounding scheme for AC distribution systems [9].

5.1.2 -48V DC Telecommunication Distribution Grounding Scheme

Although most commercial and residential distribution schemes have usually been AC, there are some DC distribution schemes that can be used to inform the earthing decisions made for the DC microgrid described in this dissertation. The most widely utilized DC distribution system is the telecommunications network; A -48V transmission scheme for powering telecom equipment [10]. The -48VDC scheme is a three-wire distribution scheme with a power conductor, a power return conductor (called BR for battery return), and a PE conductor. The BR conductor and and the PE conductor are connected to earth at a single point. As in the AC earthing schemes, the PE conductor is not a current carrying conductor. Figure 5.3 shows the typical grounding scheme for 48V DC distribution in a data center setting. Neither the BR conductor nor the -48V line is connected to the chassis of the load equipment. The PE line is used to provide the low impedance path to earth for the frame of the telecom equipment.

5.1.2.1 Note on Corrosion and "-"48VDC Scheme

The polarity of the 48V DC telecom transmission scheme is driven by concerns over corrosion of buried conductors. In most 48V telecom systems there is a physical battery providing backup power for the local equipment. If there is an electrical leakage pathway from the copper wires connected to the battery through surrounding wet soil, then the positive copper wire loses metal ions to the relatively negative soil through electrolysis.

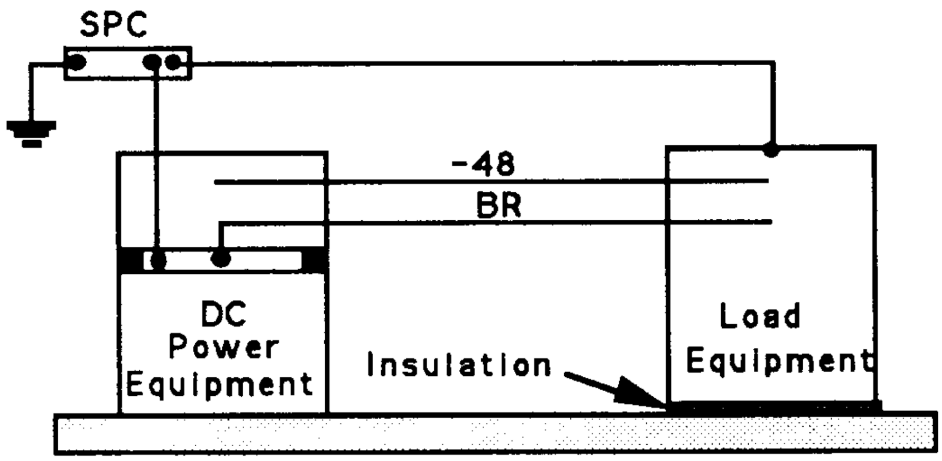

Figure 5.3: Example of -48V DC distribution scheme commonly used in a telecom setting. SPC stands for single point connection to earth. The protective earth line is distributed from the point of connection of the DC power equipment and is the only grounding connection for load equipment [10].

This process causes the positive wire to de-electroplate and corrode. The electrolysis process can be understood by considering an electroplating example, where two metal plates are connected to a battery and placed in a conductive liquid. Electric current flows through the liquid from the positive plate to the negative plate. Positive metal ions are lost by the positive plate due to oxidation. The positive metal ions recombine with electrons on the negative plate through reduction. The result of this reaction is that a metal coating is transferred from the positive plate to the negative plate. This is the same type of reaction that can occur between the positive conductor in a DC system and surrounding wet soil. Electrolytic corrosion is a major concern especially with thin conductors or in cases where the conductor insulation is poor. By connecting the +48V terminal of the battery to earth, the corrosion of the positive wires is mitigated. This is because, the surrounding soil is no longer more negative than the copper wires [42]. The concerns of electrolytic corrosion are greatly reduced in overhead transmission schemes and when larger conductors are used.

5.1.3 Existing 380V DC Distribution Grounding Schemes

Even though higher DC voltages have not been used as extensively as 48V in telecom applications, there are a number of companies that are pushing the 380VDC standard and piloting projects to showcase the advantages of the high voltage DC standard. Some of the main companies trying to encourage adoption of the 380V standard are: Emerson Network Power, Vicor Power, Nextek Power Systems and the EMerge Alliance. The EMerge alliance is an industry association that is establishing a 380V standard geared

at telecom applications [26]. Although there is not an established grounding-scheme standard for a 380VDC distribution, a common feature of all the pilot projects has been using midpoint grounding for +/- 190V transmission [43, 44, 11, 45]. Two examples of midpoint grounding schemes are shown in Figure 5.4. The capacity/battery midpoint is not favored due to the much safer nature of high-resistance midpoint grounding. High-resistance midpoint grounding is widely used in 110-220VDC industrial, utility and railway settings [11]. High-resistance midpoint grounding has the following safety features:

1. High fault-impedance for pole-to-earth faults. Since a high value resistance is present between the hot lines and ground, the fault current can be made to be very low, effectively removing human risk for a pole-to-earth fault. If the first fault is not cleared, then the next fault will face a low impedance, so high-impedance midpoint grounding provides a single-failure resiliency.

2. Removes risk of arcs at short circuit to ground scenarios. The high impedance in the grounding scheme remove risk of arc flashes from the ground-faulted conductor.

While high-resistance grounding removes the risk of the initial pole-to-earth fault, the concerns of pole-to-pole faults and multiple pole-to-earth faults still need to be mitigated. Fuses and circuit breakers are used to reduce the risk of pole-to-pole faults. In a high-resistance grounding scheme, the power distribution network is not affected by a single pole-to-earth fault. However, if the first fault is not cleared before there is a subsequent ground-fault with the remaining pole, then the risk to humans for the second fault is very high. The use of GFCI devices is necessary to detect the high-impedance ground faults quickly before a second potentially catastrophic fault occurs.

5.1.4 Grounding Schemes for Lower DC Voltages (12-24V)

There are an abundance of devices that run on lower DC voltage levels—from 5V up to 48V. The main examples for 12V distribution systems are automotive and marine, battery-based systems. There is a wide set of consumer appliances that are designed to run on 12V batteries. All 12V systems are 2-wire distribution schemes with the negative terminal of the battery/supply connected to ground. Typical 2-wire connectors for 12V, shown in Figure 5.5, are either barrel connectors—common on DC adapters, or car and marine type connectors.

There is also an emerging standard for a 24V DC overlay on top of existing AC wiring in buildings. Nextek power has demonstrated such an overlay scheme by using the N and PE as a 2-wire pair for DC power distribution [45]. An isolation-transformer is used at the building entrance to isolate the building wiring from the input grid-supply. A 24V DC source is inserted between N and PE lines so the N carries the +24V and the PE acts as the return. With this approach, major rewiring of buildings is not required to provide a low-voltage, DC distribution system to the building outlets. It is important to note that the 24V scheme is a 2-wire distribution scheme with the PE line acting as both the

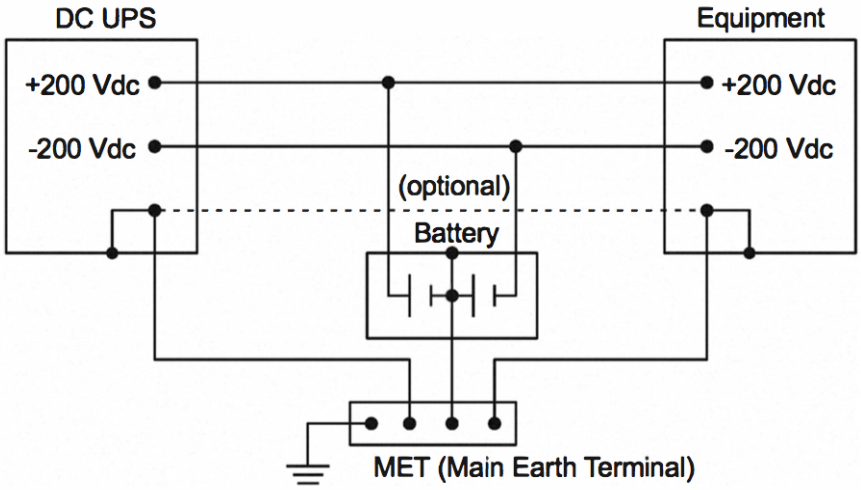

(a) Capacitive/Battery direct midpoint grounding scheme

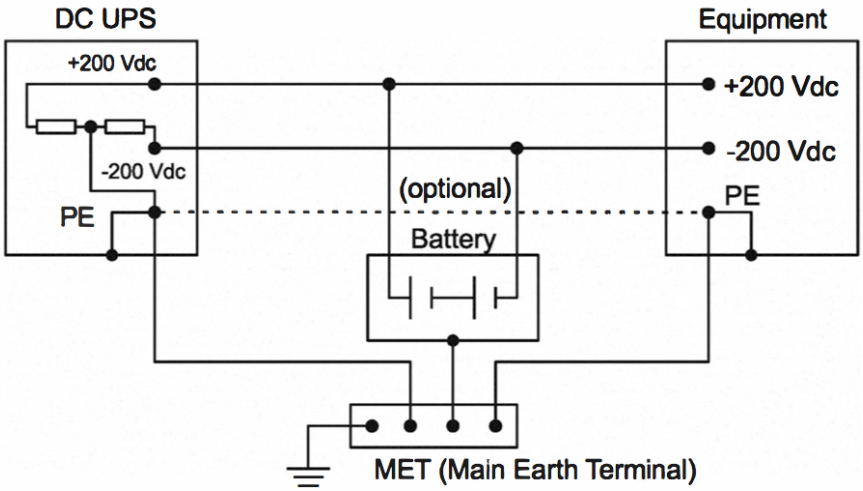

(b) High-resistance midpoint grounding scheme

Figure 5.4: Midpoint grounding schemes [11].

Figure 5.5: Typical connector types for 12V DC appliances. Barrel type connecter common on DC adapter is shown on the left. Car-type connector used in automobile and marine applications is shown on the right.

return and the earthing line. Since 24V is too low to pose a health hazard, a dedicated earthing wire is not considered essential.

5.1.5 Proposed Grounding Scheme for Rural DC microgrid

The DC microgrid presented in this dissertation has multiple voltage levels in the transmission scheme and as such the grounding scheme is different for each of the voltage levels. There are 2 versions of microgrid architectures:

1. Single-stage topology with 380V distribution to each home. A PSFB converter integrated in the home PMU converts from 380V-to-12V for home use.

2. Two-stage topology using intermediate bus converters to generate a 48V bus at the fanout nodes of the microgrid. A buck converter integrated in the home PMU converts from 48V-to-12V for home use.

The grounding schemes presented in the sections below address both the prototype system architectures.

Safety, cost, and reliability are the driving metrics for the design of a protective grounding scheme. The paramount concern is to minimize health risks. However, as there are a variety of equally safe grounding schemes, the wiring-cost of the scheme is also an important factor.

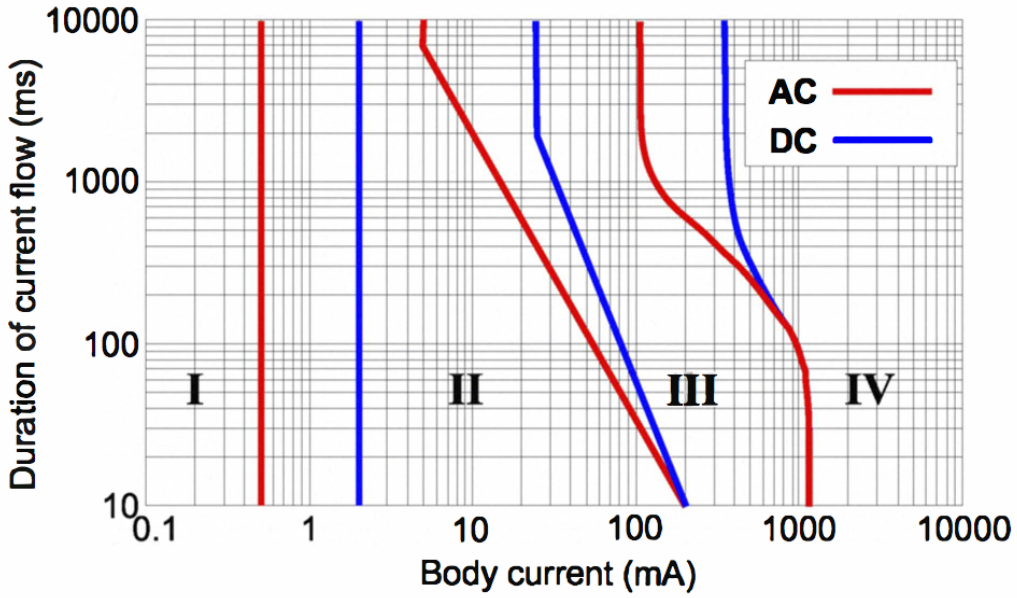

Figure 5.6: DC and AC currents organized by danger. The levels of shocks are bounded by the DC current level lines. DC shocks are slightly less dangerous than equivalent AC shocks. Level IV shocks are considered critical, with possibility of ventricular fibrillation [11].

5.1.5.1 380V bus: source-to-fanout node

On the 380V bus, a high-resistance midpoint grounding scheme is the safest option. The advantages have been described in Section 5.1.3 in detail. There are two main factors that greatly enhance the safety of a high-resistance midpoint grounded distribution system against pole-to-earth faults:

1. The line-to-earth potential of the distribution lines is reduced from 380V to +/- 190V from grounding the midpoint of the 380V bus.

2. Ground-fault currents are limited by the impedance of the high-resistance grounding connection.

Figure 5.6 shows the effect of different levels of shock currents. Any currents in levels II and below are safe and not perceptible. So by using a pair of $50k\Omega$ resistor between the grounding wire and the two 380V lines, the fault currents are kept below 4mA.

With high-resistance grounding, it is necessary to have RCD/GFCI functionality on the resistive divider to detect ground faults; high-impedance faults are unlikely to trip any circuit breakers. In our microgrid architecture, the RCD functionality can be integrated into the source converter—thereby removing the need for an external fault-detection device. Typically, RCDs work by detecting a difference in currents between the power-line

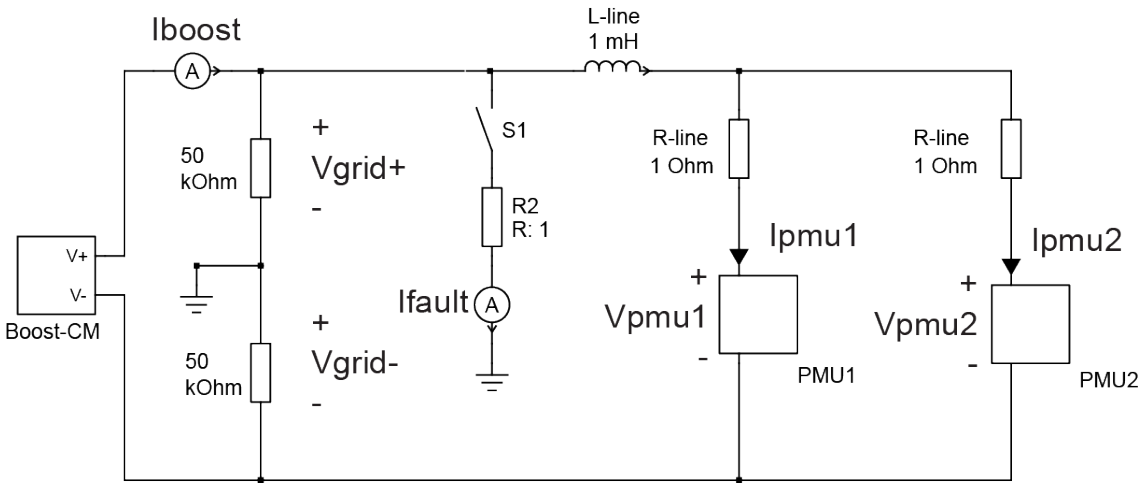

Figure 5.7: Setup for high-resistance midpoint grounding simulation. Two $50k\Omega$ resistors are used for the midpoint grounding. A 1Ω fault is simulated on the +190V line.

and the return-line; any imbalance between the two currents is considered a fault. Figure 5.7 shows the setup that was used for simulating the effect of a pole-to-earth fault on the +/- 190VDC bus. Figure 5.8 shows the effect of a ground-fault on the line voltages and currents of a high-resistance midpoint grounded distribution network. A ground-fault can be detected by monitoring the voltages on the +190V and -190V lines. In the case of a ground-fault, one of the lines will drop to earth potential and the other will rise to full-scale (380V).

The choice between a TN-S type scheme vs a TT type scheme comes down to whether it is cheaper to run an extra PE conductor from the source converter or whether it is cheaper to install a low-impedance connection to earth at the fanout node. Since the cost of wiring is a significant part of the capital costs as shown in Table 4.1, a TT-type scheme with earth connections at the fanout nodes has the potential to be more cost-effective. This will have to be verified through field trials. Figure 5.9 shows a schematic of a 2-wire +/- 190V scheme from the source converter to the fanout nodes of the microgrid system. The fanout nodes serve as grounding points to a local cluster of microgrid households. The chassis of the fanout node boxes are connected to ground through a local low impedance earthing connection.

5.1.5.2 Fanout node to home 380V single stage conversion

In the case where there is a single-stage 380-to-12V PSFB converter at each home, the connection from the fanout node to the home is a 3-wire scheme with +190V, -190V and PE. This is in compliance with the established standards for TT-schemes. The PE line is connected to the negative terminal of the battery on the secondary side of the PSFB converter. The 12V power is a 2-wire scheme. This is in line with existing DC appliances where the negative terminal is often connected with chassis of the appliance.

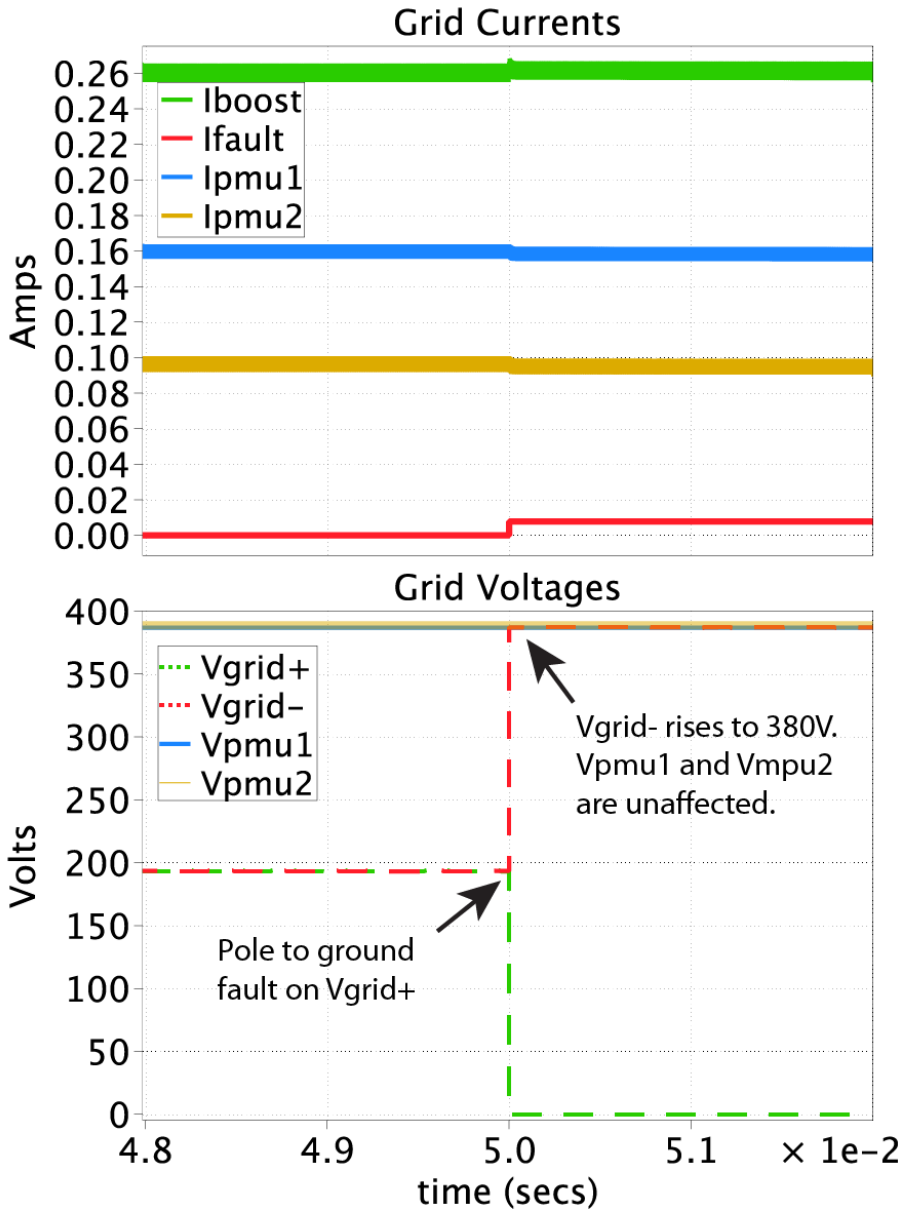

Figure 5.8: Simulation of a ground-fault on a high-resistance midpoint network. The current through the fault is limited by the $50k\Omega$ midpoint resistance. The voltage on the faulted line drops to 0V and the other pole voltage rises to 380V.

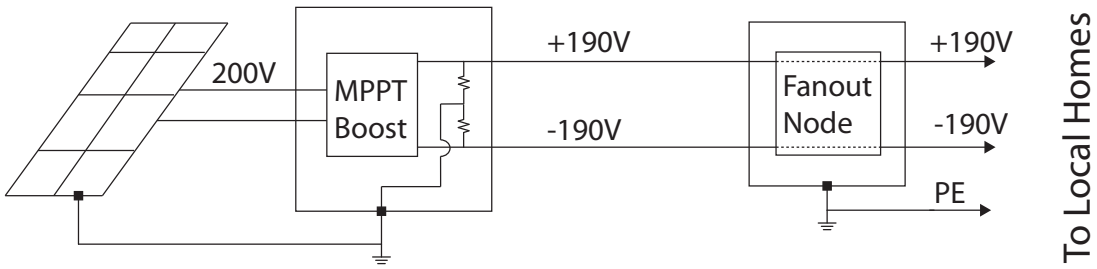

Figure 5.9: 2-Wire distribution of the 380V bus (+/- 190V) from the source converter to the fanout node. The PE line is connected to earth at the fanout node. The chassis of the fanout node is also connected to the PE line. The PE is distributed to a local cluster of households with the +/- 190V lines.

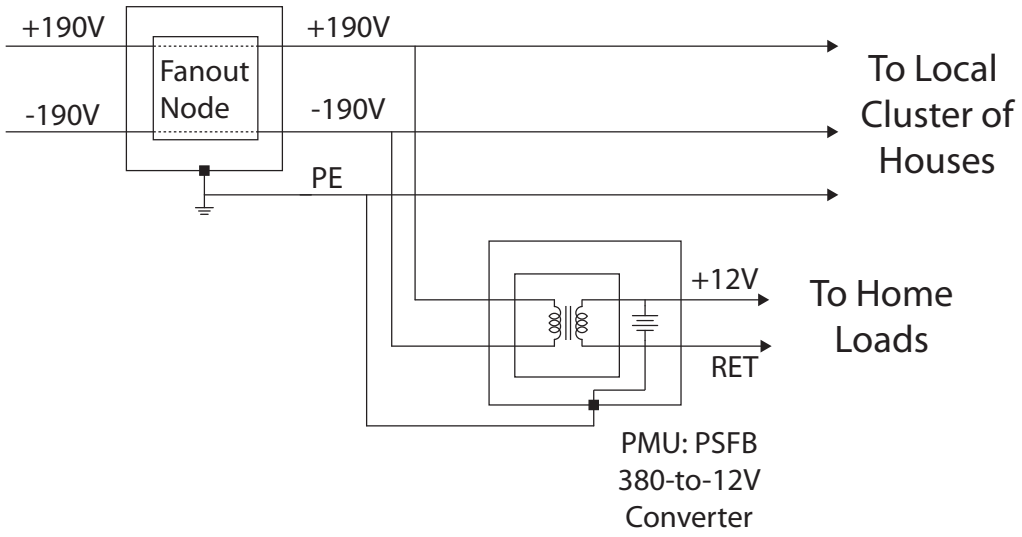

Figure 5.10: Grounding scheme from fanout nodes to the home PMU in a single-stage 380V architecture. +/- 190V and PE lines are distributed from the fanout node to a local cluster of households. The PE line is connected to the RET of the 380-to-12V PSFB converter inside the homes. The chassis of the PMU is also connected to the PE line.

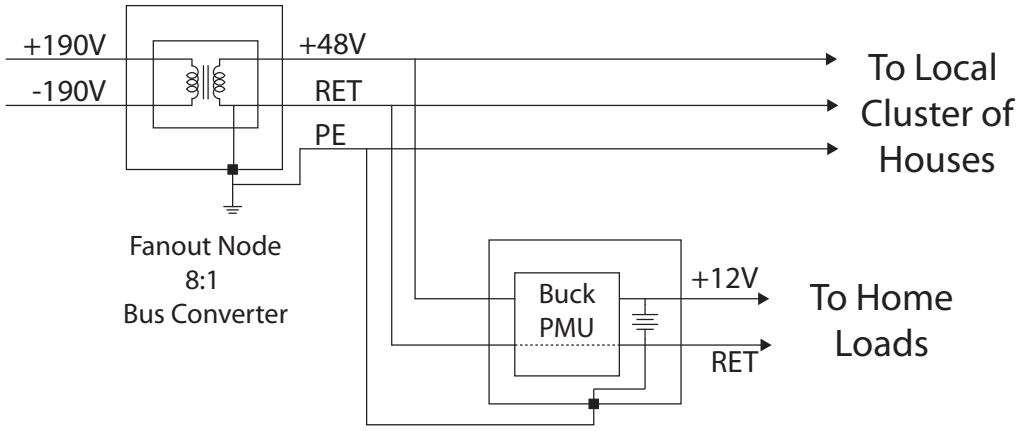

Figure 5.11: Grounding scheme from fanout nodes with integrated 380-to-48V fixed-ratio intermediate bus converters. The RET of the 48V line is connected to PE at the fanout node and +48V, RET and PE are distributed to the local cluster of houses. The 12V home bus is not isolated from the from the 48V fanout bus. However, the 380V bus is galvanically isolated from the local cluster 48V bus at the fanout node.

Therefore, having the negative-terminal of the battery grounded minimizes the chassis-to-earth potential for 12V appliances. Since there is galvanic-isolation between the primary to the secondary side of the 380-to-12V converter, the chassis of the PMU is also connected to the PE line. Figure 5.10 illustrates the grounding scheme from the fanout node to the connected homes on the system.

5.1.5.3 Fanout node with 2-stage 48V to home distribution

In the case where a two-stage conversion process is used to generate a 12V bus at each home, the fanout nodes integrate bus converter modules that step down the 380V distribution bus to a local 48V bus. The bus converter modules integrate a transformer and isolate the 380V bus on the primary side from the 48V bus on the secondary side. Figure 5.11 is an illustration of the distribution scheme from a fanout node to a local cluster of homes. The negative terminal of the 48V bus and the chassis of the fanout node are connected to earth with a low impedance connection—this results in a +48V distribution scheme. While a -48V scheme has been commonly used in telecom settings, it is not practical for our microgrid architecture since a non-isolated converter is used to step down from 48V to 12V at each home. If the +48V terminal was earth-connected in our microgrid, the voltages of the home 12V bus terminals would be at -48V and -36V (or 0 and -12V in single-stage conversion architecture) with respect to earth ground. Since both overhead transmission lines and thicker conductors are used, corrosion is not as big a concern as in telecom applications.

5.2 Protection Scheme

As shown in Section 5.1.5.1, the high-resistance midpoint grounding of the 380V bus ensures that pole-to-earth fault currents are kept low. However, such faults need to be detected with an RCD as the resulting fault currents will not be high enough to trip circuit breakers. The RCD functionality can be implemented within the source converter.

In addition to pole-to-earth faults, pole-to-pole faults on the +/- 190V bus need to be protected against by using appropriately sized DC fuses. In the experiments presented in Section 5.3.1, a 1A DC fuse with an $I^2 \cdot t$ rating of $1.28 A^2 \cdot$s is used.

On the 48V bus, the negative terminal is connected to earth ground through a low-impedance connection. Therefore, pole-to-pole faults and pole-to-earth faults are identical. The Vicor bus converter modules used in the two-stage conversion prototype system integrate both over-current and short circuit protection. The trip currents and response times are shown in Table 5.1.

Mode	Current Range	Response time
Over-current protection	$9 < I_{ocp} < 14$A	5ms
Short-circuit protection	$I_{scp} > 14$A	1.2μs

Table 5.1: Vicor BCM protection circuitry characteristics [12].

5.3 Fault Testing Experiments

Fault testing experiments were performed to test the DC microgrid's grounding scheme against pole-to-pole faults. There are two sets of experiments: (i) for 380V bus faults; and (ii) for 48V bus faults.

5.3.1 380V Bus Fault Testing

Simulation results presented in Figure 5.8 showcase the high-resistance grounding's role in limiting pole-to-earth fault currents on the 380V bus. The experiments presented in this section showcase the response of microgrid bus voltages and currents to pole-to-pole faults on the 380V bus.

The test setup for the fault experiments on the 380V bus is shown in Figure 5.12. A 400W 2-phase boost converter is used to generate the 380V bus. The 380V bus is connected to a 300W 8:1 fixed-ratio bus converter, which generates the 48V bus. Two 100W buck converter based PMUs are connected to the 48V bus. The PMUs each have a 12V 8Ah lead-acid battery for storage. A 1A DC fuse ($I^2 \cdot t$ =1.28A^2·s) is used as the pole-to-pole fault protection device. A 100A IGBT is connected to a fault resistor to generate a controllable fault. Table 5.2 shows the specification of the components used in the experiments.

Figure 5.13 shows the short (50 us) and long (10 ms) time period response of grid currents—$I_{Fuse-out}$, $I_{Fanout-in}$, I_{Fault}—to a low-impedance (11Ω) fault on the 380V bus. $I_{Fanout-in}$ supplies some of the initial current into the fault from the stored charge on the fanout node input capacitance; $I_{Fanout-in}$ decays to 0A after 50μs. The fault magnitude is sufficient to trip the protection fuse as can be seen in Figure 5.13b at 6ms. Figure 5.14 shows the grid voltages in response to the same fault over timespans of 10ms and 100ms respectively. V_{380} and V_{48} start to sag as the fault draws more power from the source. When the breaking point of the fuse is reached, the grid voltages downstream of the fuse (V_{380} and V_{48}) are de-energized very quickly. The voltage on the upstream side of the fuse (V_{Source}) rises to 400V and is stabilized by the over-voltage protection mode of the source converter.

The second type of faults tested were open-circuit faults. These are faults that occur when one of the power-lines breaks or is disconnected. The designed response for this type of fault is for the source converter voltage (V_{Source}) to float to 400V and be stabilized by the over-voltage protection scheme. Figure 5.15 shows the results from an open-circuit fault experiment. In this experiment, the IGBT was placed in series with the fuse on the

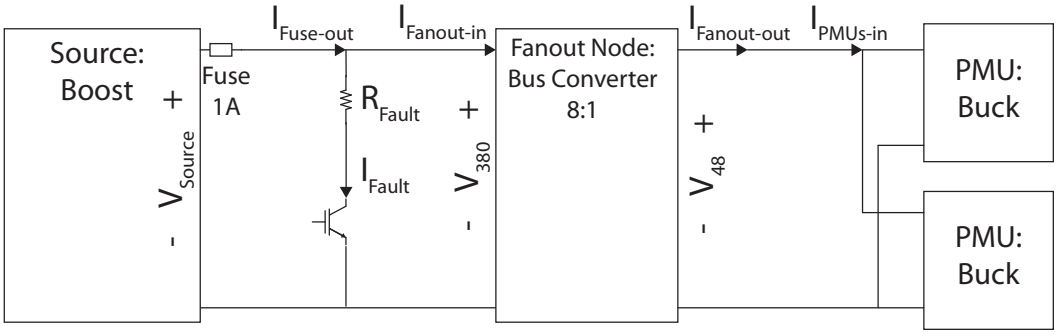

Figure 5.12: Test setup for fault testing on the 380V bus.

System Component	Specification	Power Rating
Source Converter	100kHz 2-phase boost converter	400W
Fanout Node	Vicor BCM 8:1 fixed ratio converter	300W
PMU	200kHz buck converter	100W

Table 5.2: Description of the microgrid components used for the fault experiments.

positive terminal of the source converter. The open-circuit fault was generated by driving the IGBT off. As soon as the source is disconnected, $I_{Fanout-in}$ immediately falls to zero. V_{380} and V_{48} also start to drop immediately after the fault. V_{Source} is again stabilized at 400V by the over-voltage protection scheme on the source converter.

5.3.2 Faults on 48V Bus

The fault protection on the 48V bus is integrated into the functionality of the bus converter modules as shown in Table 5.1. The experimental setup is similar to Figure 5.12 except that the IGBT module is placed on the 48V bus, i.e. on the secondary side of the fanout node.

In the first set of experiments, a 4Ω load was used to create a 12A fault across the 48V bus. This fault current triggers the over-current protection mode of the Vicor BCM as shown in Figure 5.16. Both V_{380} and V_{48} start to droop after the fault is triggered. At 42ms, the over-current protection shuts off the BCM output and all the voltages and currents immediately go to 0. This behavior is easily detectable at the fanout nodes.

The short-circuit response of the fanout node is shown in Figure 5.17. The same experiment setup as described above was used. The fault resistance was reduced to 2Ω. Figure 5.17 shows the short-circuit response over a 50us window. The short-circuit protection response is faster than the over-current protection response. As soon as a short-circuit condition is detected the BCM shuts off its output. This leads to the voltages and the currents on the 48V bus immediately falling to 0. V_{380} floats up due to the decreased load and is stabilized at 400V.

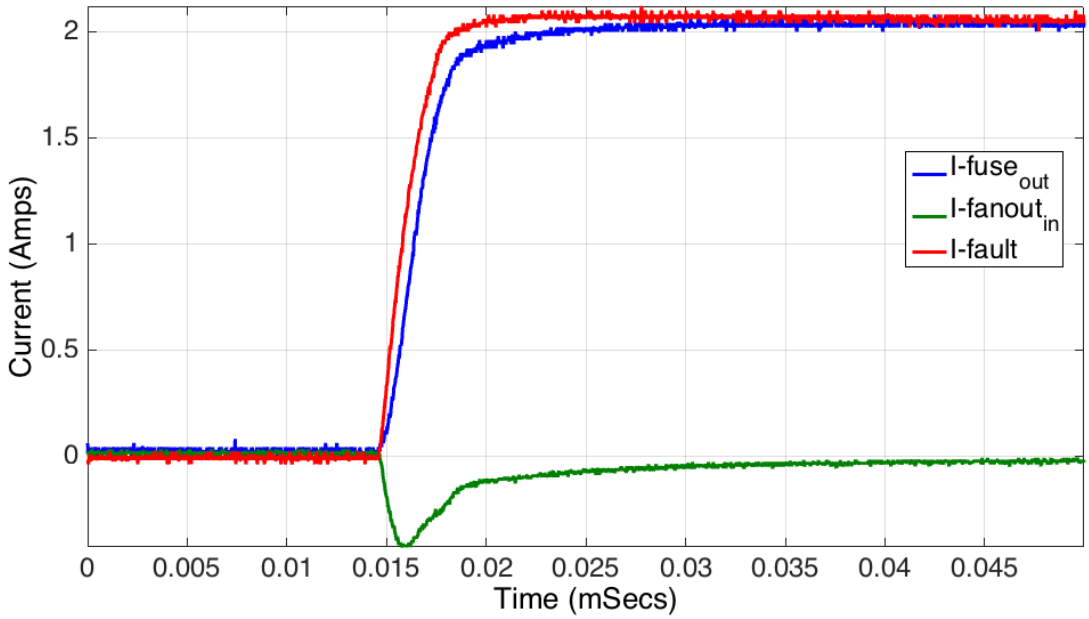

(a) Response over a 50 us time period

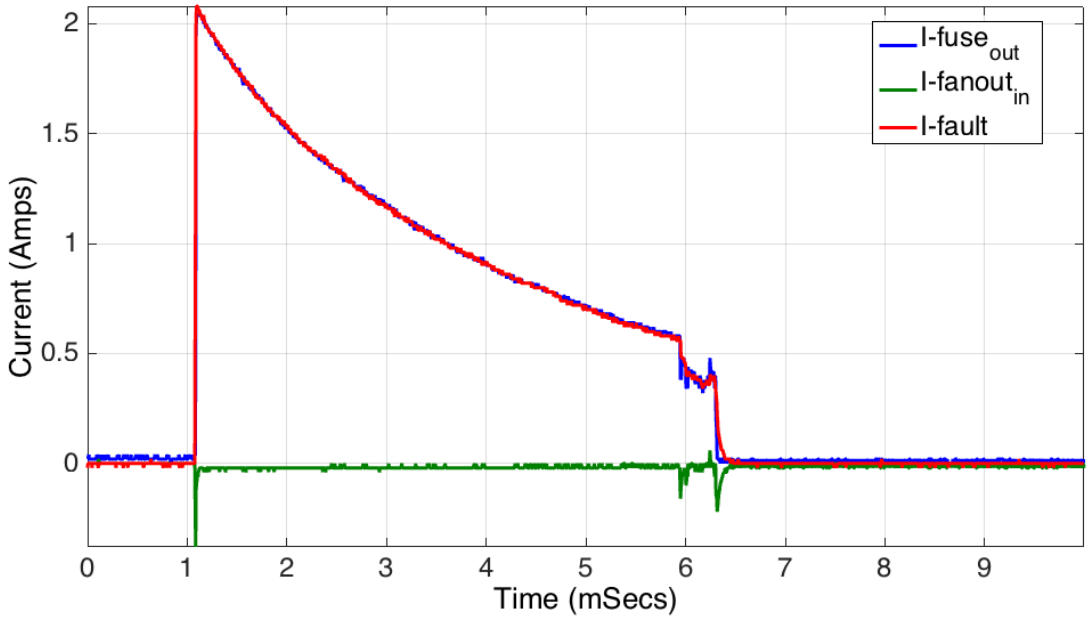

(b) Response over a longer 10 ms time period

Figure 5.13: Response of grid currents ($I_{Fuse-out}$, $I_{Fanout-in}$, I_{Fault}) to a pole-to-pole fault on the 380V bus. The fault impedance is 11 Ohms.

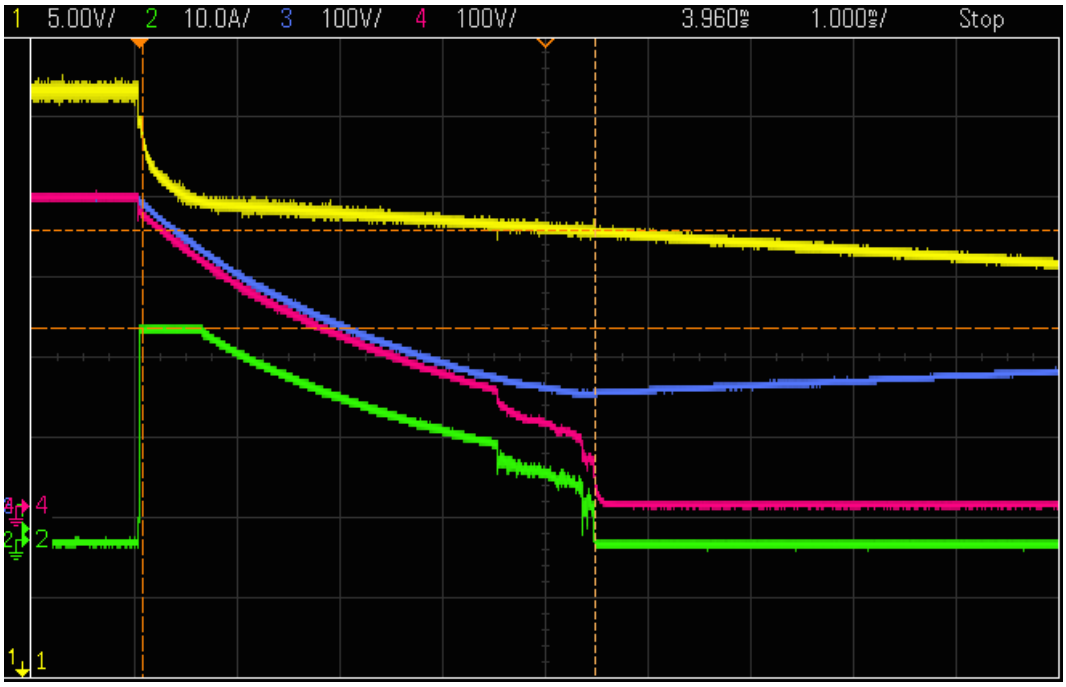

(a) Response over a 10 ms time period (1ms/div).

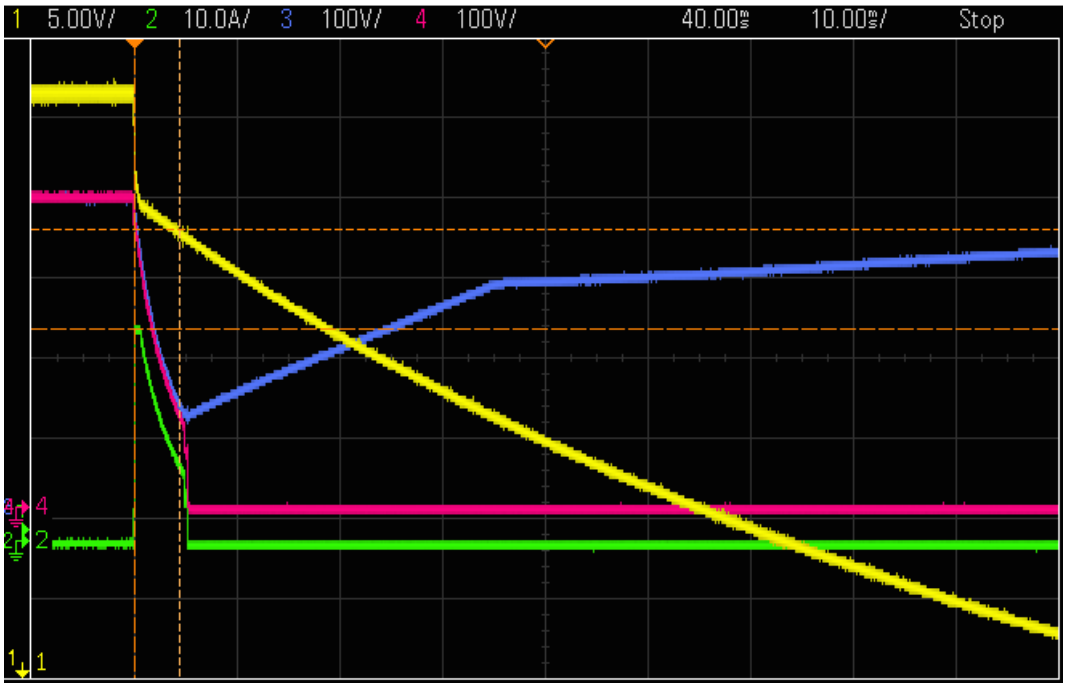

(b) Response over a 100 ms time period (10ms/div).

Figure 5.14: Response of grid voltages and currents to 11Ω fault on the 380V line. Ch-1 (yellow): V_{48} [5V/div], Ch-2 (green): $I_{Fanout-in}$ [10A/div], Ch-3 (blue): V_{Source} [100V/div], Ch-4 (pink): V_{380} [100V/div].

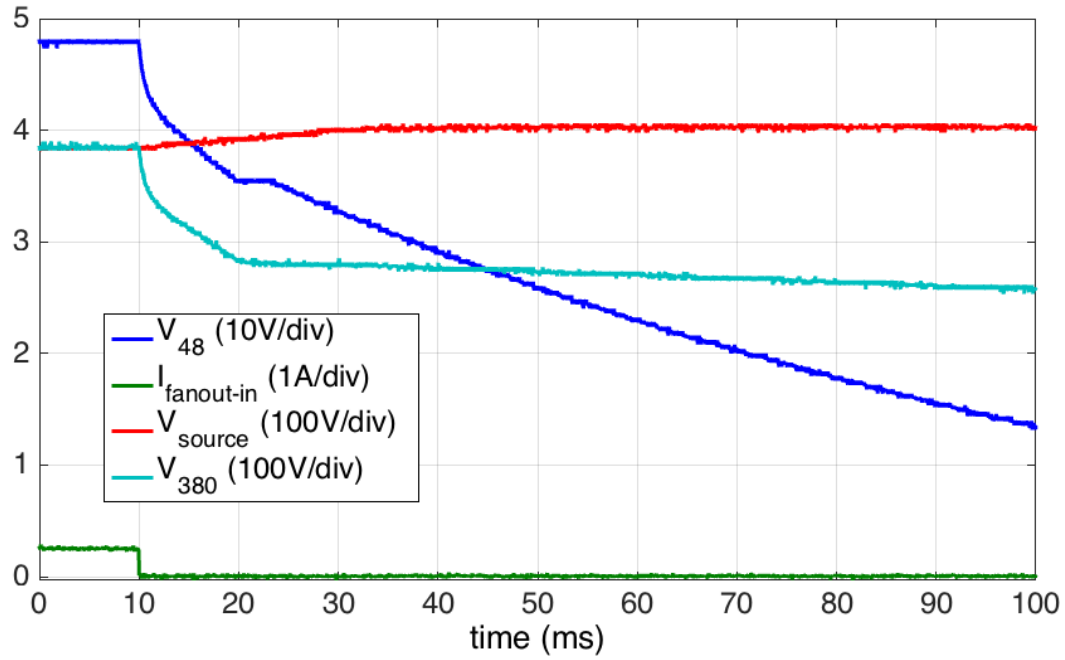

Figure 5.15: Response of V_{48}, $I_{Fanout-in}$, V_{Source}, and V_{380} to an open circuit fault on the +380V line over a 100ms period. V_{Source} is prevented from floating above 400V by the over-voltage protection implemented on the source converter.

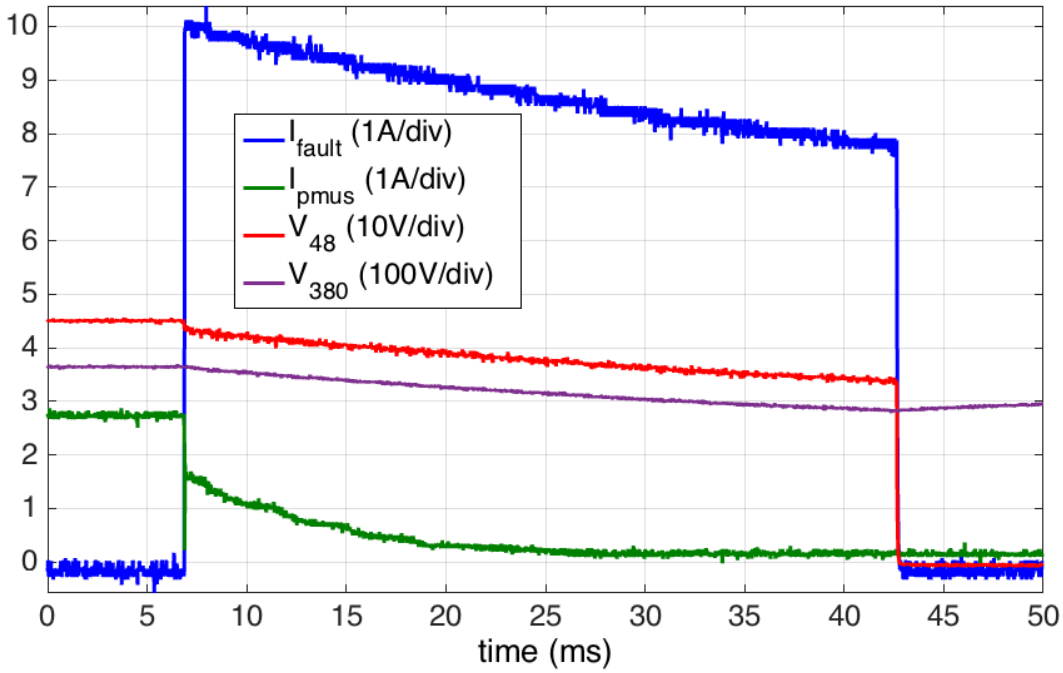

Figure 5.16: Over-current response of BCM converter over a 50ms time period. 48V bus pole-to-pole fault impedance is 4 Ohms.

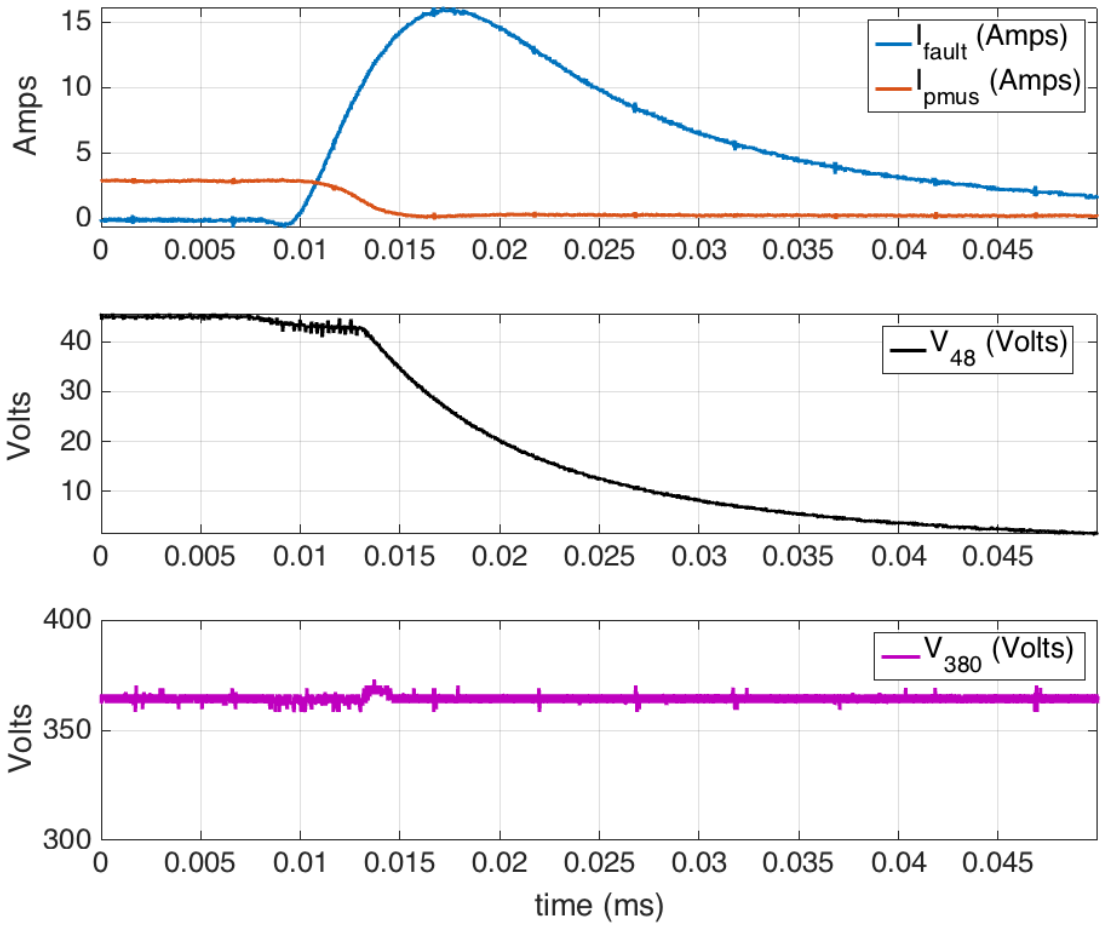

Figure 5.17: Short-circuit response of BCM converter over a 50us time period. 48V bus pole-to-pole fault impedance is 2 Ohms.

5.4 Conclusions

The grounding and protection architecture of the DC microgrid was informed by existing AC and DC distribution schemes. The 380V bus implements a high-resistance midpoint grounding scheme with fuse protection on the input to the grounding resistive bridge (Figure 5.9). This scheme has many safety advantages in comparison to other grounding options—the most import of which is a high-impedance limit to pole-to-earth fault currents as was shown in Figure 5.8. GFCI functionality is required to detect pole-to-earth faults and this can be integrated into the source converter operation.

A TT-type earthing scheme for the DC microgrid is shown to be both safe and cost-effective. Figs. 5.9, 5.10, and 5.11 illustrate the grounding scheme from the source converter to the homes PMUs in 2 different microgrid architectures—i) a 1-stage conversion scheme with 380V distribution to home, and ii) a 2-stage conversion scheme with 48V distribution to home. In both cases, a 2-wire +/- 190V scheme is used to distribute 380V power from the source converter to the fanout nodes of the system. A PE line is low-impedance grounded at the fanout nodes and distributed to the homes.

In a 1-stage scheme, +190V, -190V, and PE are distributed directly to the homes. The secondary side of an isolated 380-to-12V PMU converter is connected to the PE line.

In a 2-stage scheme, the negative terminal of the 48V bus is connected to ground at the fanout nodes to provide +48V, RET, and PE lines to the home converters. The output of the non-isolated PMU converters in the 2-stage scheme are connected to the PE line as well.

In both architectures, the PE line is connected to the output of the PMU at the negative terminal of the 12V battery. The household devices are provided +12V in a 2-wire scheme, which is the standard for 12V appliances.

Additional protection is required to protect against pole-to-pole faults. Experimental results verify that protective fuses are an effective approach to mitigate low impedance pole-to-pole faults. Over-voltage protection built into the control scheme of the source converter ensures that the voltage on the output terminals of the source does not exceed 400V.

In a 2-stage scheme, over-current and short-circuit protection functionality of the 48V bus is integrated into the Vicor BCM converters. This protection functionality has also been experimentally verified.

This chapter has presented and verified a safe and cost-effective approach to grounding and protection of a DC microgrid designed for rural electrification.

Chapter 6

Conclusions and Recommendations for Future Research

6.1 Conclusions

This dissertation showed the motivations for a smart and scalable DC microgrid for rural electrification of emerging regions. The design of microgrid architecture and functionality of microgrid hardware were informed by: (i) current trends in renewable energy technologies, and (ii) the energy needs of rural unelectrified populations. Efficiency of stored electricity, η_{stored}, was established as a key figure-of-merit. A DC microgrid with distributed storage was shown to enhance η_{stored} in comparison to an equivalent AC microgrid. In addition, the scalability of distributed storage was shown to address the challenge of accurately sizing an off-grid system for initial electricity demand while allowing for customer driven growth of storage capacity.

The distributed load-line control scheme implemented on the power management units (PMUs) of the DC microgrid was designed for grid voltage regulation and enabled power sharing. It was shown through both simulations and experiments that the load-line scheme regulated grid voltage effectively over a wide range of grid operating conditions. Effective control of power flow with the control scheme was also shown.

Two prototype versions of microgrid hardware were implemented. The first-generation microgrid architecture utilized a phase-shifted full-bridge topology for power conversion in the PMUs. The PMUs converted the 380V distribution bus to 12V for household usage in a single stage. However, concerns with low-load efficiency, and the cost of converter hardware prompted a switch to a 2-stage conversion topology for the second-generation of microgrid hardware.

The second-generation microgrid architecture utilized fixed-ratio (8:1) DC bus converters to generate intermediate 48V buses for local clusters of houses. These bus converters were integrated into the fanout nodes of the microgrid. The converter topology in the PMUs was changed to a buck topology. Despite an addition conversion step compared to

the first-generation microgrid architecture, the second-generation architecture was shown to be more efficient over a wider range of operating conditions. In addition, the overall system hardware cost was also reduced. The LCOE of the DC microgrid over a 15 year timespan was estimated to be less than $0.35 per kWhr with the second-generation architecture.

Protection and earthing schemes for the DC microgrid were discussed in detail. Motivations behind existing protection and earthing schemes were considered and a detailed grounding scheme for the DC microgrid was presented. This grounding scheme was informed by existing standards and best practices. Experiments were conducted to verify the protection schemes and protection hardware.

The smart and scalable DC microgrid described in this dissertation showed significant promise as an approach for cost-effective and scalable electrification of rural emerging regions.

6.2 Future Directions for Research

There are a number of avenues for future research related to developing a more efficient and scalable DC microgrid system. Some of these directions are outlined below.

6.2.1 Digital Communications

Integrating digital communications in the various components of the microgrid will allow for control of power-flow between different PMUs, as described in Chapters 1, and 2. The communications system can aggregate usage information from the connected PMUs. By sending price signals to PMUs, the microgrid operator can control power flow. Load prioritization and demand-response can be enabled by this methodology.

6.2.2 Accurate usage and behavioral data measurements

While there are prior studies that have observed customer usage patterns and behaviors for conventional microgrids, there are many open questions as to how these patterns will be affected by a microgrid that is designed around distributed storage. The motivations for distributed storage have been explored in detail, but there is very limited existing data of user behaviors in such a system.

In general, data on electricity usage over time is very valuable in informing the hardware specifications of microgrids. Obtaining data related to the growth in demand of electricity will lead to better design optimization of future microgrid hardware.

6.2.3 Power Electronics Hardware Optimizations and Revisions

While the power electronics architecture of the PMUs and the fanout nodes has been explored in depth in this dissertation, there are still many avenues to improve efficiency and reduce costs. Customer usage data can be utilized to optimize the size of individual converters, thereby improving conversion efficiencies and reducing capital costs.

The 2-stage conversion architecture was driven by the desire to reduce converter hardware costs and improve low-load conversion efficiency with readily available hardware; hardware such as commercially available dc bus converters, and buck converter control ICs. However, a single-stage conversion architecture has the potential to increase system efficiency if it is appropriately sized to match household power usage patterns.

Also, the design of the source converter was not optimized over the course of this dissertation. An investigation into a more efficient topology would be worthwhile.

Lastly, while it is anticipated that most household appliances will be 12VDC devices, it is possible that customers would also use 120-240VAC appliances. While there are off-the-shelf inverters that will convert from 12V to 120-240VAC, these inverters are not the most efficient solution. It is possible to use the 380V bus to directly generate an AC waveform more efficiently and at lower cost. Integrating this functionality into the PMUs is also another possible investigation.

6.2.4 Distributed Peak Power Tracking Implemented by the PMUs

It might be possible to fully distribute the functionality of the source converter to the grid-connected PMUs. The source converter is responsible for operating the installed solar panels at their peak power point. However, since all the PMUs are implementing a load-line control scheme, it is possible that a distributed peak power tracking (PPT) algorithm can be implemented by the PMUs themselves. An architecture where each PMU implements an observe-and-perturb algorithm might be able to remove the need for a dedicated PPT source converter for the solar panels. Some preliminary simulations were performed in this avenue and showed promise. The main challenge in designing a distributed PPT scheme is to ensure that unique power-flow solutions can be achieved for all microgrid operating conditions.

Also, the economic motivation for a distributed PPT scheme needs to investigated as there would be some loss of solar PV operational efficiency. However, this might be a cost-benefit trade-off that is worthwhile. The unit costs of solar panels have decreased significantly in the past few years. There might be a net economic benefit to removing the source converter hardware at the cost of slightly increasing the size of the installed PV.

Bibliography

[1] WORLD ENERGY OUTLOOK 2011 FACTSHEET. *IEA World Energy Outlook 2011*, November 2011.

[2] P Alstone, D Gershenson, and D M Kammen. Decentralized energy systems for clean electricity access. *Nature Climate Change*, 2015.

[3] Bernard Tenenbaum and et al. From the bottom up: How small power producers and mini-grids can deliver electrification and renewable energy in Africa. *World Bank Publications*, 2014.

[4] P. Bardouille, P. Avato, J. Levin, A. Pantelias, and H. Engelmann-Pilger. From gap to opportunity: Business models for scaling up energy access. *International Finance Corporation*, 2012.

[5] D Schnitzer, DS Lounsbury, JP Carvallo, et al. Micro-grids for rural electrification: A critical review of best practices based on seven case studies. *Published by the United Nations Foundation*, pages 83–99, 2014.

[6] W. Stevens and G. P. Corey. A study of lead-acid battery efficiency near top-of-charge and the impact on PV system design. *Photovoltaic Specialists Conference, 1996., Conference Record of the Twenty Fifth IEEE*, pages 1485–1488, 1996.

[7] Alan Colin Brent and David E Rogers. Renewable rural electrification: Sustainability assessment of mini-hybrid off-grid technological systems in the African context. *Renewable Energy*, 35(1):257–265, January 2010.

[8] Power supplies: A hidden opportunity for energy savings. *A NRDC report prepared for Natural Resources Defense Council, San Francisco, CA*, 2002.

[9] Wikipedia contributors. Earthing system. *Wikipedia, The Free Encyclopedia*, 2015.

[10] N Tullius. Three-wire DC distribution to telecommunication equipment. In *Telecommunications Energy Conference, 1994. INTELEC '94., 16th International*, pages 297–300, 1994.

[11] K Hirose, T Tanaka, T Babasaki, et al. Grounding concept considerations and recommendations for 400VDC distribution system. In *Telecommunications Energy Conference (INTELEC), 2011 IEEE 33rd International*, pages 1–8. IEEE, 2011.

[12] Vicor BCM Bus Converter Module. *[Online] Available: http://www.vicorpower.com/dc-dc-converters-board-mount/bus-converter-module.*

[13] Energy for all: financing access for the poor. Technical report, IEA World Energy Outlook, 2011.

[14] M Nouni, S Mullick, and T Kandpal. Providing electricity access to remote areas in India: An approach towards identifying potential areas for decentralized electricity supply. *Renewable & Sustainable Energy Reviews*, 12(5):1187–1220, June 2008.

[15] Leena Srivastava and I H Rehman. Energy for sustainable development in India: Linkages and strategic direction. *Energy Policy*, 34(5):643–654, March 2006.

[16] D Soto, E Adkins, M Basinger, and R Menon. A prepaid architecture for solar electricity delivery in rural areas. In *Proceedings of the Fifth International Conference on Information and Communication Technologies and Development. ACM*, pages 130–138, 2012.

[17] Daniel Soto, Edwin Adkins, Matt Basinger, et al. A prepaid architecture for solar electricity delivery in rural areas. In *Proceedings of the Fifth International Conference on Information and Communication Technologies and Development - ICTD '12*, page 130, New York, New York, USA, March 2012. ACM Press.

[18] Javier Rosa, P. Achintya Madduri, and Daniel Soto. Efficient Microgrid Management System for Electricity Distribution in Emerging Regions. In *Global Humanitarian Technology Conference (GHTC), 2012 IEEE*, pages 23–26. IEEE, 2012.

[19] S Komatsu, S Kaneko, and P P Ghosh. Are micro-benefits negligible? The implications of the rapid expansion of Solar Home Systems (SHS) in rural Bangladesh for sustainable development. *Energy Policy*, 2011.

[20] V Modi. Improving electricity services in rural India. Technical report, 2005.

[21] Richard Martin. India's Energy Crisis. *MIT Technology Review*, October 2015.

[22] Dushan Boroyevich, Igor Cvetkovic, Dong Dong, et al. Future electronic power distribution systems a contemplative view. In *2010 12th International Conference on Optimization of Electrical and Electronic Equipment*, pages 1369–1380. IEEE, May 2010.

[23] Wei Zhang, Dong Dong, I Cvetkovic, F Lee, and D Boroyevich. Lithium-based energy storage management for DC distributed renewable energy system. *Energy Conversion Congress and Exposition (ECCE), 2011 IEEE*, pages 3270–3277, 2011.

[24] D Soto and V Modi. Simulations of Efficiency Improvements Using Measured Microgrid Data. *Global Humanitarian Technology Conference (IGHTC), 2012 IEEE*, pages 369–374, 2012.

[25] T G Quetchenbach, M J Harper, J Robinson IV, et al. The GridShare solution: a smart grid approach to improve service provision on a renewable energy mini-grid in Bhutan. *Environmental Research Letters*, 8(1):014018, 2013.

[26] Emerge Alliance. [Online] Available: http://www.emergealliance.org.

[27] P A Madduri, J Rosa, S.R. Sanders, E A Brewer, and M Podolsky. Design and verification of smart and scalable DC microgrids for emerging regions. In *Energy Conversion Congress and Exposition (ECCE), 2013 IEEE*, pages 73–79. IEEE, 2013.

[28] S.R. Sanders, J M Noworolski, X Z Liu, and George C Verghese. Generalized averaging method for power conversion circuits. *Power Electronics, IEEE Transactions on*, 6(2):251–259, 1991.

[29] S.R. Sanders and George C Verghese. Lyapunov-based control for switched power converters. *Power Electronics, IEEE Transactions on*, 7(1):17–24, 1992.

[30] Li Zhang, Tianjin Wu, Yan Xing, Kai Sun, and Josep M Gurrero. Power control of DC microgrid using DC bus signaling. *Applied Power Electronics Conference and Exposition (APEC), 2011 Twenty-Sixth Annual IEEE*, pages 1926–1932, November 2010.

[31] Wei Jiang and Yu Zhang. Load Sharing Techniques in Hybrid Power Systems for DC Micro-Grids. *Power and Energy Engineering Conference (APPEEC), 2011 Asia-Pacific*, pages 1–4, 2011.

[32] J A Sabate, V Vlatkovic, R.B. Ridley, F Lee, and B H Cho. Design considerations for high-voltage high-power full-bridge zero-voltage-switched PWM converter. In *Applied Power Electronics Conference and Exposition, 1990. APEC '90, Conference Proceedings 1990., Fifth Annual*, pages 275–284, 1990.

[33] V Vlatkovic, J A Sabate, R.B. Ridley, F.C Lee, and B H Cho. Small-signal analysis of the phase-shifted PWM converter. *Power Electronics, IEEE Transactions on*, 7(1):128–135, 1992.

[34] M J Schutten and D A Torrey. Improved small-signal analysis for the phase-shifted PWM power converter. *Power Electronics, IEEE Transactions on*, 18(2):659–669, March 2003.

[35] Phase-Shifted Full Bridge DC/DC Power Converter. *[Online] Available: http://www.ti.com/tool/TIDM-PSFB-DCDC.*

[36] High Voltage Isolated Solar MPPT Developers Kit. *[Online] Available:http://www.ti.com/tool/TMDSHVMPPTKIT.*

[37] P A Madduri, J Poon, J Rosa, et al. A scalable dc microgrid architecture for rural electrification in emerging regions. In *Applied Power Electronics Conference and Exposition (APEC), 2015 IEEE*, pages 703–708. IEEE, 2015.

[38] Texas Instruments WEBENCH Power Designer. *[Online] Available: http://www.ti.com/lsds/ti/analog/webench/power.page.*

[39] Angel V Peterchev and Seth R Sanders. Load-Line Regulation With Estimated Load-Current Feedforward: Application to Microprocessor Voltage Regulators. *Power Electronics, IEEE Transactions on*, 21(6):1704–1717.

[40] R Redl and N O Sokal. Near-Optimum Dynamic Regulation of DC-DC Converters Using Feed-Forward of Output Current and Input Voltage with Current-Mode Control. *Power Electronics, IEEE Transactions on*, (3):181–192, 1986.

[41] Wikipedia contributors. Residual-current device. *Wikipedia, The Free Encyclopedia*, 2015.

[42] Richard Levine. Why Positive Power Ground in Telephone Subscriber Loops? *[Online] Available: http://lyle.smu.edu/ levine/ee8320/positiveground.pdf*, September 2002.

[43] Emerson Network Power. NetSure 4015. (EN609DRA-NS4015 / 0913), September 2013.

[44] Vicor. 400V DC Microgrid Small Scale Demo System for Telecom and Datacom Applications. In *Telecommunications Energy Conference, 2012 INTELEC 2012. 34th International IEEE.*

[45] S Backhaus, G W Swift, S Chatzivasileiadis, and W Tschudi. DC Microgrids Scoping Study—Estimate of Technical and Economic Benefits. Technical report, Los Alamos National Laboratory, 2015.

Appendix A

Wiring Recommendations

There are multiple wire types that were found to be applicable for the microgrid distribution wiring. In general for the +/-190V 2-wire distribution network, an aluminum cable would be the most cost effective option. Bare aluminum conductor steel reinforced (ACSR) cable is the most economical high capacity conductor that is applicable. ACSR cable is typically used for overhead power transmission lines. The 6 AWG version of this conductor has an allowable capacity of 105 Amps. The cost of this conductor can be as low as $0.10 per meter.

THHN copper wire is used in buildings for AC wiring. 14 AWG THHN is available for $0.40 per meter. While copper wire is more expensive than aluminum wire, copper wire is easier to terminate. THHN conductor might be more applicable for connection from the fanout node to the houses as this is typically the last 15 meters of the distribution network and wiring costs would not be too high for shorter runs.

Datasheets for both ACSR and THHN wire are provided in the following pages.

Included Documents:

1. Southwire ACSR catalog (2 pages)
2. Automation Direct THHN wire catalog (3 pages)

ACSR

Aluminum Conductor. Steel Reinforced . Bare.

APPLICATIONS

Used as bare overhead transmission conductor and as primary and secondary distribution conductor and messenger support. ACSR offers optimal strength for line design. Variable steel core stranding enables desired strength to be achieved without sacrificing ampacity.

SPECIFICATIONS

Southwire's ACSR bare conductor meets or exceeds the following ASTM specifications:

- B230 Aluminum 1350-H19 Wire for Electrical Purposes.
- B232 Concentric-Lay-Stranded Aluminum Conductors, Coated-Steel Reinforced (ACSR).
- B498 Zinc-Coated (Galvanized) Steel Core Wire for Use in Overhead Electrical Conductors.
- B500 Metallic Coated Stranded Steel Core for Use in Overhead Electrical Conductors.

CONSTRUCTION

- Aluminum 1350-H19 wires, concentrically stranded about a steel core. Standard core wire for ACSR is class A galvanized.
- Class A core stranding is also available in zinc-5% aluminum-mischmetal alloy coating.
- For aluminum-clad (AW) ACSR, please refer to the ACSR/AW catalog sheet
- Additional corrosion protection is available through the application of grease to the core or infusion of the complete cable with grease.
- ACSR conductor is also available in non-specular.

Southwire
One Southwire Drive
Carrollton, Ga. 30119 USA

MADE IN ★ THE USA

ACSR

Code Word	Size (AWG or kcmil)	Strand-ing (Al/Stl)	Diameter (ins.)				Weight Per 1000 ft. (lbs.)			Content (%)		Rated Strength (lbs.)	Resistance OHMS/1000 ft.		Allowable Ampacity+ (Amps)
			Individual Wires		Steel Core	Complete Cable	Al	Stl	Total	Al	Stl		DC @ 20°C	AC @ 75°C	
			Al	Stl											
Turkey	6	6/1	.0661	.0661	.0661	.198	24	12	36	67.88	32.12	1190	.641	.806	105
Swan	4	6/1	.0834	.0834	.0834	.25	39	18	57	67.87	32.12	1860	.403	.515	140
Swanate	4	7/1	.0772	.103	.103	.257	39	28	67	58.1	41.9	2360	.399	.519	140
Sparrow	2	6/1	.1052	.1052	.1052	.316	62	29	91	67.9	32.1	2850	.254	.332	184
Sparate	2	7/1	.0974	.1298	.1298	.325	62	45	107	58.12	41.88	3460	.251	.338	184
Robin	1	6/1	.1181	.1181	.1181	.354	78	37	115	67.88	32.12	3550	.201	.268	212
Raven	1/0	6/1	.1327	.1327	.1327	.398	99	47	145	67.89	32.11	4380	.159	.217	242
Quail	2/0	6/1	.1489	.1489	.1489	.447	124	59	183	67.88	32.12	5310	.126	.176	276
Pigeon	3/0	6/1	.1672	.1672	.1672	.502	156	74	230	67.87	32.13	6620	.100	.144	315
Penguin	4/0	6/1	.1878	.1878	.1878	.563	197	93	291	67.88	32.12	8350	.0795	.119	357
Waxwing	266.8	18/1	.1217	.1217	.1217	.609	250	39	289	86.43	13.57	6880	.0643	.0787	449
Partridge	266.8	26/7	.1013	.0788	.2363	.642	251	115	367	68.51	31.49	11300	.0637	.0779	475
Ostrich	300	26/7	.1074	.0835	.2506	.68	283	130	412	68.51	31.49	12700	.0567	.0693	492
Merlin	336.4	18/1	.1367	.1367	.1367	.684	315	49	365	86.43	13.57	8680	.0510	.0625	519
Linnet	336.4	26/7	.1137	.0885	.2654	.72	317	146	462	68.51	31.49	14100	.0505	.0618	529
Oriole	336.4	30/7	.1059	.1059	.3177	.741	318	209	526	60.35	39.65	17300	.0502	.0613	535
Chickadee	397.5	18/1	.1486	.1486	.1486	.743	373	58	431	86.43	13.57	9940	.0432	.0529	576
Brant	397.5	24/7	.1287	.0858	.2574	.772	374	137	511	73.21	26.79	14600	.0430	.0526	584
Ibis	397.5	26/7	.1236	.0962	.2885	.783	374	172	546	68.51	31.49	16300	.0428	.0523	587
Lark	397.5	30/7	.1151	.1151	.3453	.806	375	247	622	60.35	39.65	20300	.0425	.0519	594
Pelican	477	18/1	.1628	.1628	.1628	.814	447	70	517	86.44	13.56	11800	.0360	.0442	646
Flicker	477	24/7	.141	.094	.2819	.846	449	164	614	73.21	26.79	17200	.0358	.0439	655
Hawk	477	26/7	.1354	.1053	.316	.858	449	207	656	68.51	31.49	19500	.0356	.0436	659
Hen	477	30/7	.1261	.1261	.3783	.883	450	296	746	60.35	39.65	23800	.0354	.0433	666
Osprey	556.5	18/1	.1758	.1758	.1758	.879	522	82	603	86.43	13.57	13700	.0308	.0379	711
Parakeet	556.5	24/7	.1523	.1015	.3045	.914	524	192	716	73.21	26.79	19800	.0307	.0376	721
Dove	556.5	26/7	.1463	.1138	.3413	.927	524	241	765	68.51	31.49	22600	.0306	.0375	726
Eagle	556.5	30/7	.1362	.1362	.4086	.953	525	345	871	60.35	39.65	27800	.0303	.0372	734
Peacock	605	24/7	.1588	.1059	.3177	.953	570	209	779	73.2	26.8	21600	.0282	.0346	760
Squab	605	26/7	.1525	.1186	.3559	.966	570	262	832	68.51	31.49	24300	.0281	.0345	765
Wood Duck	605.0	30/7	.142	.142	.426	.994	571	375	946	60.35	39.65	28900	.0279	.0342	774
Teal	605.0	30/19	.142	.0852	.426	.994	571	367	939	60.86	39.14	30000	.0279	.0342	773
Kingbird	636	18/1	.188	.188	.188	.94	596	94	690	86.43	13.57	15700	.0270	.0332	773
Swift	636.0	36/1	.1329	.1329	.1329	.93	596	47	643	92.72	7.28	13690	.0271	.0334	769
Rook	636	24/7	.1628	.1085	.3256	.977	599	219	818	73.22	26.78	22600	.0268	.0330	784
Grosbeak	636	26/7	.1564	.1216	.3649	.991	599	275	874	68.51	31.49	25200	.0267	.0328	789

Prices as of April 15, 2015. Check Web site for most current prices.

Wire - Type THHN

Applications

Type THHN building wire is intended for general purpose applications as defined by the National Electrical Code (NEC). Type THHN is permitted for new construction or rewiring for 600-volt applications. For applications requiring Type THHN, the conductor is appropriate for use in wet or dry locations at temperatures not to exceed 90°C or not to exceed 75°C in oil or coolants. Slick nylon outer jacket for easy pulling. All sizes rated gasoline and oil resistant II. THHN wire 6AWG and larger Sunlight Resistant in all colors.

THHN wire is sold in 500 foot spools; certain sizes are also available in 2500 foot reels.

Features

Conductors

- Stranded, uncoated copper conductors per ASTM-B3, ASTM-B787 and ASTM-B8

Insulation

Color-coded Polyvinyl Chloride (PVC), heat and moisture-resistant, flame-retardant compound per UL-1063 and UL-83

Jacket

A tough, polyamide, Nylon outer covering per UL-1063 and UL-83

Standards

UL Standards UL-83, UL-1063, UL-758
AWM Spec 1316, 1317, 1318, 1319, 1320, 1321
ASTM Stranding Class B3, B8, B787
Federal Specification A-A-59544
Canadian Standards Association C22.2 No. 75
NEMA WC70/ICEA S-95-658
ICEA T-29-520 (210,000 Btu/hr) Flame Test
ARRA 2009; Section 1605 "Buy American" Compliant
RoHS

Type THHN Wire

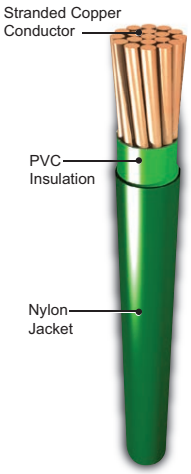

Type THHN Wire Specifications

Size (AWG or kcmil)	Number of Strands	Cross-sectional Area (mm^2)	Insulation Thickness (inches)		Overall Outside Diameter		Allowable Ampacities*			Approximate Weight (lbs) 500'/2500'	Standard Packaging spool/reel
			PVC	Nylon	(inches)	(mm)	60°C	75°C	90°C		
14	19	6.258	0.015	0.004	0.109	2.77	15	20	25	7.8 / 42.2	500' or 2500'. Some colors not offered in 2500' reel.
12	19	8.581	0.015	0.004	0.127	3.23	20	25	30	11.7 / 61.4	
10	19	13.61	0.015	0.004	0.160	4.07	30	35	40	18.7	500'
8	19	23.61	0.030	0.005	0.212	5.39	40	50	55	31.4	
6	19	32.71	0.030	0.005	0.248	6.30	55	65	75	48.5	
4	19	53.16	0.040	0.006	0.317	8.06	70	85	95	75.4	

Note: Allowable ampacity shown above is per the National Electric Code. The above data is approximate and subject to normal manufacturing tolerances.

Please Note: Our prices on wire are closely tied to the market price for copper. This allows us to offer the best savings possible if conditions are favorable; however, it also means that our prices may increase if market conditions warrant.

Prices as of April 15, 2015. Check Web site for most current prices.

Wire - Type THHN

Type THHN Wire						
Part Number	***Insulation Color***	***Gauge***	***Description***	***Spool/Reel Length***	***Approx. Weight***	***Price***
THHN14BK	Black	14AWG	Type THHN wire, bare copper, 19 strands, 600 Volts	500'	7.8 lbs	$62.00
THHN14WH	White					$62.00
THHN14RD	Red					$62.00
THHN14BL	Blue					$62.00
THHN14GN	Green					$62.00
THHN14YL	Yellow					$62.00
THHN14OR	Orange					$62.00
THHN14BN	Brown					$62.00
THHN14PL	Purple					$62.00
THHN14GY	Gray					$62.00
THHN14GYL	Green with Yellow spiral stripe					$62.00
THHN14BW	Blue with White spiral stripe					$62.00
THHN12BK	Black	12AWG	Type THHN wire, bare copper, 19 strands, 600 Volts		11.7 lbs	$92.00
THHN12WH	White					$92.00
THHN12RD	Red					$92.00
THHN12BL	Blue					$92.00
THHN12GN	Green					$92.00
THHN12YL	Yellow					$92.00
THHN12OR	Orange					$92.00
THHN12BN	Brown					$92.00
THHN12GY	Gray					$92.00
THHN12GYL	Green with Yellow spiral stripe					$92.00
THHN10BK	Black	10AWG	Type THHN wire, bare copper, 19 strands, 600 Volts		18.7 lbs	$142.00
THHN10WH	White					$142.00
THHN10GN	Green					$142.00
THHN10YL	Yellow					$142.00
THHN10OR	Orange					$142.00
THHN10BN	Brown					$142.00
THHN10GYL	Green with Yellow spiral stripe					$142.00
THHN8BK	Black	8AWG	Type THHN wire, bare copper, 19 strands, 600 Volts		31.4 lbs	$239.00
THHN8GN	Green					$239.00
THHN8GYL	Green with Yellow spiral stripe					$239.00
THHN6BK	Black	6AWG	Type THHN wire, bare copper, 19 strands, 600 Volts		48.5 lbs	$363.00
THHN4BK	Black	4AWG	Type THHN wire, bare copper, 19 strands, 600 Volts		75.4 lbs	$659.00

Prices as of April 15, 2015. Check Web site for most current prices.

Wire - Type THHN

Type THHN Wire						
Part Number	**Color**	**Gauge**	**Description**	**Spool/Reel Length**	**Approx. Weight**	**Price**
THHN14BK25	Black	14AWG	Type THHN wire, bare copper, 19 strands, 600 Volts	2500'	42.2 lbs	$310.00
THHN14WH25	White					$310.00
THHN14RD25	Red					$310.00
THHN14BL25	Blue					$310.00
THHN14GN25	Green					$310.00
THHN14YL25	Yellow					$310.00
THHN14OR25	Orange					$310.00
THHN14BN25	Brown					$310.00
THHN14PL25	Purple					$310.00
THHN14GY25	Gray					$310.00
THHN14BW25	Blue with White spiral stripe					$310.00
THHN12BK25	Black	12AWG	Type THHN wire, bare copper, 19 strands, 600 Volts		61.4 lbs	$465.00
THHN12WH25	White					$465.00
THHN12RD25	Red					$465.00
THHN12BL25	Blue					$465.00
THHN12GN25	Green					$465.00
THHN12YL25	Yellow					$465.00
THHN12OR25	Orange					$465.00
THHN12BN25	Brown					$465.00

Gauge Conversion Table

*American Wire Gauge Conversion Chart**			
This cross reference shows equivalent nominal values. Actual cross sections may vary.			
AWG	**mm²**	**AWG**	**mm²**
30	0.05	6	16
28	0.08	4	25
26	0.14	2	35
24	0.25	1	50
22	0.34	1/0	55
21	0.38	2/0	70
20	0.50	3/0	95
18	0.75	4/0	120
17	1.00	300MCM	150
16	1.50	350MCM	185
14	2.50	500MCM	240
12	4	600MCM	300
10	6	750MCM	400
8	10	1000MCM	500
***Note: Table shows commercially used equivalent values.**			

Appendix B

Datasheets for Various System Components

Table of Contents:

BCM® Bus Converter
BCM384x480y325A00

Fixed Ratio DC-DC Converter

FEATURES

- 384 Vdc – 48 Vdc 325 W Bus Converter
- High efficiency (>95%) reduces system power consumption
- High power density (>1000 W/in³)
  reduces power system footprint by >40%
- "Full Chip" VI Chip® package enables surface mount, low impedance interconnect to system board
- Contains built-in protection features: undervoltage, overvoltage lockout, overcurrent protection, short circuit protection, overtemperature protection.
- Provides enable/disable control, internal temperature monitoring
- ZVS/ZCS Resonant Sine Amplitude Converter topology
- Can be paralleled to create multi-kW arrays

TYPICAL APPLICATIONS

- High End Computing Systems
- Automated Test Equipment
- Telecom Base Stations

DESCRIPTION

The VI Chip® bus converter is a high efficiency (>95%) Sine Amplitude Converter™ (SAC™) operating from a 360 to 400 Vdc primary bus to deliver an isolated, ratiometric output from 45 to 50 V. The SAC offers a low AC impedance beyond the bandwidth of most downstream regulators, meaning that input capacitance normally located at the input of a regulator can be located at the input to the SAC. Since the K factor of the BCM384F480T325A00 is 1/8, that capacitance value can be reduced by a factor of 64x, resulting in savings of board area, materials and total system cost.

The BCM384F480T325A00 is provided in a VI Chip package compatible with standard pick-and-place and surface mount assembly processes. The VI Chip package provides flexible thermal management through its low junction-to-case and junction-to-board thermal resistance. With high conversion efficiency the BCM384F480T325A00 increases overall system efficiency and lowers operating costs compared to conventional approaches.

V_{IN} = 360 – 400 V	P_{OUT} = 325 W(NOM)
V_{OUT} = 45 – 50 V (NO LOAD)	K = 1/8

PART NUMBERING

PART NUMBER			PACKAGE STYLE	PRODUCT GRADE
BCM384	**x**	480T325A00	**F** = J-Lead **T** = Through hole	**T** = -40° to 125 °C

For Storage and Operating Temperatures see Section 6.0 General Characteristics

TYPICAL APPLICATION

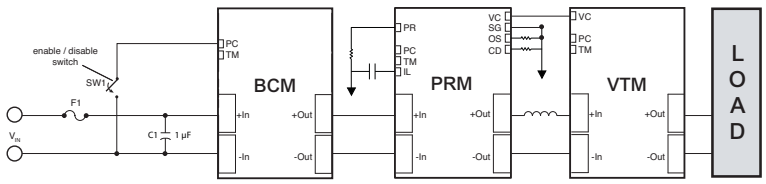

VI Chip® BCM® Customer Evaluation Board User Guide

Contents

Introduction

- Oscilloscope probe jack for output voltage and ripple measurements
- Simple to use
- Ring lug or solder connections
- Parallelable

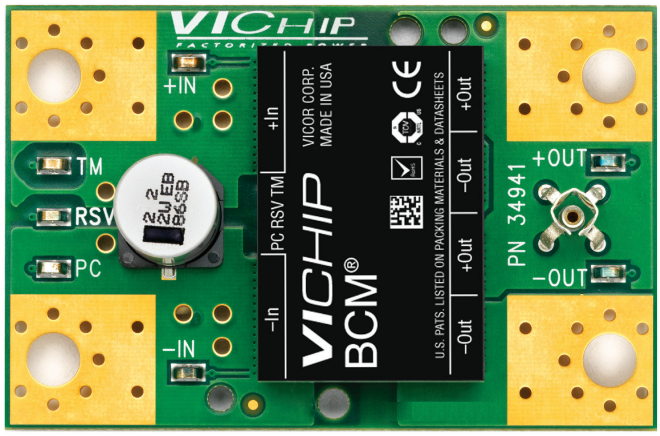

Introduction

The Customer Evaluation Board offers a convenient means to evaluate the performance of Vicor's BCM bus converter and has been optimized for user convenience. Refer to the appropriate BCM data sheet for performance and operating limits. The data sheets are available for downloading at vicorpower.com.

It is important to remember the fast response of most BCMs can readily show the limitations of the source, load, and associated wiring connected to the evaluation board. Care should be exercised to minimize stray source and load impedances in order to fully exercise the BCM.

Please refer to Figure 1 for locations of the input and output connections as viewed from the component side. Wires may be soldered directly to the pads instead of ring lugs if desired to minimize circuit impedances.

Wide Input Range Synchronous Buck Controller with Analog Current Monitor

Check for Samples: LM5117, LM5117-Q1

FEATURES

- **LM5117-Q1 is an Automotive Grade product that is AEC-Q100 grade 1 qualified (-40°C to +125°C operating junction temperature)**
- **Emulated Peak Current Mode Control**
- **Wide Operating Range from 5.5V to 65V**
- **Robust 3.3A Peak Gate Drives**
- **Adaptive Dead-Time Output Driver uontrol**
- **Free-Run or Synchronizable Clock up to 750kHz**
- **Optional Diode Emulation Mode**
- **Programmable Output from 0.8V**
- **Precision 1.5% Voltage Reference**
- **Analog Current Monitor**
- **Programmable Current Limit**
- **Hiccup Mode Over Current Protection**
- **Programmable Soft-Start and Tracking**
- **Programmable Line Under-voltage Lockout**
- **Programmable Switch-Over to External Bias Supply**
- **Thermal Shutdown**

PACKAGES

- **HTSSOP-20 (Thermally enhanced)**
- **WQFN-24 (4mm x 4mm)**

DESCRIPTION

The LM5117 is a synchronous buck controller intended for step-down regulator applications from a high voltage or widely varying input supply. The control method is based upon current mode control utilizing an emulated current ramp. Current mode control provides inherent line feed-forward, cycle-by-cycle current limiting and ease of loop compensation. The use of an emulated control ramp reduces noise sensitivity of the pulse-width modulation circuit, allowing reliable control of very small duty cycles necessary in high input voltage applications.

The operating frequency is programmable from 50 kHz to 750 kHz. The LM5117 drives external high-side and low-side NMOS power switches with adaptive dead-time control. A user-selectable diode emulation mode enables discontinuous mode operation for improved efficiency at light load conditions. A high voltage bias regulator that allows external bias supply further improves efficiency. The LM5117's unique analog telemetry feature provides average output current information. Additional features include thermal shutdown, frequency synchronization, hiccup mode current limit and adjustable line under-voltage lockout.

User's Guide
SNVA466B–May 2011–Revised April 2013

AN-2103 LM25117 Evaluation Board

1 Introduction

The LM5117 evaluation board provides the design engineer with a fully functional synchronous buck converter based on Emulated Current Mode Control to evaluate the LM5117 controller IC. The evaluation board provides 12V output with a 9A current capability in addition with average output current information. The input voltage ranges from 15V to 55V.

2 Performance of the Evaluation Board

- Input Voltage Range: 15V to 55V
- Output Voltage: 12V
- Output Current: 9A
- Nominal Switching Frequency: 230 kHz
- Synchronous Buck Operation: Yes
- Diode Emulation Mode: Yes
- Hiccup Mode Overload Protection: Yes
- External VCC Sourcing: Yes
- Current Monitor Output: Yes

3 Powering and Loading Consideration

3.1 Proper Board Connection

When applying power to the LM5117 evaluation board certain precautions need to be followed. A misconnection can damage the assembly.

The input connection is made to the J1 (VIN+) and J2 (VIN-) connectors. The load is connected to the J3 (VOUT+) and J4 (VOUT-). Be sure to choose the correct connector and wire size when attaching the source power supply and the load. The average output current can be monitored at J5. Use RCA jack to remotely sense the current monitor output. TP5 is directly connected to UVLO and can be used as an input of the remote shutdown signal.

3.2 Source Power

The power supply and cabling must present low impedance to the evaluation board. Insufficient cabling or a high impedance power supply will droop during power supply application with the evaluation board inrush current. If large enough, this droop will cause a chattering condition upon power up. During power down, this insufficient cabling or a high impedance power supply will overshoot, results in a non-monotonic decay on the output.

An additional external bulk input capacitor may be required unless the output voltage droop/overshoot of the source power supply is less than 1V.

3.8 Evaluation Board Schematic